



Ph.D. Dissertation

UWB Antenna Design for Communication System Performance Optimization

Author: Pavel Miškovský
Advisors: José María González-Arbesú
Jordi Romeu i Robert

December 2009

ABSTRACT

UWB technology originally developed during the 80's for strictly military applications, gained more interest in the research community since 1998, following the release of FCC regulatory report on UWB communications systems. The development of UWB technology without restrictions, including antennas as an essential part of wireless communication systems was greatly accelerated. This thesis deals with the design and performance assessment of UWB antennas for optimum communication system performance.

Traditional antenna performance descriptors such as input port impedance, radiation pattern or effective antenna length generally face strong frequency dependence. In this context the traditional narrowband approach to antenna design is no more appropriate for UWB antennas. Such antennas behave as spatial and temporal filters, distorting the radiated waveforms. Indeed, the radiated signal distortion is an inherent UWB antenna issue, usually assessed qualitatively. Consequently the need for a compact frequency and direction-independent antenna distortion descriptor was identified. For this purpose the first objective of the thesis is to define and analyze new direction-independent UWB antenna descriptors that should assess the antenna performance in terms of transmitted UWB pulse fidelity. Such a compact descriptors will summarize the antenna performance in a single number and therefore will be very convenient for antenna optimization using CAD.

As a second objective of the thesis, a critical analysis of the proposed UWB descriptors measurement methods is developed. Namely, spatially averaged fidelity (SAF) descriptors and radiation efficiency measurement methods in ultra wideband frequency range are shown. Particular attention was paid to the enhancement of the Wheeler cap based radiation efficiency measurement method to wide frequency ranges.

A demonstration of the practical use of the newly defined UWB direction-independent antenna descriptors is shown through the design and optimization of impedance loaded linear monopoles. For this purpose an evolutionary optimization technique,

Particle Swarm Optimization (PSO) was used. Resistively and capacitively loaded monopoles were optimized in terms of SAF, mean radiation efficiency and reflected energy at input port. Pareto fronts were determined, showing what performance can be expected from such impedance loading profiles along linear wire monopoles. The optimum impedance loaded monopole was selected based on a compromise between different parameters (SAF, mean radiation efficiency, reflected energy).

Finally, the optimized monopole performances were verified experimentally. Firstly, due to the parasitic effects of discrete resistors and capacitors packages, the monopoles scaled to a frequency range 5-times lower than the range used in simulations were fabricated. Operating at lower frequencies, the frequency dependent parasitic effects are lower. The measured performances prove the concept of UWB antenna design in terms of the new proposed descriptors.

Secondly, a resistively loaded monopole was fabricated using resistors without package, made of very thin metallic layers. Due to the high fabrication accuracy requirements the monopole didn't reach the expected performance.

The relevance of the new UWB antenna performance descriptors was proved through the design and experimental verification of UWB loaded linear monopoles.

RESUM

La tecnologia UWB es va desenvolupar inicialment als anys 80 per aplicacions estrictament militars, i no va ser fins al 1998 amb la regulacions per part de la FCC dels sistemes de comunicacions UWB quan la recerca en aquesta àrea va començar a despertar de nou. Des d'aquest moment l'avanç en el desenvolupament dels sistemes UWB i els components que el formen, incloent les antenes com a part essencial de tot sistema de comunicacions sense fils, ha estat significatiu. Aquesta tesi es centra en el disseny i avaluació de les prestacions de les antenes UWB per tal d'aconseguir un sistema de comunicacions amb prestacions òptimes.

Els paràmetres tradicionalment utilitzats per la descripció de les prestacions d'una antena, com la impedància d'entrada, el diagrama de radiació o la longitud efectiva de l'antena, són generalment paràmetres amb una forta dependència freqüencial. De manera que les aproximacions de banda estreta utilitzades pel disseny d'antenes no seran vàlids per al disseny d'antenes UWB. Aquestes antenes es comporten essencialment com a filtres espacials i temporals que distorsionen les formes d'ona radiades. Realment, la radiació de senyal distorsionada és un dels problemes inherents en una antena UWB, el qual típicament s'avalua de forma qualitativa. Com a conseqüència s'identifica la necessitat de trobar un descriptor capaç de avaluar la distorsió radiada per l'antena UWB, que sigui independent de la freqüència i de la direcció de radiació. Amb aquest propòsit el primer objectiu d'aquesta tesi és la definició i anàlisi de nous descriptors, independents de la direcció, capaços d'avaluar les prestacions de l'antena UWB en funció de la fidelitat del pols transmès. Aquests descriptors determinaran les prestacions de l'antena mitjançant un únic valor, la qual cosa permetrà l'ús de eines CAD per la optimització de l'antena.

Com a segon objectiu de la tesi, s'ha desenvolupat un mètode de mesura per poder quantificar de forma acurada els descriptors proposats per la descripció de les prestacions de les antenes UWB. Amb aquest objectiu s'han avaluat descriptors basat en *spatially average fidelity* (SAF) i mètodes de mesura de la eficiència de radiació. En concret s'ha concentrat els esforços en la millora dels mètodes de mesura basat en el concepte Wheeler cap per grans amplituds de banda.

Com a demostració pràctica de la utilitat dels nous descriptors, independents de la direcció, desenvolupats durant la tesi, s'ha realitzat el disseny i optimització de una

antena monopòl carregada amb impedàncies linealment distribuïts. Per aquest disseny s'ha utilitzat addicionalment un mètode d'optimització basat en objectiu Particle Swarm Optimization (PSO). La carrega dels monopòls mitjançant elements resistius i capacitius s'ha realitzat per unes òptimes prestacions del SAF, es a dir per una òptima eficiència de radiació i energia reflectida la port d'entrada. Per aquesta configuració s'han trobat el fronts de Pareto, determinant així quines prestacions cal esperar d'aquest monopòls carregats amb impedàncies de forma distribuïda. La distribució òptima de carrega d'aquest monopòl ha estat seleccionada basant-nos en un compromís entre els diferents paràmetres que caracteritzen l'antena UWB (SAF, eficiència de radiació, energia reflectida).

Finalment, la optimització de les prestacions del monopòl s'ha verificat experimentalment. Primerament, en aquest disseny experimental i degut als efectes paràsits dels elements resistius concentrats i l'encapsulat dels elements capacitius, el monopòl s'ha escalat a una freqüència 5 cops inferior a la inicialment esperada. Fixem-nos que a freqüències inferiors les prestacions dels efectes paràsits son menors. Les mesures demostren la utilitat del descriptors proposats per al disseny i avaluació d'antenes UWB. En segon lloc, s'ha dissenyat i fabricat un monopòl carregat resistivament mitjançant la realització de resistències implementades amb capes fines de material metàl·lic dissipatiu. Degut a toleràncies en la fabricació els resultants en aquest cas no han sigut els esperats.

La rellevància dels nous descriptors proposats per descriure les prestacions de les antenes UWB s'ha demostrar mitjançant el disseny i la obtenció de resultats experimentals de monopòls carregats seguint una distribució de carrega lineal.

To my family and Eugenia,

ACKNOWLEDGEMENTS

I would like to thank my advisors José María González-Arbesú and Jordi Romeu for their guidance, support and patience, through these years. I greatly appreciate your infinite availability, great intuition and objectiveness and I hope I learned from such great qualities.

I also would like to thank Miguel Ángel Lagunas and Simó Aliana, Director and General Administrator of CTTC, respectively, for giving me the opportunity to undertake my thesis in the frame of CTTC Pre-Doctoral program. CTTC was always a place where I found not only an unconditional support for my thesis but also an excellent working environment and big amount of friends that helped to make this work a pleasant journey. I prefer to thank them all together, I am sure that you know who I mean. It was exhausting sometimes but I am convinced that without your sense of humor, all these running kilometers together and football leagues it would have been much harder.

I cannot forget my former advisor at CTTC and friend Jordi Mateu, who always encouraged me and helped me with my first publications and who is still enough strong to beat me in a marathon. I'll get you next year!

I also would like to thank Josep Parrón from UAB and Jaume Anguera from FRACTUS, for having reviewed this work in a very short time and for helping me to improve its final form.

Finally, a big hug to my family and Eugenia, for your love and support during all these years. To you I dedicate this work.

If you cannot measure it, you cannot improve it.
(Lord Kelvin 1824-1907)

CONTENTS

INTRODUCTION.....	
1. BACKGROUND OF THE THESIS	1
1.1. History of UWB Antennas	1
1.2. State of the Art of UWB Antennas	7
1.2.1. Frequency Independent Antennas	8
1.2.2. Impedance Loaded Antennas	10
2. AIMS OF THE THESIS	11
2.1. Identification of Scientific Problems	11
2.1.1. Definition of UWB Antenna Descriptors	12
2.1.2. UWB Antenna Radiation Efficiency	15
2.2. Objectives of the thesis	20
RESULTS.....	
3. DESCRIPTORS FOR UWB ANTENNA PERFORMANCE ASSESSMENT	23
3.1. Formulation for a Single Antenna	23
3.1.1. Spatially Averaged Fidelity – SAF_1	23
3.1.2. Application of SAF_1	24
3.2. Formulation for a Transmit-Receive System	37
3.2.1. Spatially Averaged Fidelity – SAF_2	38
3.2.2. Averaged Energy Efficiency – AE	39
3.2.3. Application of SAF_2 and AE	39
3.3. Conclusions	46
4. MEASUREMENT METHODS OF UWB DESCRIPTORS	47
4.1. Measurement of SAF_1	47
4.1.1. Wide Frequency Range Anechoic Chamber Calibration	48
4.1.2. Template Positioning and Sampling	52
4.2. Measurement of Radiation Efficiency in UWB	59
4.2.1. Application of Johnston-Geissler method to UWB	59
4.2.2. J-G method Assessment on a Lossy Monopole	61
4.2.3. Application of J-G method to UWB Antennas	63

4.3.	Conclusions	67
5.	DESIGN AND OPTIMIZATION OF AN UWB MONOPOLE	71
5.1.	Impedance Loading Profile Definition	72
5.1.1.	Geometry Definition	72
5.1.2.	Loading Profile	73
5.2.	Particle Swarm Optimization – PSO	75
5.2.1.	Basic Overview of PSO	75
5.2.2.	PSO Implementation in Matlab	80
5.3.	Resistively Loaded Monopole	82
5.3.1.	Specific PSO Settings	82
5.3.2.	Resistive Profile Optimization	83
5.3.3.	Monopole Length	88
5.3.4.	Discrete Resistor Tolerances	91
5.3.5.	Discrete Resistors Parasitics	93
5.3.6.	PSO Solution Analysis	96
5.4.	Capacitively Loaded Monopole	98
5.4.1.	Specific PSO Settings	98
5.4.2.	Capacitive Profile Optimization	99
5.5.	Conclusions	103
6.	LOADED MONOPOLE FABRICATION AND MEASUREMENT	105
6.1.	Scaled Resistively Loaded Monopole	105
6.1.1.	Fabrication Process	106
6.1.2.	Characterization of the Resistively Loaded Monopole	108
6.2.	Scaled Capacitively Loaded Monopole	114
6.2.1.	Fabrication Process	114
6.2.2.	Measurement of the Capacitively Loaded Monopole	116
6.3.	Thin Metal Layer Monopole	120
6.3.1.	Fabrication Process	120
6.3.2.	Measurement of the Thin Layer Resistive Monopole	124
6.4.	Conclusions	129

CONCLUSIONS.....

7.	CONCLUSIONS AND RESEARCH PERSPECTIVE	131
	ANNEX.....	135
	REFERENCES.....	141

INTRODUCTION

1. BACKGROUND OF THE THESIS

1.1. History of UWB antennas

Ultrawideband (UWB) antennas should share the same history with UWB radio communications, since antenna is an indispensable component of wireless radio systems. However, it is not exactly the case, because UWB antennas were discovered much earlier than the first UWB radio system.

The origins of UWB antennas are assigned at the very beginning of the radicomunications history, back to 19th century, to a “spark gap” era. Spark gap transmitters were used by radio pioneers such as Hertz, Tesla or Marconi in their experiments. Actually a spark gap was “UWB” by accident not by design, nevertheless many early antenna design were ultra-wideband [Schantz04a]. In 1898 Oliver Lodge proposed a concept of narrowband frequency domain radio and invented the first practical radio tuning system. Lodge preferred antennas shown on Figure 1.1 consisting of triangular metallic pieces [Lodge98], being a clear precursor of today’s well known UWB bow-tie antennas. For this reason Schantz attributes the disclosure of the field of UWB antennas to the year 1898, initialized by Oliver Lodge.

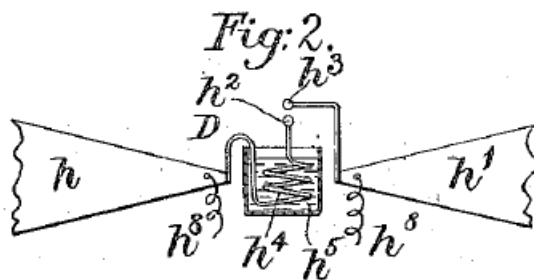


Figure 1.1: Triangular antenna used by O. Lodge in 1898, precursor of bow-tie antenna, [Lodge98].

Lodge also used antennas known today as biconical antenna (Figure 1.2.a). Spark gap era inventors such as Hertz, Marconi or Bose (inventor of pyramidal and conical horn) developed and used first UWB antennas. The fact that the history of UWB antennas was not subject to same scrutiny, as the history of spark-gap transmitters, is the reason that some of antenna designs have been forgotten to be rediscovered later.

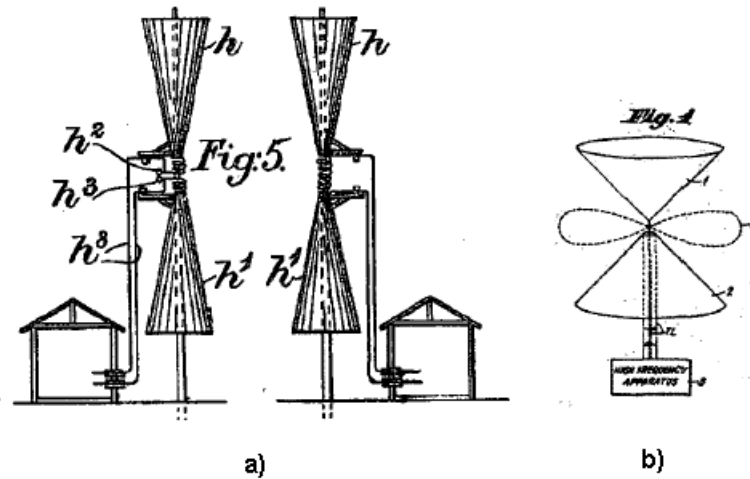


Figure 1.2: Biconical antenna: **a)** Lodge's design from 1898, [Lodge98] and **b)** Carter's design from 1939, [Carter39]

Several decades later UWB reappeared, because of the increased bandwidth needs in television (6 MHz) compared to AM or FM radio (10 kHz – 75 kHz). To this period are dated the first attempts to design UWB antennas. Many designs like biconicals, bow-ties or horns were rediscovered but also improved. First basic UWB antenna principles, such as achievement of broader bandwidths using tapered feed or fat radiating elements, were discovered.

In order to summarize some of these antenna rediscoveries which gave the bases of several today's UWB antennas, we can cite few of the most important designs:

- Lodge's biconical antenna rediscovered and improved by Carter [Carter39]
- Schelkunoff's coaxial horn antenna (Figure 1.3) [Schelkunoff41] whose concept was improved by Lindenblad [Lindeblad41] and finally rediscovered by Kraus as "volcano smoke" antenna [Paulsen03].
- Kandoian's discone antenna [Kandoian46] with a similar principle as Carter's conical monopole
- Friis and Schelkunoff's [Schelkunoff66] slot antennas improved by Marié [Marie62] and Barnes [Barnes00] varying the width of the slot.

All the above-mentioned antennas are shown on figures 1.2, 1.3, 1.4, 1.5 and 1.6.

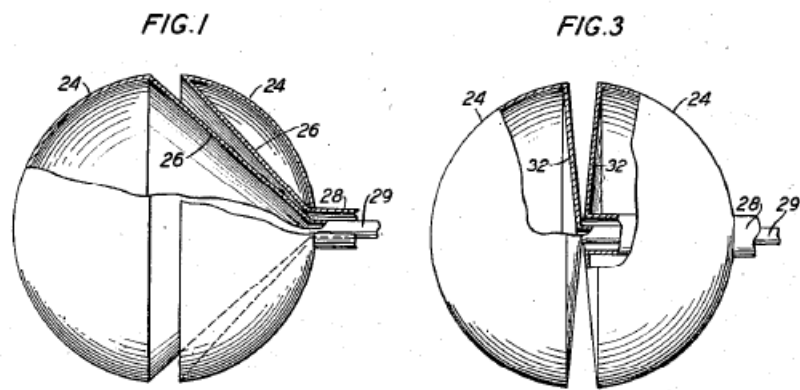


Figure 1.3: Schelkunoff's coaxial horn antenna patented in 1941, [Schelkunoff41]

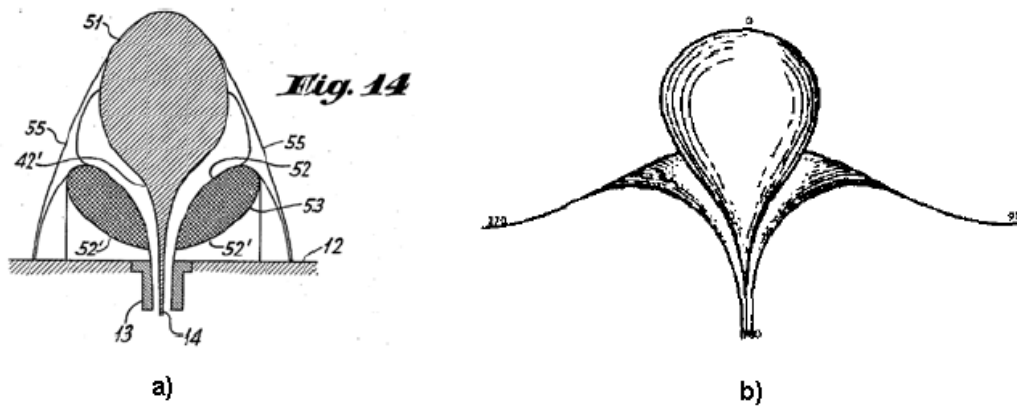


Figure 1.4: a) Lindenblad's coaxial horn antenna patented in 1941, [Lindeblad41] and b) Kraus volcano smoke antenna from 1945, [Paulsen03].

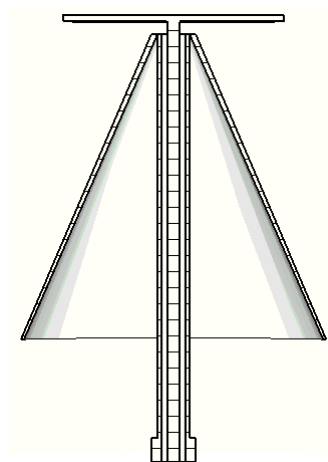


Figure 1.5: An example of discone antenna cross section, introduced by Kandoian in 1946.

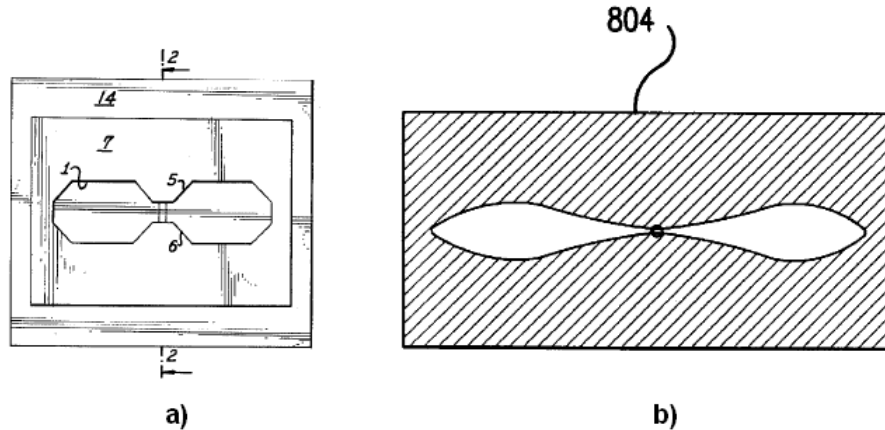


Figure 1.6: a) Slot antenna patented by Marié in 1962, [Marie62], b) Same principle patented by Barnes in 2000, [Barnes00]

First spark gap radios used by Marconi were actually pulse based UWB radios. Spark gaps were used until the beginning of 20th century when the narrowband radios were shown to be better for voice transmission. Finally they were forbidden due to radiofrequency (RF) interferences to carrier based narrowband radios. The origin of UWB technology similar to what is known today as UWB dates back to 1960's, when a feasibility of a communication system using very short pulses was studied by Ross [Fontana00]. The invention of the sampling oscilloscope by Hewlett-Packard in 1962, opened the path to a direct measurement of impulse responses of microwave circuits. This motivated the research in time-domain electromagnetics, and revealed the potential of pulse based transmission for radar and communications.

While working at Sperry Research Center, Ross applied impulse measurement techniques to the design of wideband, radiating antennas and consequently, using the same tools, to the design of short pulse radar. The first UWB communications patent was awarded in 1976 to Sperry Research Center, for a transmitter-receiver system using short base-band pulses, developed by Ross [Ross73].

Due to the inherent properties of UWB technology, it was developed during the 80's for strictly military applications. This technology was referred to as "base-band", "carrier-free" or "impulse" communications. In 1989, the term UWB was introduced by the US Department of Defense (DoD), for signals having at least 1.5GHz bandwidth or a 20dB fractional impedance bandwidth exceeding 25%. Since 1994, much of the work in UWB field, previously performed under classified U.S.

government programs, has been carried out without any restrictions and the development of UWB technology was greatly accelerated.

In 1998, the Federal Communications Commission (FCC) proposed a rule making group to regulate UWB communication systems and the first regulatory report was released on April 22, 2002. In this report FCC defines a term *Ultra-Wideband system* as a *communication system having a fractional bandwidth larger than 20% or a bandwidth of more than 500 MHz* [FCC02]. Fractional bandwidth is defined as a difference between upper and lower frequencies (f_H ; f_L) of the operational frequency band divided by its center frequency f_C . The center frequency can be defined as arithmetic or geometric average of f_H and f_L frequencies. The difference from narrowband systems is that in narrowband the bandwidth is typically 10% or less of the center frequency. Figure 1.7 shows an example of usable spectrum defined by Part 15 of the FCC rules for U.S. standard.

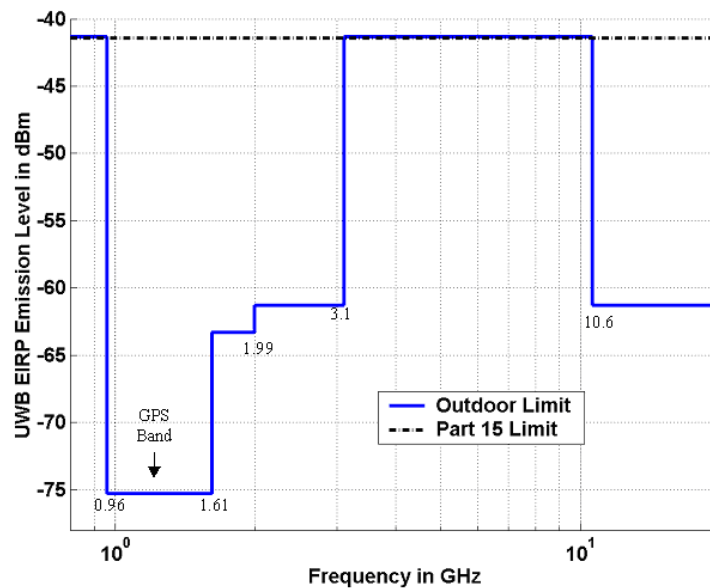


Figure 1.7: Spectral mask defined by FCC for outdoor UWB systems US standard, from [FCC02].

UWB signals as defined by FCC can be transmitted within the frequency band from 3.1 GHz to 10.6 GHz at power levels that do not overpass -41 dBm/MHz. An FCC regulation induced a strong interest in UWB regulation activities in Europe and Asia. All regulatory efforts in Europe resulted in a document published on 21st of February 2007, allowing the use of the radio spectrum for equipment using UWB technology within the European Community [Com07]. The power limits and usage constraints in

Europe differ significantly from those defined by the FCC in US. The main difference between the European and US UWB regulation concerns the frequency range. The European band is from 6.0 GHz to 8.5 GHz and the U.S band from 3.1 GHz to 10.6 GHz.

UWB signals are generally short duration impulses or non-sinusoidal waveforms (e.g. triangular, chirped etc.). Typical pulse waveforms used in UWB systems include rectangular pulse, Gaussian pulse, Gaussian doublet and Rayleigh monocycles etc, having a very wideband spectrum [Chen02], [Conroy99]. Monocycles have a spectrum that does not contain a DC component, the fact which is useful for some applications and facilitates the design of antennas amplifiers, downconverters etc. [Han02]. Moreover, the DC components can not be transmitted by antennas, so using pulses with DC component is not very energy efficient.

One of the most important advantages of the UWB technology is the improved transmission channel capacity. From Shannon's capacity equation [Shannon49], the channel capacity is proportional to the bandwidth of the channel and to the logarithm of the SNR (Signal to Noise Ratio). The channel capacity can increase by linearly increasing the channel bandwidth or exponentially increasing the signal power. Due to the low power levels and ultra wide bandwidth, defined by FCC regulation, UWB systems can offer very high data rates at very low power. UWB technology performs better (regarding high speed data transmissions) in short-range applications (shorter than 10 m).

The transceiver structure should be very simple due to the absence of carrier. Recent advances in the field of silicon design makes low cost UWB systems possible [Fontana02], [Lee01], [Miao06].

Another advantage of UWB from the point of view of the transmission-reception system is the robustness to fading and interference. The wideband nature of UWB signals reduces the effect of random amplitude fluctuations. Multipath components are easier to resolve and can be used to improve signal detection.

Thanks to inherent properties of UWB signals, the UWB systems are suitable for two types of applications: short range-high data rate applications or high range low data rate applications.

The first category enables high speed data transfer useful for computers or consumer electronics. The second category is suitable for ranging and imaging applications based on RADAR principles, such as UWB testbed developed at CTTC [Mollfulleda05],[Mollfulleda06].

1.2. State of the Art of UWB Antennas

Prior to the state of the art analysis it is convenient to understand what an UWB antenna is.

We understand by the term “UWB antenna”, an antenna that potentially uses all its bandwidth (as defined by FCC) all the time and its properties are consistent and stable across the operational band: impedance match, pattern, gain, polarization. In order to avoid confusion it should be underlined that an UWB antenna is not a multi-narrowband antenna. Some differences between conventional narrowband antennas and UWB antennas design can be pointed out:

Narrowband antennas: Narrowband antenna properties such as gain or directivity patterns are essentially constant through the whole bandwidth, which is easily accomplished since it is 10% or less of center frequency. Impedance matching can be relatively easily realized using a matching network, because in general the impedance is an intrinsic property of the antenna (quarter wavelength resonant monopole 36Ω , half wavelength resonant dipole 73Ω) [Balanis97].

UWB antennas: Antenna parameters such as gain or directivity tend to vary significantly across the operational bandwidth. Because UWB antenna impedance is a design choice, a significant control on impedance matching is possible. There are two principal techniques of achieving a desired impedance: i) control of geometry (preferred), ii) impedance loading (arbitrary good impedance match can be obtained). In general any antenna can be considered as an impedance transformer from the antenna feeding line impedance to the impedance of free-space. A good matching of UWB antenna needs a smooth impedance transition [Schantz04]. Due to the wideband nature of UWB signals, UWB antennas contrary to narrowband antennas, face a problem of dispersion. Dispersion is a particular kind of signal distortion in which the phase velocity of the wave depends on frequency. In other words it is a phenomenon

by which different frequency components propagate at different phase velocities yielding distorted and inconsistent time domain waveforms which can significantly increase the complexity of the detection mechanism at the receiver.

Several types of UWB antennas have thoroughly been described in literature. Regarding the above-mentioned consistency of UWB antenna parameters over the operational bandwidth, two antenna classes deserve special attention in this section: frequency independent antennas and impedance loaded antennas.

1.2.1. Frequency independent antennas

Around year 1948, Mushiake, remarked that self-complementary antennas have (at least theoretically) a constant input impedance of 188Ω , independent of the structure shape and source frequency. As stated by Mushiake [Mushiake92], the term self-complementary planar structure means a structure of the shape which is identical to a complementary one, as shown on Figure 1.8. Two complementary structures are exactly identical in shape but their electric and magnetic properties are interchanged.

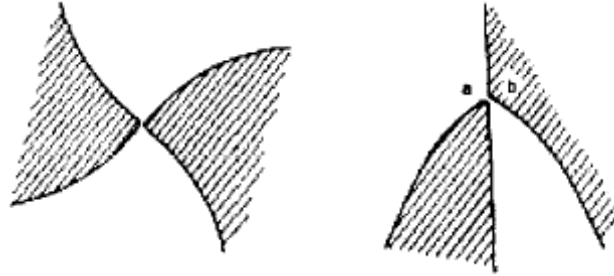


Figure 1.8: Examples of self complementary planar structures. On the right picture, surface (a) is complementary to dashed surface (b).

Mushiake states that for the complementary structure, the input impedance must be equal to the original input impedance and its value is given by expression (1.1)

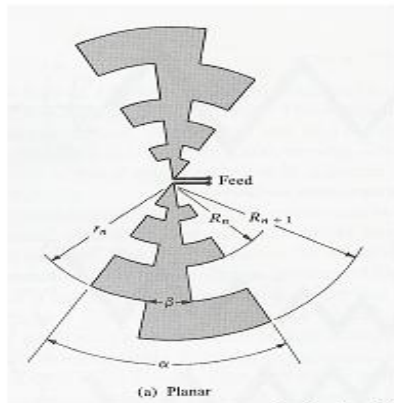
$$Z = \frac{Z_0}{2} = \frac{1}{2} \sqrt{\frac{j\omega\mu}{j\omega\varepsilon + \sigma}} \quad (1.1)$$

where Z_0 is the electromagnetic impedance also known as the intrinsic impedance of the medium, defined as the ratio between the magnitudes of electric and magnetic fields. In free space Z_0 is equal to 120π and consequently the expression 1.1 reduces to

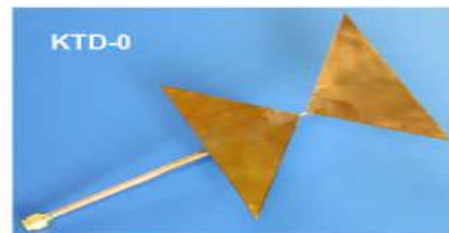
$$Z = 60\pi = 188\Omega \quad (1.2)$$

This value of constant input impedance at all frequencies is verified when the antenna shape extends to infinity. In practice the shape of the antenna is cutted-off to reasonable dimensions, at distance from the feeding point where the current becomes significantly low. The higher frequency of the antenna bandwidth is limited by the size of the feeding point and the lower frequency is limited by the overall size of the antenna.

Based on the principle of self-complementary antennas Rumsey [Rumsey57] proposed new class of frequency independent antennas which shape is only specified in terms of angles. Mushiake's and Rumsey's work, lead to development of log-periodic antenna (Figure 1.9 a) and helped to explain the performance of 90° bow-tie antenna (Figure 1.9 b) by DuHamel in [DuHamel57].



a)



b)

Figure 1.9: a) Example of log-periodic antenna [Balanis97], b) 90° bow-tie antenna [Gonzalez04]

Frequency independent antennas have a good performance in terms of input impedance match and are considered very appropriate for UWB applications nevertheless they are very prone to signal dispersion. Their physical shape (spirals,

log periodic antennas etc.) relies on the repetition of the geometry and so their phase center (the point from where the signal is radiated) moves with frequency (small antenna portion radiates high frequencies and large antenna portion radiates low frequencies) which is the cause of signal dispersion.

1.2.2. Impedance loaded antennas

Altshuler [Altshuler61] was the first who realized an experiment with resistive loading to reduce reflections on the antenna input, placing a resistance at quarter wavelength from the open ends of the dipole. This approach leads to outward travelling wave on the remainder of the antenna, but works well only over narrow frequency ranges.

A new possible antenna design for pulse transmission was proposed by Wu and King in 1965. The objective was to determine the distribution of the internal impedance along a cylindrical dipole, for which a pure traveling wave would exist [Wu65]. Wu and King considered a dipole antenna with continuous resistive loading. A practical application of the Wu-King's current distribution was realized by Kanda for the purpose of picosecond pulse measurements [Kanda78]. Kanda made the resistive elements by depositing a linearly tapered thin film of alloy having a relatively high resistivity, on a glass rod. This way the losses were increased along the radiating element, from the feeding point towards extremity, the same way as resistivity. The progressive as well as the reflected waves were attenuated and the resulting travelling wave should procure almost constant input impedance in a wide range of frequencies. Kanda demonstrated that the resistively loaded antenna can preserve the waveform of the radiated impulse at cost of the energy efficiency, and so could be considered suitable for UWB systems in terms of low pulse distortion [Kanda78].

2. AIMS OF THE THESIS

In this chapter the objectives of the thesis are outlined through the previous identification of scientific problems.

2.1. Identification of Scientific Problems

In a transmitter-receiver (tx-rx) system such as the one depicted on Figure 1.10, several distorting and attenuating factors are involved along the path followed by the generated signal. These factors become more complex when the same system is considered in a UWB frequency range, because the bandwidth extends over several decades.

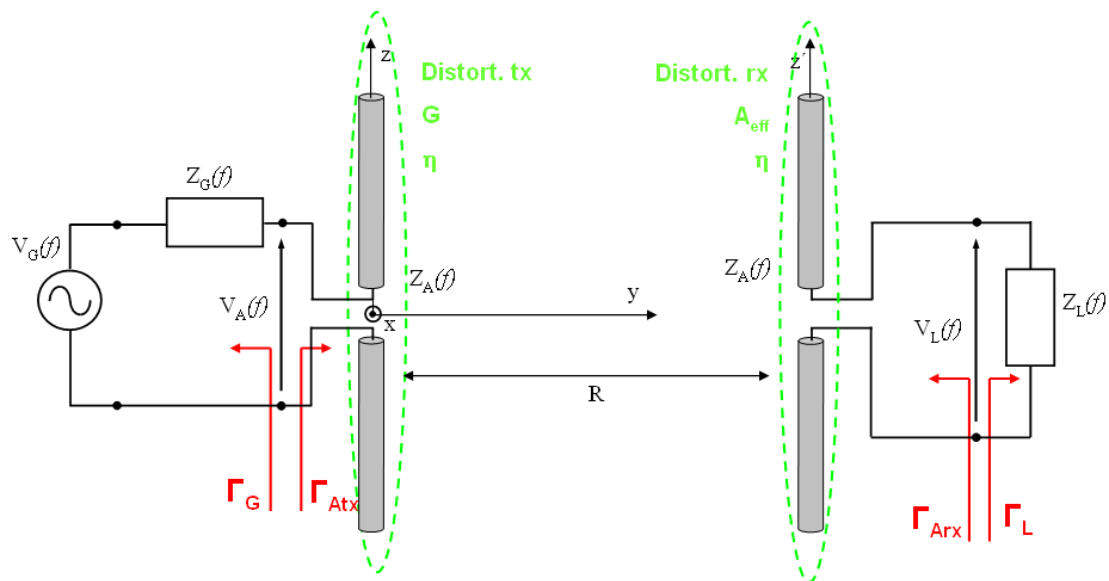


Figure 2.1: UWB tx-rx system

Firstly, a good UWB link tends to maximize the amount of power delivered from the generator to the load Z_L within the operational frequency band. The delivered power loss occurs at transitions between the antenna and the feeding line due to impedance mismatch, also at the transition between the antenna and the free space due to radiation efficiency η , but it is also dependent on the propagation distance R , on the antenna gain $G(f, \theta, \phi)$ and the receptor antenna effective area $A_{eff}(f, \theta, \phi)$.

Secondly, the generated pulse suffers from distortion along the tx-rx path. Distortion is often related to the same mechanism that produces the delivered power loss, such as impedance mismatch. In certain antenna structures such as frequency independent antennas, the phase center varies with frequency what originates that not all the signal frequency components arrive at the same time, distortion phenomenon known as dispersion.

As mentioned in section 1.2, a significant control of UWB antenna impedance match over its operational bandwidth is possible through the control of antenna geometry and/or impedance loading. The power loss and distortion due to antenna input impedance frequency variation and so due to impedance mismatch can be quantified and measured through the use of reflection coefficients Γ_G or Γ_{Atx} .

Due to the dispersion properties of UWB antennas, the relation between the current distribution and the radiated electromagnetic signal is not always as straightforward as in the case of narrowband antennas.

In order to characterize an UWB antenna performance alone or within a tx-rx system, a characterization of transmitted and received pulses distortion is necessary. Some descriptors already exist, some can be improved and some new descriptors could be proposed.

2.1.1. Definition of UWB antenna descriptors

Several antenna performance descriptors, such as input impedance bandwidth, gain, beamwidth or effective antenna length, can face strong frequency dependence. In this context, the traditional narrowband approach to antenna design is no more appropriate for UWB antennas. Moreover, the frequency dependence of the radiation pattern produces that antennas behave as temporal and spatial filters, radiating differently distorted time-domain waveforms in different directions. For the same excitation, the comparison of two antennas radiating two different waveforms is almost impossible. As illustrated on Figure 2.2, a wire monopole and triangular monopole fed by the same pulse (a pulse having a flat spectrum within the UWB FCC frequency range), radiate differently distorted pulses in different angular directions. From such a

comparison it is impossible to objectively determine which of the two antennas is better for a given application.

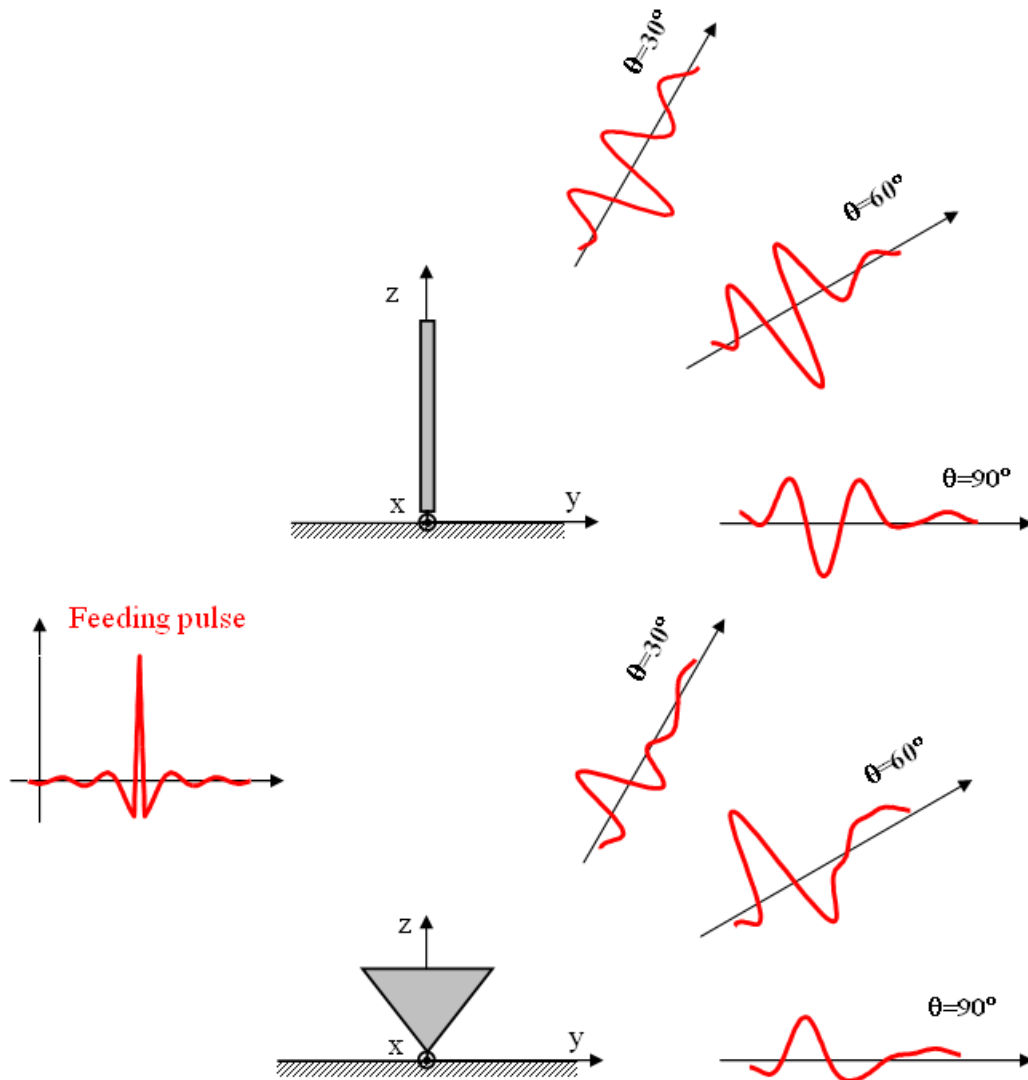


Figure 2.2: Two different antennas (wire monopole and triangular monopole) with identical feeding pulse radiate differently distorted time domain pulses

The radiated signal distortion is one of the inherent issues of UWB antennas, usually assessed qualitatively, that deserves a special attention. Lamensdorf and Susman [Lamensdorf94] proposed a qualitative pulse fidelity metric, measuring the amount of resemblance between two pulses. In the early 70's, they conducted a research on antennas for baseband short sub-nanosecond pulse transmission. They defined some of the bases for short-pulse antenna characterization, using a time-domain approach. Among different time-domain pulse antenna descriptors in [Lamensdorf94], a transmitted-energy pattern was defined as (2.1) in terms of energy per unit area.

$$U_T(\theta, \phi) = \frac{Z_0}{32\pi^2 R^2} \int_{-\infty}^{+\infty} \left| \frac{V_G(\omega)}{Z_G + Z_A(\omega)} \vec{F}_0(\theta, \phi, \omega) \right|^2 d\omega \quad (2.1)$$

where Z_0 is the free space impedance R is the distance between the two antennas, \vec{F}_0 is the field factor defined as a product of effective antenna height $h_e(\theta, \phi, \omega)$ and propagation constant $\beta = \omega/c_0$, Z_G and V_G are the generator impedance and voltage respectively, Z_A is the antenna input impedance.

As noted in [Lamensdorf94] the expression (2.1) is also dependent on the particular waveform $V_G(\omega)$ which excites the antenna and so the antenna impedance mismatch is included. In order to assess how an antenna distorts a transmitted or received waveform Lamensdorf and Susman also defined the signal fidelity F by the expression (2.2) being a measure of distortion, based on the cross-correlation of two signals $f(t)$ and $r(t)$.

$$F = \max_{\tau} \int_{-\infty}^{+\infty} f(t) r(t + \tau) dt \quad (2.2)$$

Combining the concepts of energy pattern and fidelity set by Lamensdorf and Susman, McLean [McLean05] defined two new pattern descriptors for UWB antennas: correlated energy pattern (2.3) and correlation coefficient pattern (2.4), both useful in systems where correlation detection is used.

$$U_C(\theta, \phi) = \frac{\left[\int_{-\infty}^{+\infty} \left(\vec{E}(t, R, \theta, \phi) \cdot \vec{a}(\theta, \phi) T(t) \right) R dt \right]^2}{Z_0 \int_{-\infty}^{+\infty} |\vec{T}(t)|^2 dt} \quad (2.3)$$

$$\rho(\theta, \phi) = \frac{\left[\int_{-\infty}^{+\infty} \left(\vec{E}(t, R, \theta, \phi) \cdot \vec{a}(\theta, \phi) T(t) \right) R dt \right]^2}{\sqrt{\int_{-\infty}^{+\infty} |\vec{T}(t)|^2 dt} \sqrt{\int_{-\infty}^{+\infty} |\vec{E}(t, R, \theta, \phi)|^2 R^2 dt}} \quad (2.4)$$

These descriptors consider a single antenna and indicate how the radiated UWB signals will change with time and as a function of direction. McLean *et al.* defines a template function $\vec{T}(t, \theta, \phi)$, which is an arbitrarily defined waveform involved in the

cross-correlation to assess the distortion of the radiated waveform \vec{E} . Vector \vec{a} denotes the polarization of the antenna. A variety of detection schemes that are not explicitly using a correlation can be effectively described in this way (peak detection is a correlation with delta function as a template) [McLean05].

The pattern descriptors defined by Lamensdorf and McLean, are direction dependent. For antenna performance optimization in terms of any of these descriptors, it would be much more convenient if they would be direction independent. In the actual state-of-the-art, antenna descriptors assessing the antenna performance in terms of transmitted pulse fidelity but being direction independent are an issue. A more *compact* time domain antenna descriptor without frequency and direction dependence is needed. In this sense, the compactness of the descriptor means that it should summarize the performance of the antenna (or antenna system) in a single parameter, in order to simplify its design using optimization techniques.

The above-mentioned analysis formed a base for the first objective of the thesis which is the definition and analysis of improved and new proposed direction independent UWB antenna descriptors.

2.1.2. UWB antenna radiation efficiency

An UWB antenna with a good match over its operational bandwidth is not necessarily a good antenna. The radiation efficiency is also an important issue. Antenna radiation efficiency following the IEEE standard is defined by the expression (2.5), as the ratio of the total power radiated by the antenna under test P_{rad} to the total power accepted by the antenna P_{acc} at its terminals [STD79]. As mentioned in [Schantz01], this definition of radiation efficiency assumes that the power applied on antenna terminals is either dissipated by antenna losses P_{LA} or radiated P_{rad} .

$$\eta_{rad} \equiv \frac{P_{rad}}{P_{acc}} = \frac{P_{rad}}{P_{rad} + P_{LA}} \quad (2.5)$$

This definition does not take into account the mismatch losses at the antenna input, regardless of narrowband or UWB approach. Narrowband antennas are usually perfectly matched to the source impedance at their operational resonant frequency. In

this situation a good power transfer from the source to the antenna is provided and the radiation efficiency is much more significant antenna parameter than mismatch losses. In wide bandwidths such as UWB, the frequency dependence of the antenna input impedance and consequently the possible impedance mismatch can be the most significant power loss factor. If an UWB antenna reflecting 99% of the input power and so accepting 1%, radiates half of the accepted power and dissipates the other half, following the definition (2.5), it has still the radiation efficiency of 50%. A solution to this arguable definition would be to use the total radiation efficiency, which takes into account net power applied at antenna input, instead of accepted power P_{acc} [Schantz02]. Another possibility would be to use the conventional efficiency definition and look for the best possible impedance match over the operation bandwidth.

Concerns about UWB radiation efficiency definition open a second important issue, which is the UWB radiation efficiency measurement method. Several radiation efficiency measurement methods have been thoroughly described in the literature. Many of them, such as directivity/gain [Pojar88] and radiometric methods [Ashkenazy85] are known for having reduced accuracy and significant complexity. Some are time consuming and require specialized laboratory equipment, such as calorimetric method [Schroeder06] that requires the use of high power sources and thermal insulation boxes. Other measurement methods are known to be easy to implement, nevertheless they can become very costly if the structure of the antenna is complex, as in the case of the resistance comparison method [Smith77]. Most of the known antenna radiation efficiency measurement methods are valid in a relatively narrow bandwidth and are dependent on the antenna circuit model (in general, most antennas can be modeled by series or parallel resonant circuit models). Therefore they are not very suitable for radiation efficiency measurement of UWB antennas because the UWB frequency range expands to several octaves where serial and parallel resonant circuit antenna models are interlaced along the frequency band.

Among the known narrowband measurement techniques the Wheeler cap method [Wheeler59] has become the standard because of its repeatability and simplicity of implementation. However, it assumes a pure series RLC equivalent circuit antenna model which is purely resonant, and so in principle this kind of method is not well

suiting for UWB antennas. This is why several authors proposed modifications of the Wheeler cap method, intending to increase the measurement accuracy [Johnston98], [McKinzie97] or measurement bandwidth [Schantz01].

McKinzie proposed an improvement to the Wheeler cap method forcing either a series or parallel RLC circuit model in the proximity of the resonance [McKinzie97]. This is achieved by rotating the measured reflection coefficient data in the Smith chart. The McKinzie method improves the measurement accuracy but remains valid only for a relatively small bandwidth in the vicinity of the resonance.

In order to outline the properties of some of the above-mentioned radiation efficiency measurement methods, we realized some preliminary measurements shown here that gave an idea of how these conventional methods behave in a very wide frequency range. In our experiments we used a conventional 800 MHz resonant straight wire monopole of constant radius $r = 0.28$ mm and $length = 92$ mm over a 60 cm by 60 cm aluminum ground plane, fed by standard SMA connector, as a test antenna. The monopole was made of copper wire and should attain radiation efficiency values approaching 100%, as obtained by numerical simulation using NEC [Burke81].

In the following measurements (Wheeler and McKinzie methods), an aluminum tube of $diameter=23$ mm and $length=120$ mm, shown on Figure 2.3a) was used as a Wheeler cap. The first resonance of this cap was found at 7.67 GHz.

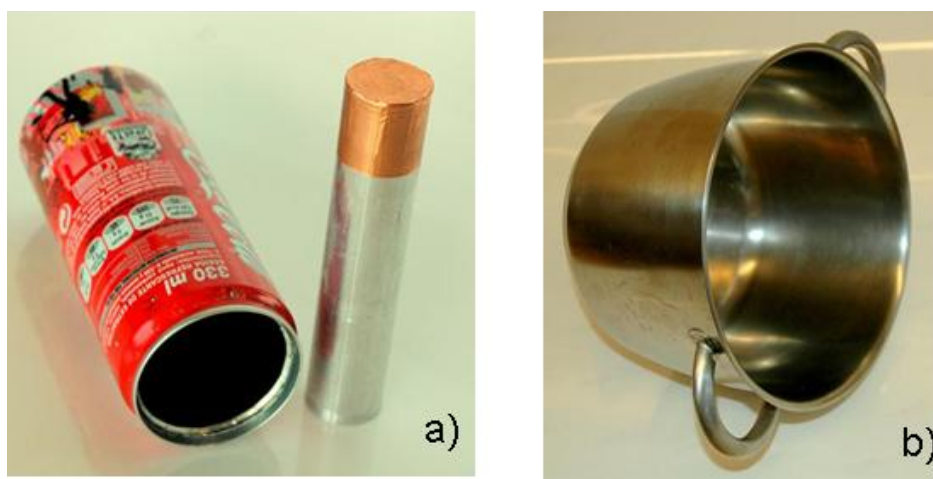


Figure 2.3: Different Wheeler caps used for radiation efficiency measurements: a) 2 cylindrical caps (beverages can $L=147$ mm, $d=58$ mm, $f_{1}^{st_{res.mode}}=4.4$ GHz the aluminum tube $L=120$ mm $d=23$ mm, $f_{1}^{st_{res.mode}}=7.67$ GHz), b) stainless steel pot used as cap for Schantz method

The Wheeler Cap Method: The Wheeler efficiency measured for 1601 frequency points in the frequency range from 100 MHz to 11 GHz shows several notches¹ and steep nulls on Figure 2.4, (green dotted line). The notches are due to the resonance frequencies of the cavity used as a cap whereas the steep nulls are due to the high resistances seen from the input port of the antenna within the cap and lead to efficiencies lower than 0% (which obviously makes no physical sense). The model proposed in [Geissler03] explains these high resistance figures due to the distance between the cap and the antenna.

The McKinzie Method: The McKinzie method is based on the Wheeler cap principle. In the case of the standard straight wire monopole the series RLC model should be applied. This is achieved by rotating the measured reflection coefficient S_{11} in the Smith chart and fitting the measured data to partially follow constant resistance circumferences [McKinzie97]. In this particular case of a series resonant antenna, the McKinzie method (Figure 2.4, blue continuous line) gives more stable values of radiation efficiency especially in those frequencies where Wheeler's method can not be applied. The method seems to work correctly up to 7.67 GHz where the notch of the first resonance of the cap appears. These efficiency notches are attributed to the high losses of higher order modes operating near their cutoff frequency [Johstonn03]. The efficiency peaks at frequencies below 500 MHz in the Wheeler cap and McKinzie methods are due to the inaccuracy of network analyzers when antenna impedances are low as well as to the proximity of the antenna to the cap.

The Schantz Method: Schantz [Schantz01] proposed an extension of Wheeler cap measurement technique to UWB antennas, where the main difference with the original Wheeler method is that the antenna radiates and reabsorbs the energy reflected back by the cap. In the measurement using Schantz method a stainless steel pot of *diameter*=230 mm and *length*=140 mm shown on Figure 2.3b) was used as a cap. Thus the low frequency cutoff of the cap is around 400 MHz. In the case of the 800 MHz monopole this method shows significant variations of efficiency (red stars

¹ NOTE: We use the term “notch” as a curve variation that has a physical sense, whereas “steep null” would be the variation that falls into values that have no physical sense. In the case of radiation efficiency the “notch” means variation that remains within the range 0-100% and “steep null” falls below 0%, as mentioned in [Geissler03] and [Johnston03]

on Figure 2.4). The efficiency values get close to the simulated efficiency (red dash-dotted curve), only at multiples of resonant frequencies of the monopole in free space.

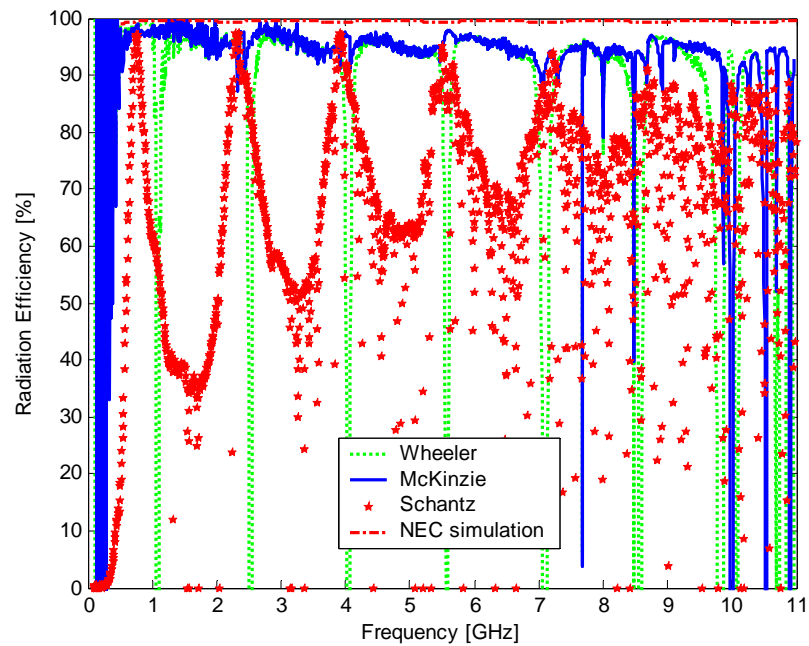


Figure 2.4: Comparison of the simulated radiation efficiency of a 92 mm-long, 800 MHz resonant straight wire monopole of constant radius $r=0.28$ mm, to the values measured using three different methods [Miskovsky09]

To summarize, the difficulty with the traditional measurements based on Wheeler cap principle is that the size of the cap depends on the particular frequency of interest. From the methods recalled in the previous paragraphs for a particular example of an 800 MHz wire monopole, only McKinzie method seems to give reasonably stable values up to the frequency of the first resonance of the cap.

To overcome the limitation of the circuit dependent measurement methods which is the validity in a small bandwidth around the antenna resonance, Johnston [Johnston98] described a reflection method without the need of any assumption on the antenna equivalent circuit model. Johnston's technique is based on a variation of the physical dimensions of the cap and so it is a little bit cumbersome measurement procedure. As an improvement of this method, Geissler [Geissler03] used a similar circuit approach but considerably simplifying the technique proposed by Johnston: the variation of the cap dimensions was replaced by a frequency variation. This measurement method developed by Johnston and improved by Geissler was applied for measurement of narrowband antennas. The question that comes out is whether this

method being independent of the antenna loss mechanism circuit model is applicable in a very large bandwidth such as UWB. The potential of the Johnston-Geissler (J-G) method for the measurement of radiation efficiency of UWB antennas should be experimentally tested.

2.2. Objectives of the thesis

The aims of the thesis resulting from issues outlined in the section 2.1 are defined in this chapter.

A need of direction-independent antenna distortion descriptors was identified. As suggested in the section 2.1, such descriptors should assess the antenna performance in terms of transmitted UWB pulse fidelity. This kind of direction-independent antenna descriptors would be very useful in antenna optimization since it would resume its performance in a single number. Consequently, a definition and analysis of such descriptors is the first aim of the thesis. The usefulness of the proposed descriptors is then demonstrated by their application in UWB antenna optimization, performed by numerical simulation. In addition, the measurement procedure of one improved antenna fidelity descriptor is outlined and its validity assessed when compared with simulations.

A requirement of a convenient antenna radiation efficiency measurement method for UWB frequency range was discussed as well. This issue identifies the second aim of the thesis, which is a critical analysis of the most common antenna efficiency measurement methods in a wide frequency range. An enhancement of one of the existing radiation efficiency measurement procedures to UWB frequency range is proposed.

Finally, to confirm the optimized UWB antenna performance experimentally, several antennas were manufactured and the measurements, using the abovementioned methods are presented.

After the review of historical background in Chapter 1 and identification of scientific issues in Chapter 2, the objectives of the thesis are resumed and each of them treated as follows:

-
- Definition and analysis of improved, direction-independent UWB antenna descriptors is developed in Chapter 3
 - Critical analysis of the proposed UWB antenna descriptors measurement methods is shown in Chapter 4.
 - In Chapter 5 a demonstration of the practical use of direction-independent descriptors in UWB antenna design and optimization is given.
 - Fabrication and measurement of the designed UWB antenna is detailed in Chapter 6

Finally, the concluding remarks and research perspective are given in Chapter 7.

RESULTS

3. DESCRIPTORS FOR UWB ANTENNA PERFORMANCE ASSESSMENT

The theoretical and experimental results presented in this chapter concern the first aim of the thesis. Improved direction-independent UWB antenna descriptors will be defined and experimentally analyzed on several antennas. The results presented in this chapter were published in [Miskovsky07a] and [Miskovsky06].

3.1. Formulation for a Single Antenna

In UWB systems using correlation detection, the received pulse is being correlated with a template pulse form. In this case the received pulse shape is one of the most important parameters, on which depends the overall system performance.

3.1.1. Spatially Averaged Fidelity – SAF_I

For the basic formulation, a single antenna is considered as depicted in Figure 3.1, driven by a voltage source $V_G(f)$ having an internal impedance $Z_G(f)$.

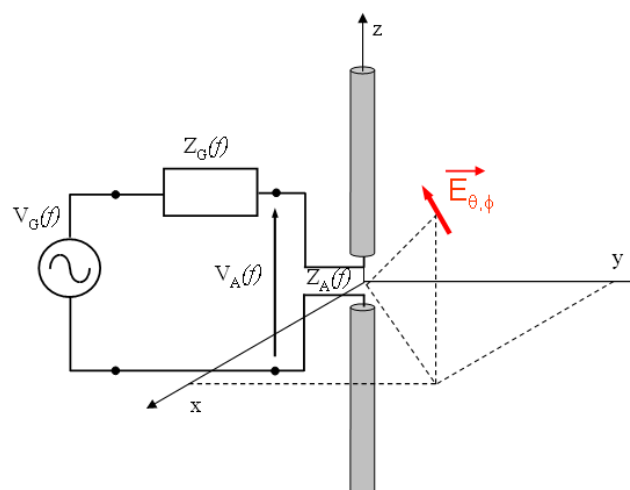


Figure 3.1: Single antenna configuration [Miskovsky07a]

To evaluate the performance of a single antenna we propose to use a new figure of merit called Spatially Averaged Fidelity (SAF_I) and defined by the expression (3.1). The definition of SAF_I is based on the principle proposed by McLean in (2.3) and takes an average over a hypothetical sphere that surrounds the antenna. Nevertheless, expression (2.3) could be slightly modified to average only a region in the surrounding space where the pulse radiated ought to match a given template.

$$SAF_I = \frac{\int_{-\infty}^{\infty} \left| \int_0^{2\pi} \int_0^{\infty} \vec{E}(t, \theta, \phi) \cdot T(t) \cdot \vec{a}(\theta, \phi) dt \right|^2 R^2 \sin \theta d\theta d\phi}{\int_{-\infty}^{\infty} |T(t)|^2 dt \cdot \int_0^{2\pi} \int_0^{\infty} \left| \vec{E}(t, \theta, \phi) \right|^2 dt R^2 \sin \theta d\theta d\phi} \quad (3.1)$$

In the numerator of (3.1), the fidelity SAF_I correlates the total radiated field \vec{E} at a distance R with a conveniently selected template T in all directions. Then a spatial averaging is realized in order to summarize the antenna performance direction-dependence, in a single number. In the numerator of equation (3.1), only the part of the total radiated energy of the field \vec{E} correlated with the template T , is considered. This quantity is averaged over all angular directions (θ, ϕ) . As stated by McLean [McLean05], the template can be formulated as a product of a time-varying scalar function $T(t)$ and unit vector \vec{a} expressing the polarization of the receiving antenna. The denominator of expression (3.1) normalizes SAF_I by the respective energies of the template and the total radiated field. Proceeding this way, the maximum value of SAF_I could be 1.

The shape of a template is arbitrary, but a reasonable choice could improve the angular performance of the antenna [McLean05], also in terms of SAF_I .

During the development of this thesis, in 2006 Dissanayake [Dissanayake06] proposed almost identical figure of merit called Pattern Stability Factor (PSF).

3.1.2. Application of SAF_I

The performance of an antenna can dramatically change with a given template. In order to assess this fact and to verify the applicability of SAF_I , we have compared three antennas: a quarter-wavelength monopole at 6.5 GHz (11.5 mm), an UWB conical monopole (about the same height), and an UWB ridge horn antenna. The

schematic representation of the tree antennas is shown on Figure 3.2. The reflection coefficients of the three antennas are shown on Figure 3.3. The UWB conical monopole, as well as the ridge horn antenna, has a very good matching within the frequency band defined by the FCC.

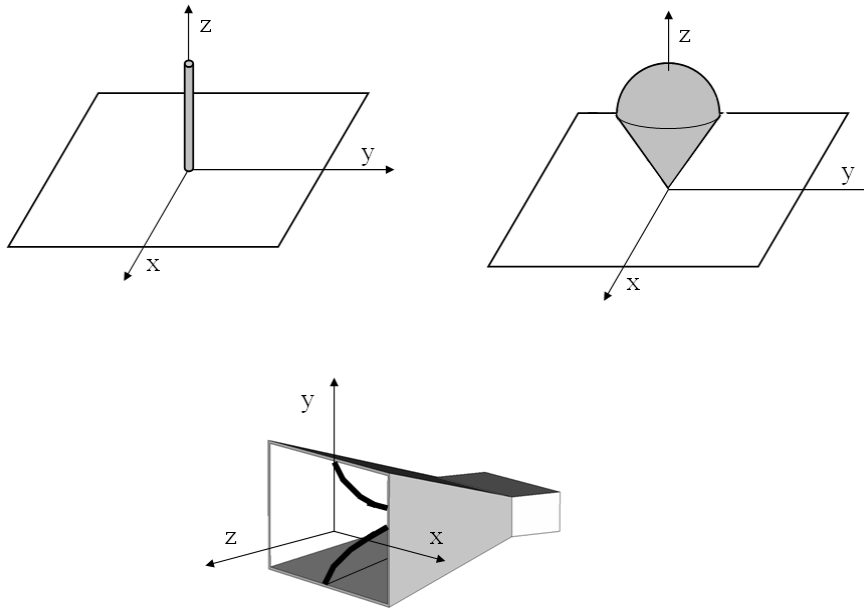


Figure 3.2: Schematic representation of the three tested antennas a) $\lambda/4$ monopole, b) UWB conical monopole, c) ridge horn antenna

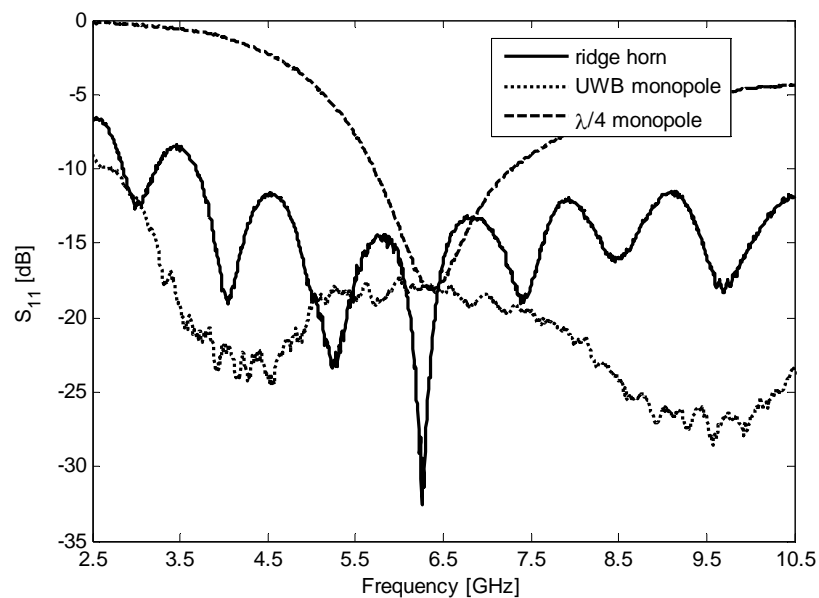


Figure 3.3: Measured reflection coefficients of the three compared antennas: ridge horn, UWB conical monopole and $\lambda/4$ monopole

The electric fields radiated by the three antennas were measured in an anechoic chamber, in a range from 2.5 GHz to 10.5 GHz with 10 MHz frequency step. The symmetry of the radiation patterns was taken into consideration in order to reduce the computation load.

In order to avoid the perturbing influence of the measurement system on the performance of the ridge antenna, only the broadside hemisphere was measured. As a feeding pulse, an ideal wideband pulse having flat spectrum within the bandwidth from 2.5 GHz to 10.5 GHz, was used. Its time domain representation is shown on Figure 3.4. In this chapter we will not describe all the details concerning the measurement procedure of averaged fidelity SAF_I . The most important considerations on measurement setup and template function to be taken into account will be detailed in the following chapter.

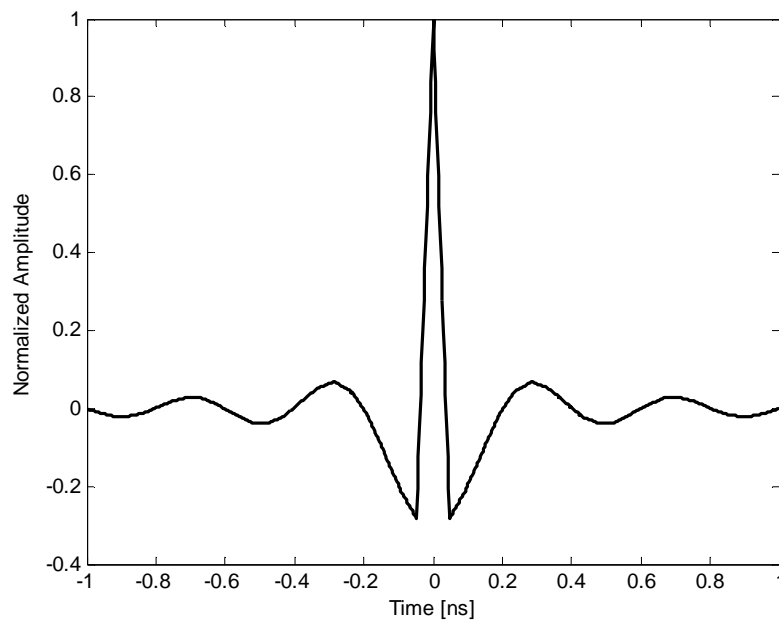


Figure 3.4: Time domain representation of the antenna feeding pulse, having a flat spectrum within the FCC UWB frequency range (2.5 GHz - 10.5 GHz).

Dependence of SAF_I on the template: To show the variation of SAF_I with the template an illustrative example is given in Figure 3.5.

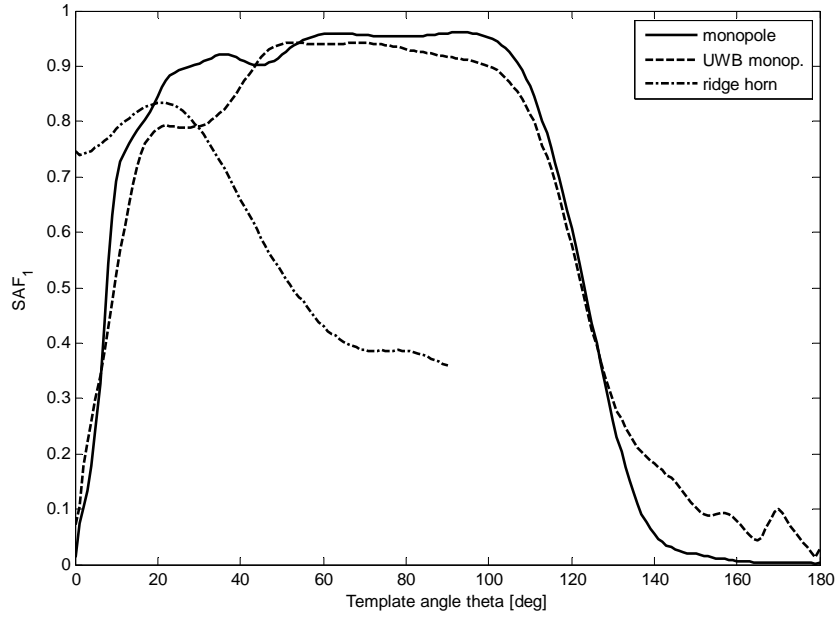


Figure 3.5: The fidelity SAF_I as function of different templates in FCC UWB frequency band. The template used in SAF_I computation is the shape of the pulse radiated in the direction given by the angle θ [Miskovsky07a]

As a template we used the electromagnetic pulse radiated by each antenna in the direction defined by the abscissa of angle θ . From the point of view of SAF_I , over a large range of templates, the quarter-wavelength monopole (solid line) has a similar performance as the UWB monopole (dashed line) and more stable than UWB ridge horn antenna (dash-dotted). This result does not mean that the antenna is a good UWB antenna, but that the shapes of the radiated pulses are quite similar in all directions. So, for this particular type of template, the quarter-wavelength monopole and UWB conical monopole are less sensitive on template variation, and they distort less the radiated pulse than the ridge horn.

For better understanding of SAF_I results from Figure 3.5, the pulses radiated by each of the three antennas at specific angular directions θ are shown in Figure 3.6. The pulse shapes radiated by the $\lambda/4$ resonant and UWB monopoles are compared at angular directions $\theta=45^\circ$, 70° and 100° . In the case of $\lambda/4$ resonant monopole shown in Figure 3.6-a, the three pulse shapes are very similar to each other, which confirms

the stable values of SAF_I in the range between $\theta=45^\circ$ and $\theta=100^\circ$, shown in Figure 3.5. Similarly, in the case of UWB monopole, the pulses from Figure 3.6-b are very similar at 45° and 70° . At 100° , where the SAF_I performance starts to decrease (see Figure 3.2) the pulse shape is more distorted. In the case of ridge horn antenna (Figure 3.6-c) the pulses at $\theta=20^\circ$, 50° and 80° show important shape differences, the fact that explains the variation of SAF_I shown in Figure 3.5.

In order to give a more general idea of how the three antennas radiate and distort the UWB pulses, a 3-dimensional (3D) time domain representation of radiated pulses is shown on Figure 3.7. Each 3D image is completed by upper view, for easier analysis. An interesting observation can be made in the case of monopoles, Figure 3.7 a) and c). For angular directions from $\theta=90^\circ$ to $\theta=180^\circ$ corresponding to the zone below the ground plane, the radiated pulses are slightly delayed. This delay is due to the monopole's ground plane that for these specific angular directions appears between the measured antenna and the measurement probe.

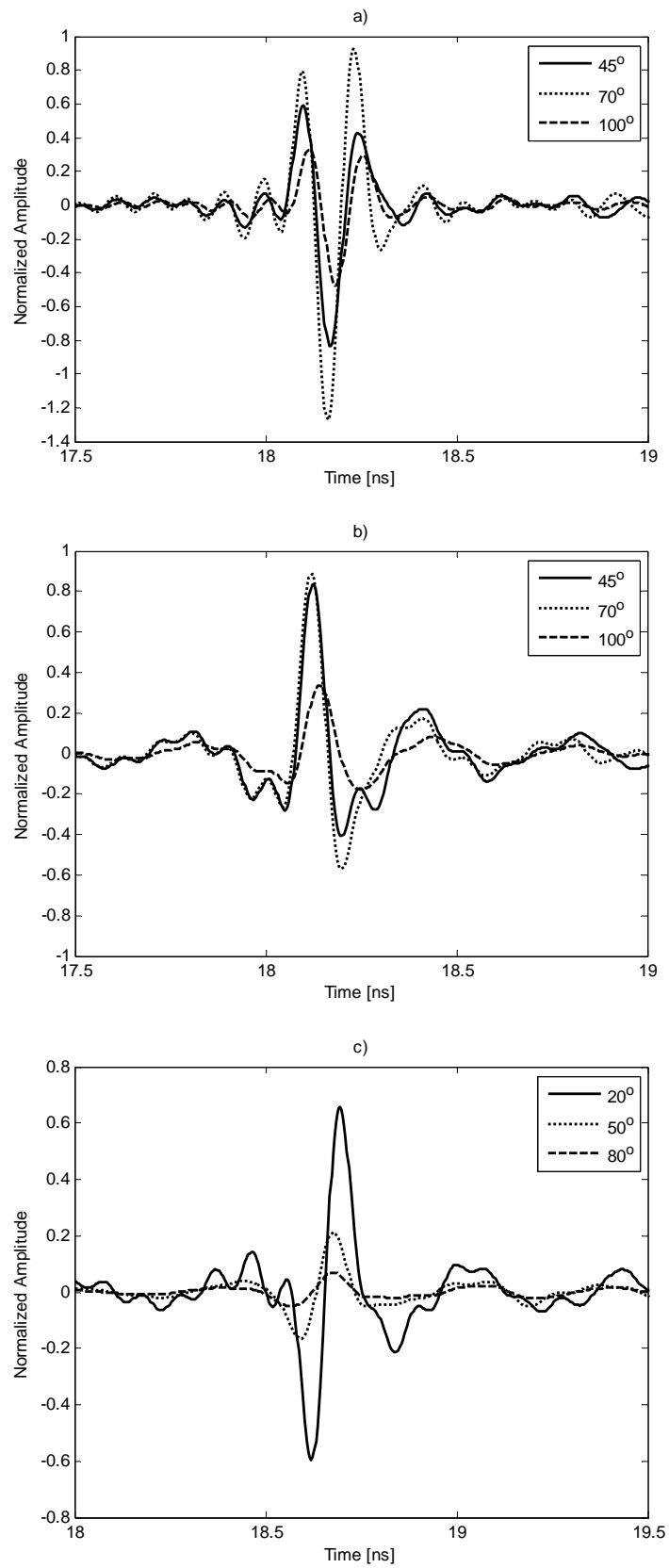


Figure 3.6: Measured radiated pulse shapes at different angular directions θ , a) $\lambda/4$ resonant monopole, b) UWB conical monopole, c) ridge horn antenna. The feeding pulse is shown on Figure 3.4.

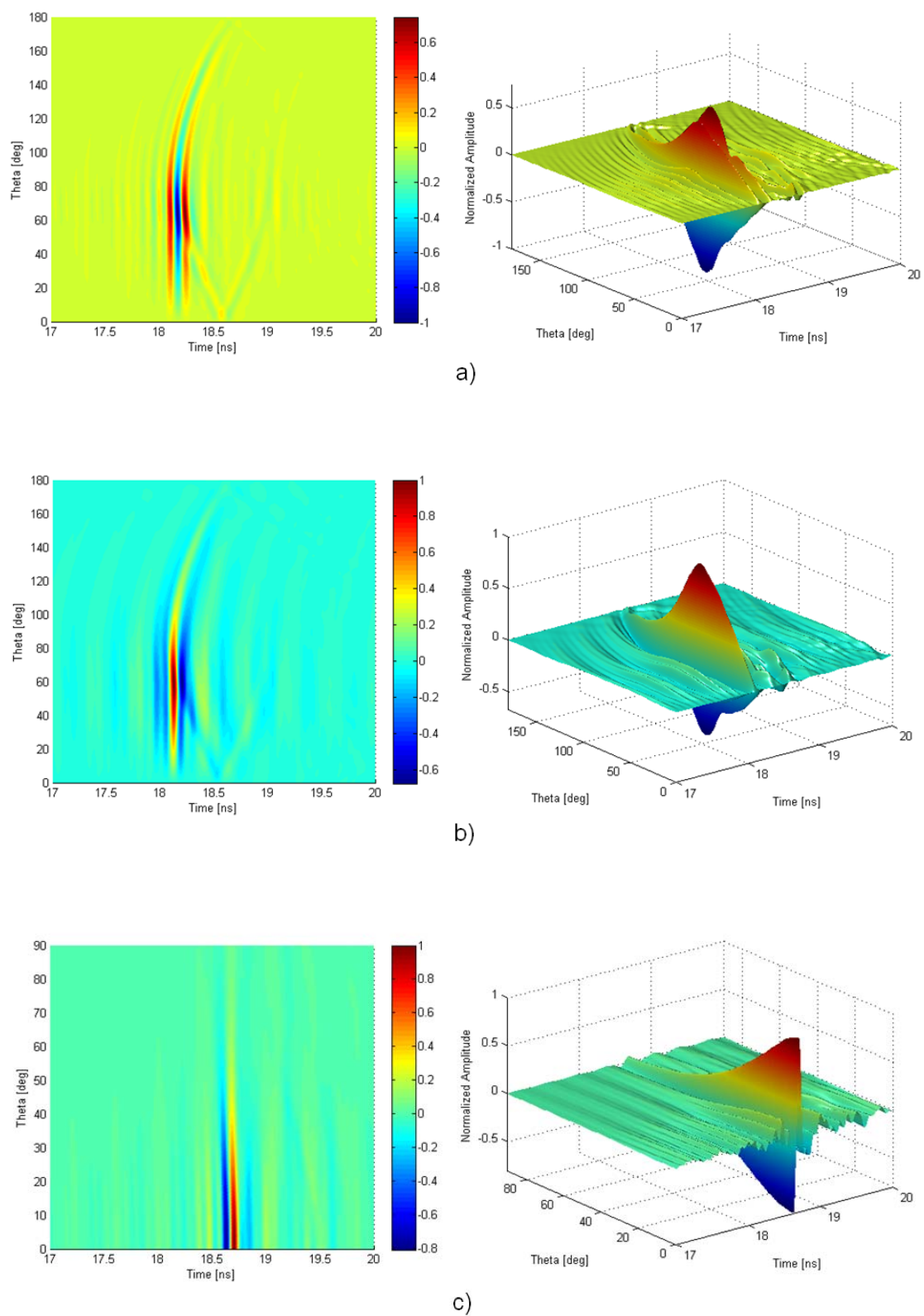


Figure 3.7: Measured pulses, radiated by the three antennas: a) $\lambda/4$ resonant monopole, b) UWB conical monopole, c) ridge horn. Feeding pulse is shown on Figure 3.4.

In order to compare the antennas performance in terms of SAF_I , another three UWB template types were used. The first template is an ideal pulse filling the UWB spectrum according to FCC. In time domain this pulse is a Sinc function. The second and third templates are the first and the second derivatives respectively of the Sinc function. The computed SAF_I for the three antennas under consideration with the mentioned pulses are presented in Table 3.1.

Table 3.1: Computed SAF_I , using the feeding pulse and its derivatives as templates [Miskovsky07a]

Template	UWB monopole	$\lambda/4$ monopole	Ridge horn
Sinc	0.63	0.83	0.61
Sinc derivative	0.11	0.05	0.08
Sinc 2 nd derivative	0.60	0.79	0.56

For all three analyzed antennas, the performance is similar when the Sinc or its second derivative is used as a template. This is due to the fact that both template shapes are almost the same. In the case of a template equal to the first Sinc derivative, the values of SAF_I are very low, though slightly better for the UWB monopole. The variation of the current distribution on the monopole changes significantly in such a wide frequency band. Consequently, the radiated pulses can not be considered as the perfect derivative of the input pulse, as commonly understood for narrowband monopoles. The ridge horn radiates a derivative of the feeding pulse but only within a narrow angular range, explaining the low figures of SAF_I for this antenna.

Dependence of SAF_I on the bandwidth: In order to demonstrate the influence of the integration bandwidth on SAF_I performance, the European UWB indoor standard bandwidth, ranging from 6 GHz to 8.5 GHz, was considered [Com07]. As a feeding pulse, an ideal wideband pulse filling the spectrum from 6 GHz to 8.5 GHz was used. Its time domain representation is shown on Figure 3.8.

In the same way as for the FCC UWB spectrum (see Figure 3.5), different templates were used, within the same measurement setup comparing the performance of the three antennas. The variation of SAF_I as a function of the pulse radiated by each antenna in the direction defined by the abscissa angle θ is shown on Figure 3.9. In the zone above the monopoles ground plane (θ going from 0° to 90°), the SAF_I curves are

slightly more uniform with respect to those shown on Figure 3.5. In this particular case, using a variable template, a quarter-wavelength monopole and UWB monopole seem to be less sensitive to template variation. The ridge horn antenna SAF_I performance changes more rapidly with the template than in the previous case (Figure 3.5).

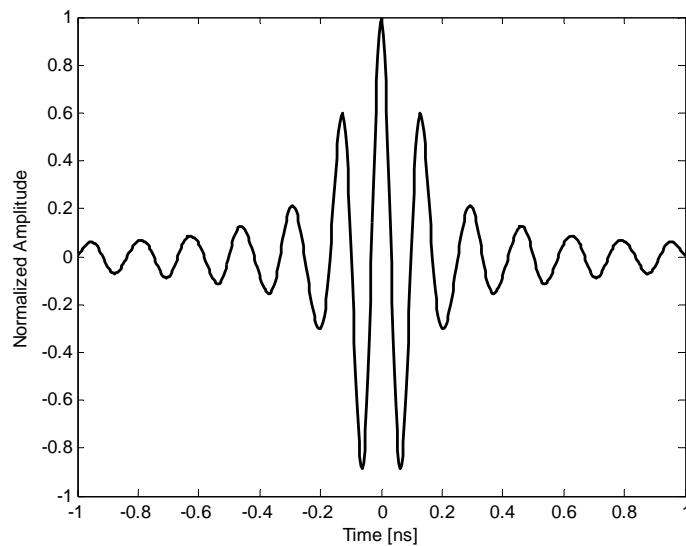


Figure 3.8: Time domain representation of the antenna feeding pulse, having a flat spectrum within the European UWB indoor frequency range (6 GHz - 8.5 GHz).

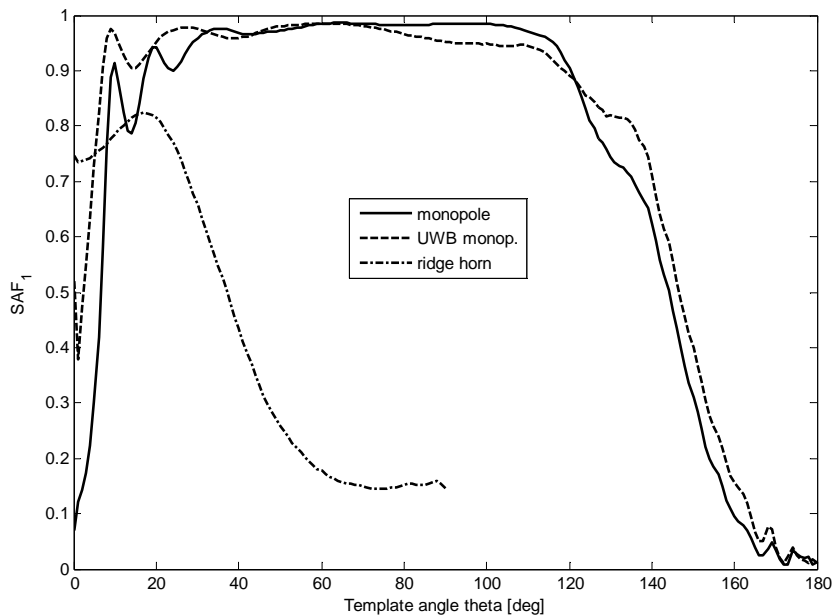


Figure 3.9: The measured average fidelity SAF_I as function of different templates in European UWB frequency band. The template is the shape of the pulse radiated in the direction given by the angle theta [Miskovsky07a].

As in the previous case (FCC UWB spectrum), the pulses radiated by each of the three antennas at specific angular directions θ are shown in Figure 3.10. The pulse shapes radiated by the $\lambda/4$ resonant and UWB monopoles are compared at angular directions $\theta=45^\circ$, 70° and 100° . The three pulse shapes are very similar to each other, which confirm the stable values of SAF_l , shown in Figure 3.9. The pulse shapes radiated by the ridge horn antenna at $\theta=20^\circ$, 50° and 80° show significant differences, as was expected from SAF_l values at corresponding angular directions shown in Figure 3.9. The 3D representation of radiated pulses is shown on Figure 3.11. The radiated pulses time delay due to the monopoles ground plane (similar to the previous case with FCC UWB pulses, Figure 3.7) can be observed on Figure 3.11 a) and b).

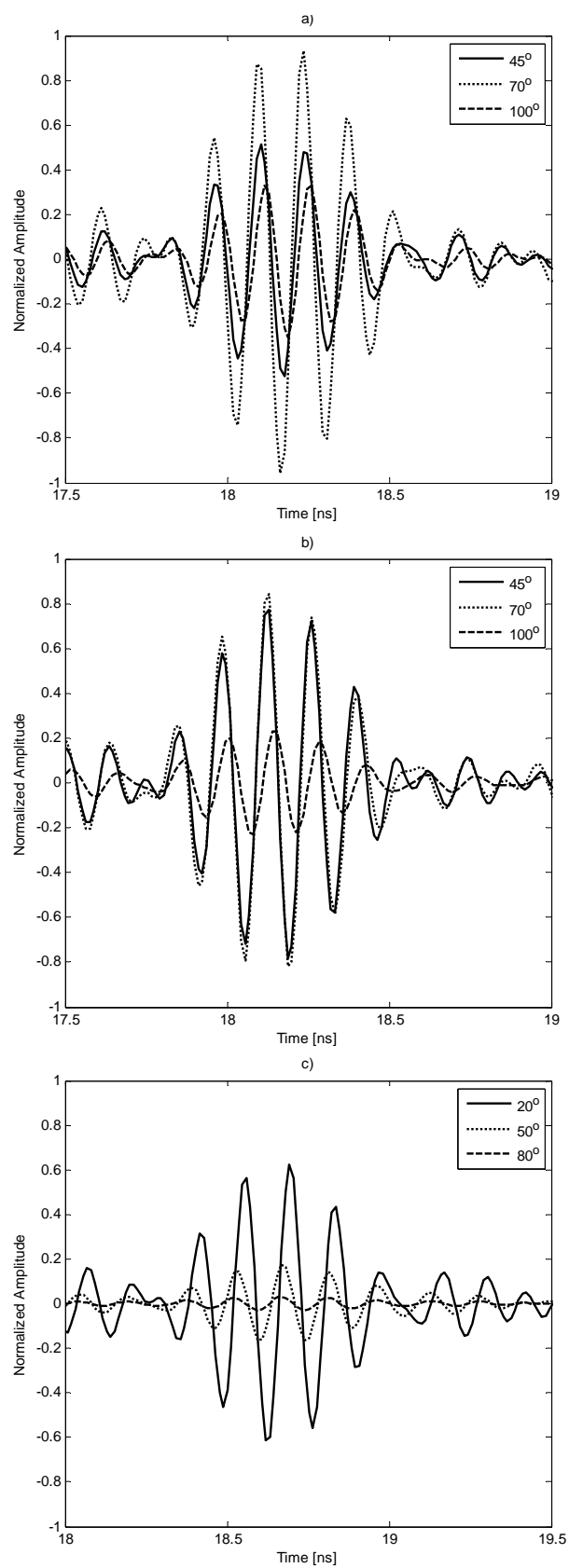


Figure 3.10: Measured radiated pulse shapes at different angular directions θ a) $\lambda/4$ resonant monopole, b) UWB conical monopole, c) ridge horn antenna. The feeding pulse is shown on Figure 3.8.

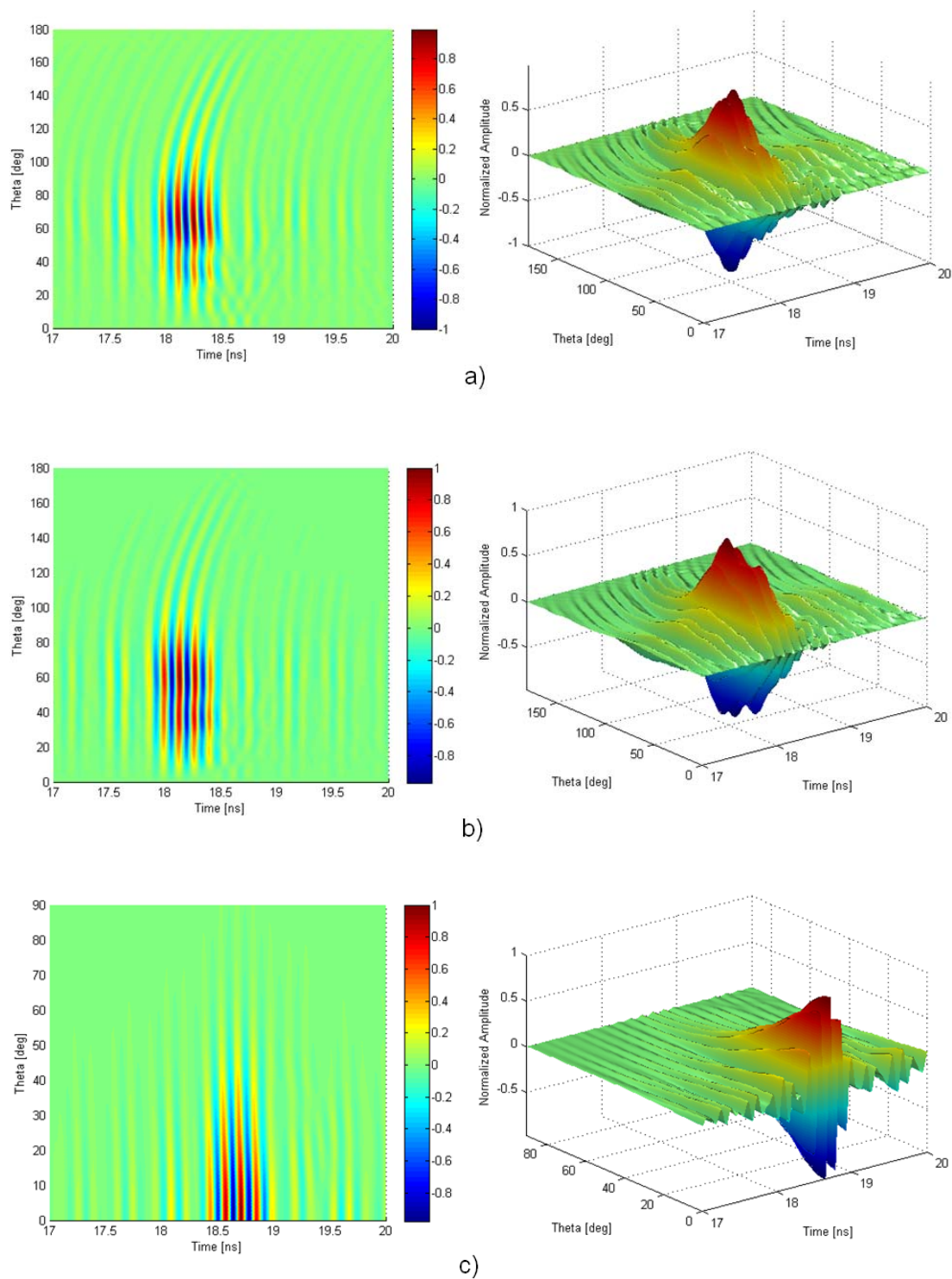


Figure 3.11: Measured pulses, radiated by the three antennas: a) $\lambda/4$ resonant monopole, b) UWB conical monopole, c) ridge horn, in 3D view and upper view. The feeding pulse is shown on Figure 3.8.

As in the case of FCC UWB spectrum in the previous section, different template types were compared in terms of SAF_I , using the European UWB band. The results are represented in Table 3.2. Basically three observations can be made:

- the quarter-wavelength monopole seems to perform in the same way as when using a template respecting the FCC UWB frequency range
- both antennas (UWB monopole and ridge horn) attain higher value of SAF_I when using 1st derivative of a Sinc function as a template (0.47 and 0.42 respectively). This seems to indicate that when a narrower bandwidth is considered in the antenna SAF evaluation, the antenna *derivates* better the input pulse. Surprisingly, as shown in Table 3.2, a quarter-wavelength monopole which is a resonant narrowband antenna attains the highest values of fidelity when the Sinc function pulse is used as a template. Here it is important to remark, that the radiation efficiency and the antenna matching are not considered in SAF_I computation.
- as in the previous case of FCC UWB spectrum (shown on Table 3.1), the performance is similar when the Sinc and its second derivative are used as template, because their shapes are very similar

Table 3.2: SAF_I for the European frequency band and different templates [Miskovsky07a]

Template	UWB monopole	$\lambda/4$ monopole	Ridge horn
Sinc	0.29	0.91	0.50
Sinc derivative	0.47	0.04	0.42
Sinc 2 nd derivative	0.36	0.82	0.48

Dependence of SAF_I on the integration angle: The definition of SAF_I should not be restricted to averaging over a whole sphere surrounding the antenna. The value of SAF_I is direction-independent as defined by the equation (3.1), but we can say that it can be dependent on operating directions of the antenna (θ, ϕ). Thus SAF_I value could be slightly modified if the averaging would be considered only in a reduced region of the space. This region could be specified as a region where the radiated pulse ought to match a given template or as a main beam region of a directive antenna. For example, in the case of the ridge horn antenna, the value of SAF_I using a second derivative of

Sinc function as a template can attain 0.78, when the integration angle θ is considered from 0° to 20° , contrary to the value from the Table 3.2, where the angle θ goes from 0° to 90° . A judicious choice of integration angle can improve the performance of the antenna in terms of SAF_I . Moreover it allows to better describe the problem to face, which is the maximization of the SAF_I value in a reduced region, defined for example by the main beam or the position of the receiver.

3.2. Formulation for a Transmit-Receive System

In a real UWB system, where transmitting and receiving antennas are used, not only the radiated waveform respecting the FCC mask [FCC02] is of significant interest, but also a special attention should be given to the pulse waveform delivered to the receiver load.

An UWB system having one transmitter antenna and one receiver antenna, as depicted on Figure 3.12, is considered.

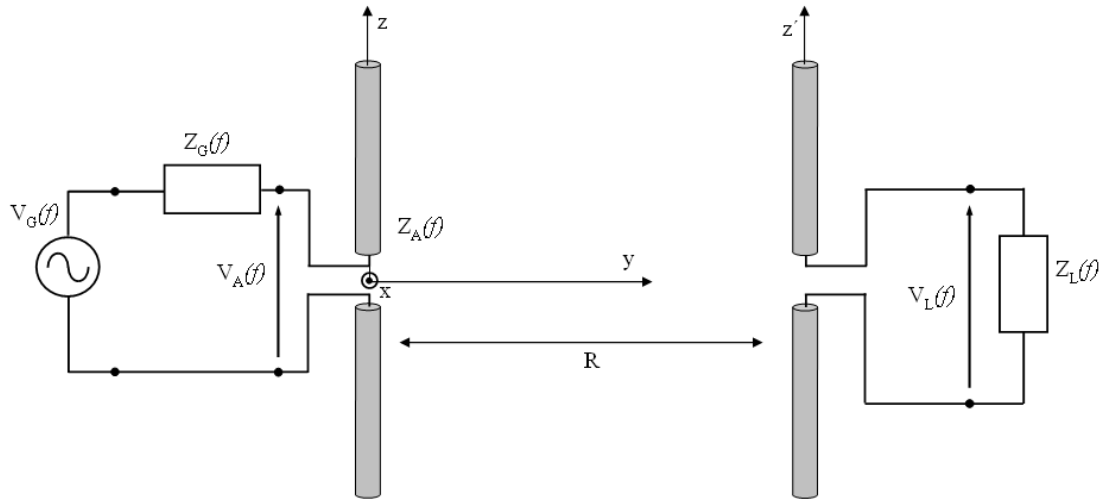


Figure 3.12: UWB system configuration: transmitting subsystem at left and receiving subsystem at right [Miskovsky07a]

The transmitter antenna is driven by a voltage source $V_G(f)$, having an internal impedance $Z_G(f) = R_G(f) + jX_G(f)$. The receiver antenna is loaded by impedance $Z_L(f) = R_L(f) + jX_L(f)$ and has a terminal voltage $V_L(f)$. The input impedance of the transmitter antenna is $Z_A(f) = R_A(f) + jX_A(f)$. The antennas are separated by a distance

R . In the context of figures of merit defined in this chapter, the distance R is not necessarily a far-field distance as usual, a fact that can influence on the proper input impedance of the antenna and so the way the pulse is radiated.

For the evaluation of the antenna performance within a system like described in Figure 3.12 we propose two figures of merit: *Spatially Averaged Fidelity* (SAF_2) and *Averaged Energy Efficiency* (AE). The procedure for SAF_2 and AE evaluation is the same as in the case of SAF_1 , placing the receiver subsystem in all angular positions (θ, ϕ) around the transmitting subsystem. For the purpose of simplicity the receiver antenna is considered having always the same polarization as the transmitter antenna.

3.2.1. Spatially Averaged Fidelity - SAF_2

In the same way as for SAF_1 , a Spatially Averaged Fidelity (SAF_2) of the received pulse at receiver load can be defined by the expression (3.2) for the complete system shown on Figure 3.12. In this case the correlation is done between the voltage on the load and the template.

$$SAF_2 = \frac{\int_0^\infty \int_0^{2\pi} \int_0^\pi \left[\int_{-\infty}^\infty V_L(t, \theta, \phi) \cdot T(t) dt \right]^2 R^2 \sin \theta d\theta d\phi}{\int_{-\infty}^\infty |T(t)|^2 dt \cdot \int_0^\infty \int_0^{2\pi} \int_0^\pi [V_L(t, \theta, \phi)]^2 dt R^2 \sin \theta d\theta d\phi} \quad (3.2)$$

This equation gives more realistic description of the antenna performance than the equation (3.1) for the SAF_1 . Voltage at load terminal $V_L(f)$ implicitly accounts for the frequency variations of the system due to the mismatch between the voltage source and the transmitting antenna, the mismatch between the receiving antenna and the load, and the radiation patterns of both antennas. The value of the parameter SAF_2 also depends on the coupling between the transmitting and receiving antennas, and on the values of source and load impedances. A high value of SAF_2 would mean a high degree of similitude between the template and the received pulse at the load (at all directions of space with respect to the transmitting antenna). Unfortunately, although SAF_2 directly describes the shape distortion of the received pulses, it does not describe explicitly the efficiency of the system. In such a wide operation bandwidth, the antenna radiation efficiency dependence on frequency is not negligible, and its influence on pulse distortion is included within the voltage at load terminal $V_L(f)$.

3.2.2. Averaged Energy Efficiency – AE

For a single antenna the radiation efficiency (3.3) is defined as the ratio of the radiated energy (measured at a distance R from the antenna) to the energy of the pulse delivered from the generator to the transmitting antenna. Z_0 represents the impedance of the free space Z_A is the input impedance of the transmitter antenna and R_A is its real part.

$$\eta = \frac{\int_0^{2\pi} \int_0^\pi \int_{-\infty}^\infty |\vec{E}(f, \theta, \phi)|^2 df R^2 \sin \theta d\theta d\phi}{Z_0 \int_{-\infty}^\infty \left| \frac{V_A(f, \theta, \phi)}{Z_A(f, \theta, \phi)} \right|^2 R_A(f, \theta, \phi) df} \quad (3.3)$$

Similarly to this definition, an *Averaged Energy Efficiency (AE)* is defined by the expression (3.4). The numerator of (3.4) takes into consideration the spatially averaged energy delivered to the receiver load and the denominator considers the spatially averaged energy of the pulse delivered from the generator to the transmitting antenna. In both expressions, (3.3) and (3.4), the mismatch between the transmitting antenna and the generator is considered. The mismatch between the receiving antenna and the load is only present in expression (3.4).

$$AE = \frac{\int_0^{2\pi} \int_0^\pi \int_{-\infty}^\infty \left| \frac{V_L(f, \theta, \phi)}{Z_L(f)} \right|^2 R_L(f) df \sin \theta d\theta d\phi}{\int_0^{2\pi} \int_0^\pi \int_{-\infty}^\infty \left| \frac{V_A(f, \theta, \phi)}{Z_A(f, \theta, \phi)} \right|^2 R_A(f, \theta, \phi) df \sin \theta d\theta d\phi} \quad (3.4)$$

3.2.3. Application of SAF_2 and AE

In order to assess the applicability of the figures of merit described by expressions (3.2) and (3.4), they have been used to compare the performance of lossy dipole antennas within an UWB system configuration from Figure 3.12. For the simulation of such a system, the Numerical Electromagnetics Code (NEC) [Burke81] has been used. Different lossy dipoles were simulated in order to vary the energy efficiency AE of the system. Two dipoles of the same given conductivity σ [S/m] and of 10 cm length were placed at distance $R=5.46$ m. In order to compute the averaged fidelity SAF_2 as defined by the expression (3.2), the receiver dipole was placed in all angular

directions θ and ϕ being always tangent to the hypothetical sphere of radius R around the transmitter, such as schematically illustrated on Figure 3.13. For purpose of simplicity, the polarization of receiver antenna is the same as the polarization of the transmitter antenna.

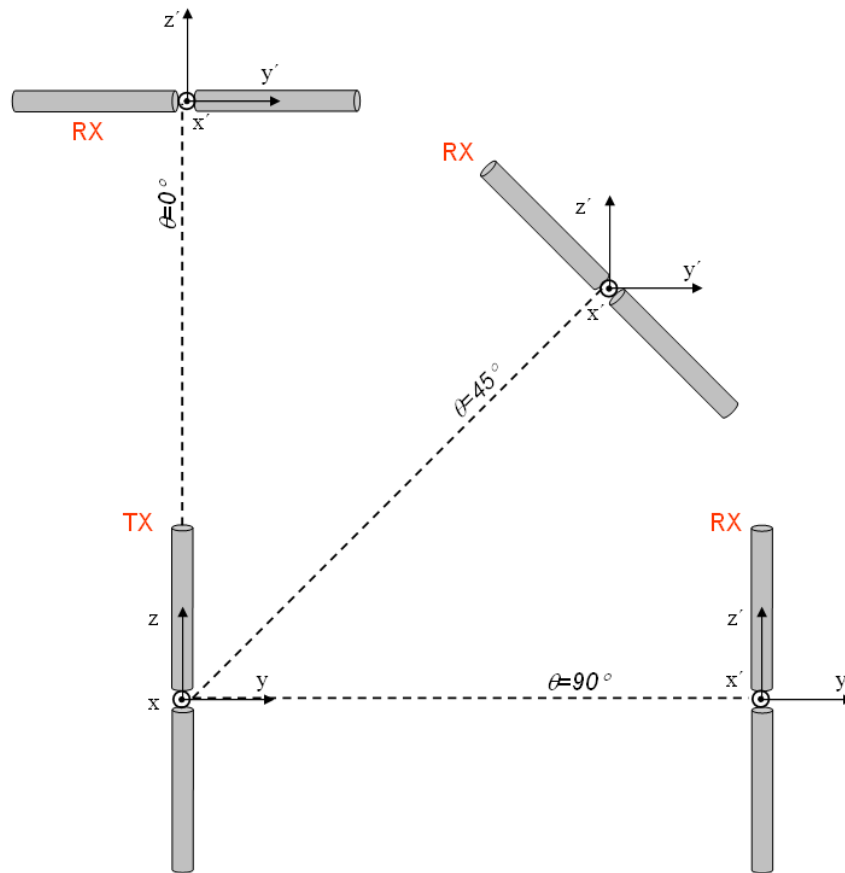


Figure 3.13: Schematic representation of the receiver (RX) antenna positioning respect to transmitter (TX) antenna, in the NEC simulation assessing the SAF_2 and AE performance

The generator internal impedance and receiver antenna loading were assumed constant ($R_G = R_L = 50\Omega$) over the whole operational frequency range. In order to use more realistic UWB pulse such as Gaussian and Rayleigh monocycles or Gaussian doublet [Zhuang03], the Rayleigh monocyte pulse of natural width of 100 ps was used as a generator pulse and its derivative, the Gaussian monocyte as a template at the receiver. Both pulses are shown on Figure 3.14.

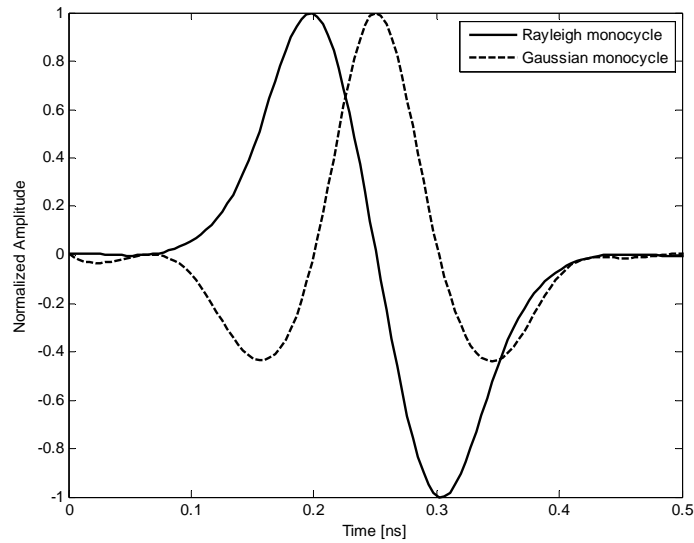


Figure 3.14: Rayleigh monocycle and Gaussian monocycle pulse shapes, used as generator and template pulse respectively

The reasons for using the Gaussian monocycle as a template are shown on the Figure 3.15. The transmit-receive system from Figure 3.12 was simulated for one angular direction (both monopoles aligned in the plane z - y at distance R) and the normalized pulse shapes at different stages of the system were schematically represented. As shown on Figure 3.15, the Rayleigh pulse fed into the transmitter antenna (V_A) gets slightly distorted for high conductivity ($\sigma=10^9$ S/m), when a ripple due to the mismatch reflection between the generator and the antenna appears. The influence of the antenna conductivity on the pulse distortion is much more visible at the voltage pulse shape (V_L) delivered to the receiver load. The received V_L pulse for low conductivity dipoles ($\sigma=10^2$ S/m) is clearly very similar to the Gaussian monocycle. The V_L pulse received with high conductivity dipoles ($\sigma=10^9$ S/m) is strongly distorted but partially it can be similar to the Gaussian monocycle. At this point a first observation can be made: using the Gaussian monocycle as a template should yield higher values of averaged fidelity SAF_2 for low conductivity dipoles than for high conductivity dipoles.

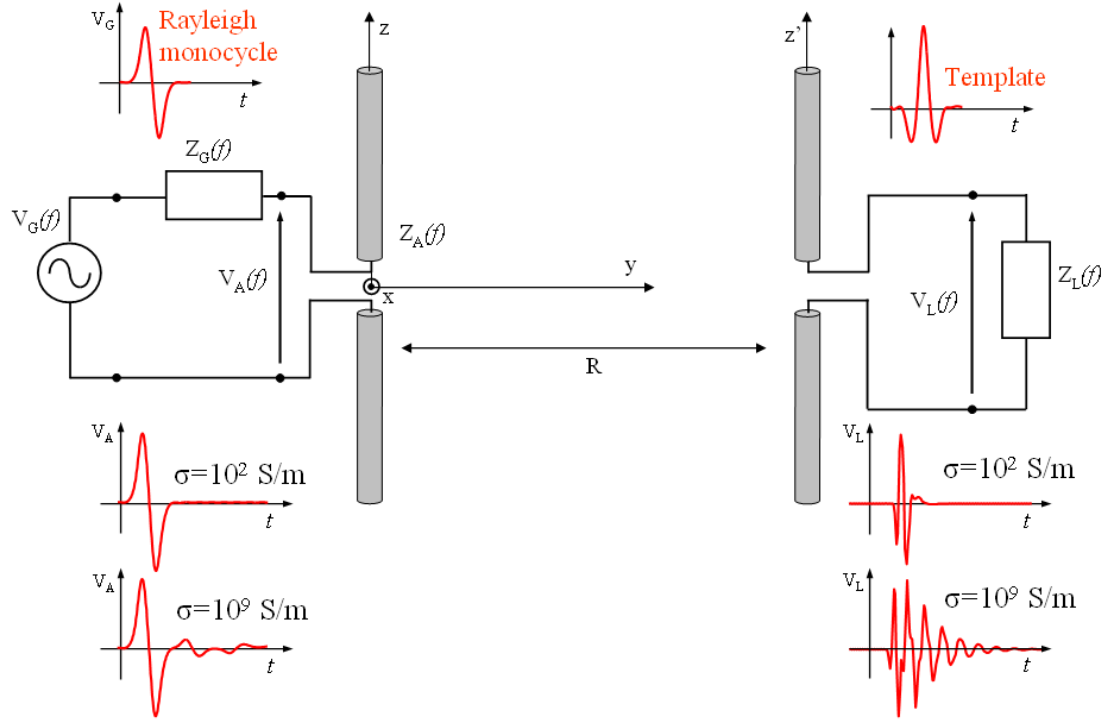


Figure 3.15: Pulse distortion within a transmit-receive system, using dipoles of different conductivities ($\sigma=10^2$ S/m and $\sigma=10^9$ S/m). Rayleigh monocycle used as generator pulse and the Gaussian monocycle used as template at the receiver.

The simulation results of averaged fidelity SAF_2 and normalized efficiency AE for two cases are shown on Figure 3.16. First, a constant conductivity was applied along the whole dipole (Figure 3.16 left). Second, a linearly variable conductivity dipole (Figure 3.16 right) was analyzed, with the conductivity decreasing from the center of the dipole toward the extremities. The value of conductivity on the horizontal axis (Figure 3.16 right), represents the maximum value of conductivity applied in the dipole center. When designing such dipoles, the optimum value of conductivity in both cases (constant and variable conductivity shown on Figure 3.16 left and right respectively) could be found as a compromise between the averaged efficiency AE and averaged fidelity SAF_2 at the intersection point of SAF_2 and normalized AE curves.

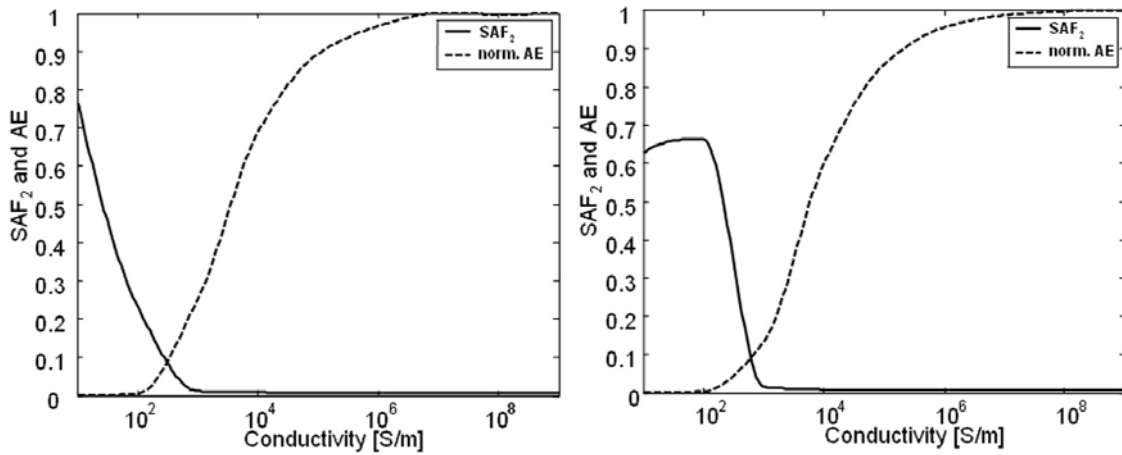


Figure 3.16: Simulated SAF_2 (continuous line) and AE (dashed line) for constant (left) and variable loading (right), [Miskovsky07a]

In this section, only a variable conductivity dipole from Figure 3.16 right is analyzed in detail. The transfer functions defined as $|V_L(f)/V_G(f)|$ and received pulse shapes, respectively for three values of conductivity (10^2 , 10^3 , and 10^7 S/m), are presented on Figure 3.17. For low conductivity, where SAF_2 is high (see Figure 3.16 right), the received pulse shown on Figure 3.17-b is very similar to the template (Gaussian monocycle) because the transfer function is highly wideband for all directions θ (Figure 3.17-a). The efficiency AE is poor (Figure 3.16 right), because of the high losses attenuating the transmitted pulse. For the high conductivity case, it is exactly the opposite (Figure 3.16 right). The narrower transfer function filters the transmitted pulse (Figure 3.17-e,f). For the optimum conductivity (10^3 S/m) the pulse suffers some distortion but is not excessively attenuated and still matches the template shape quite well (Figure 3.17-c,d). For this value of conductivity, the efficiency starts to increase and the fidelity is still quite high (see Figure 3.16 right).

For better representation of the direction dependent pulse shape distortion, the 3-dimensional normalized pulses at the receiver load are shown on Figure 3.18.

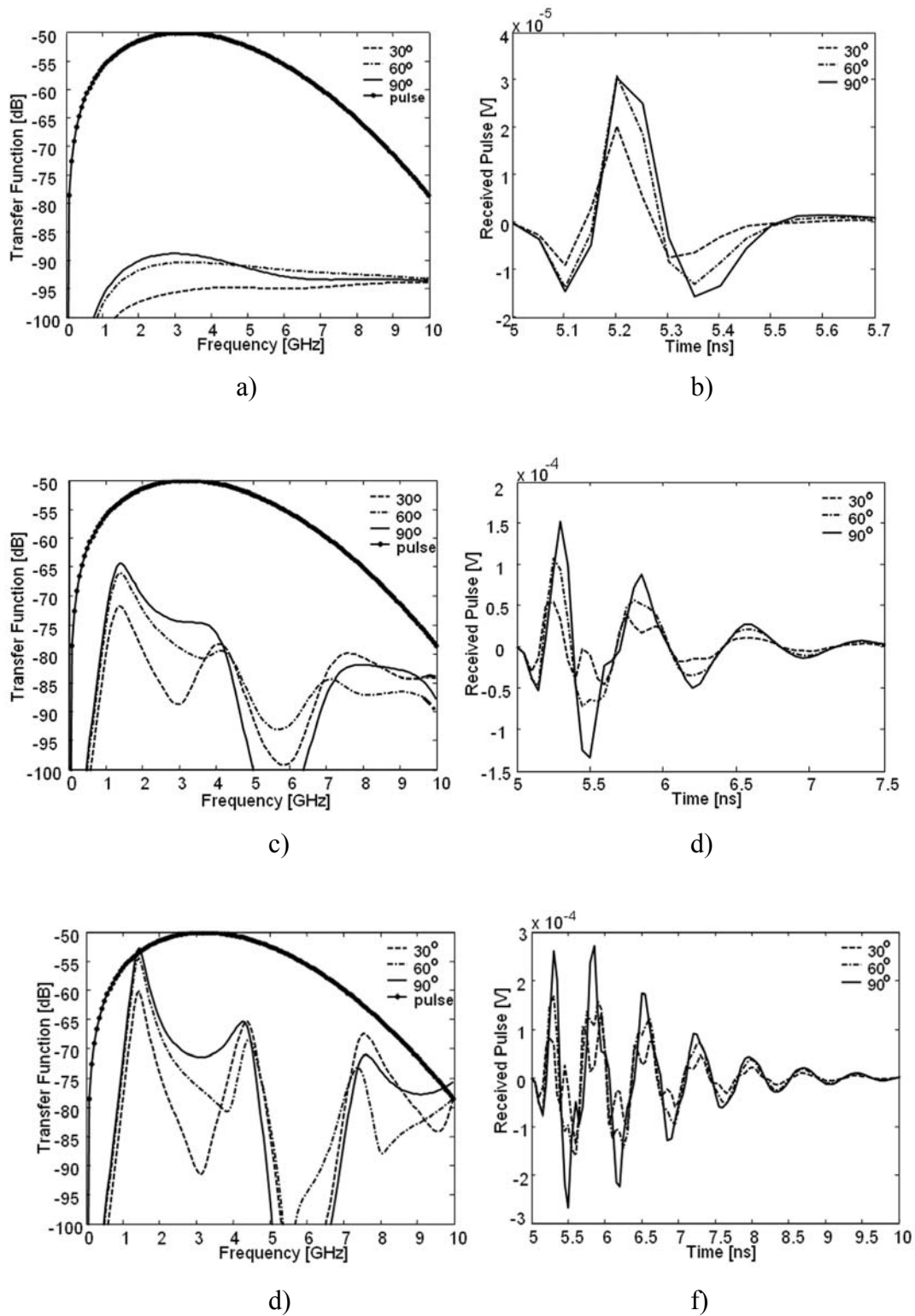


Figure 3.17: Transfer functions $|V_L(f)/V_G(f)|$, and received pulses at the load of the system from Figure 3.12, for 3 different conductivities: 10^2 S/m (a,b), 10^3 S/m (c,d) and 10^7 S/m (e,f). Different relative positions of the receiver antenna, with respect to the transmitter, are presented in each graph: $\theta = 90^\circ$ (continuous line), $\theta = 60^\circ$ (dot-dashed line) and $\theta = 30^\circ$ (dashed line). Dotted line represents the spectrum of the feeding pulse [Miskovsky07a]

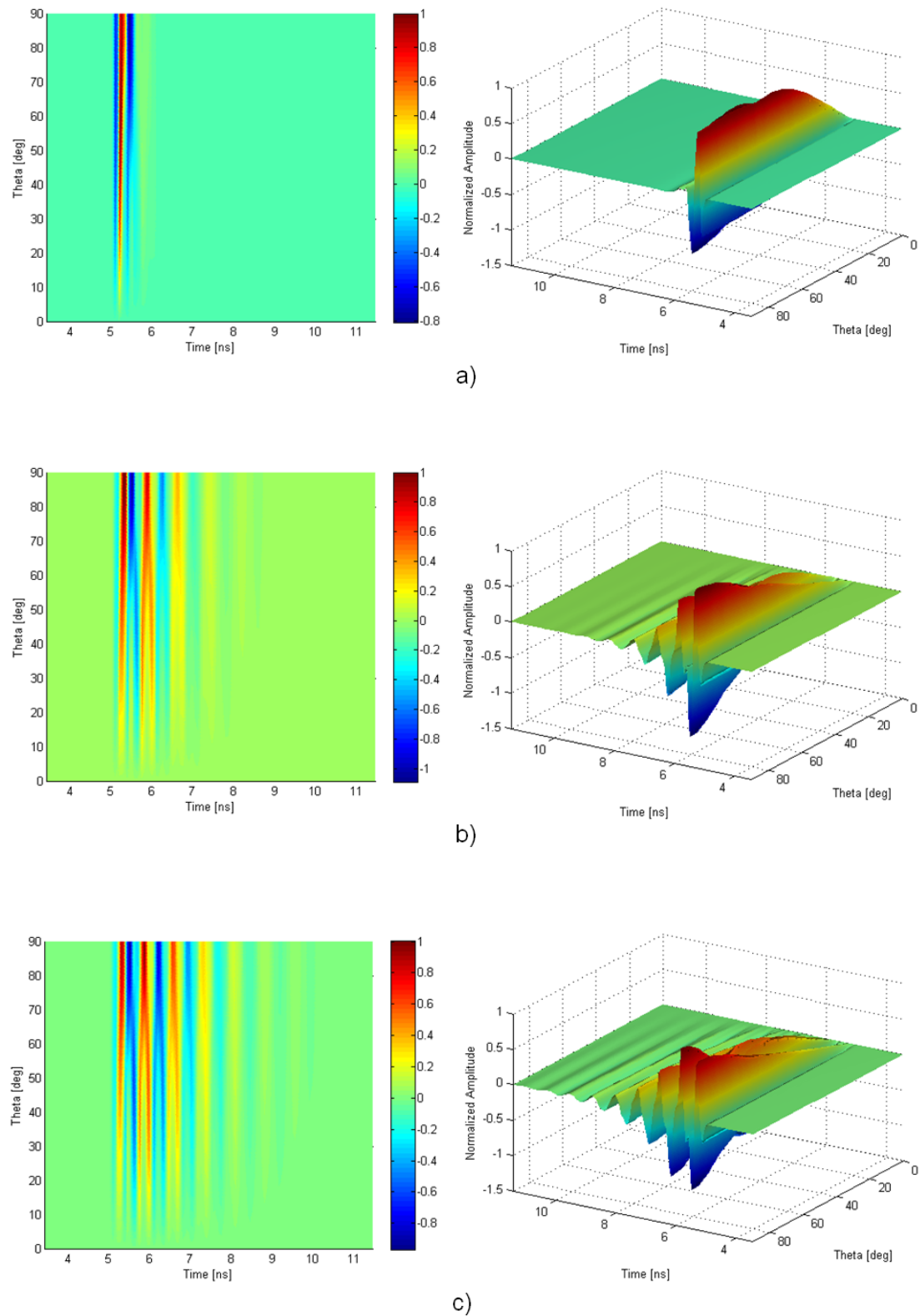


Figure 3.18: Normalized pulse shapes V_L at the receiver load, for 3 different antenna conductivities: a) 10^2 S/m, b) 10^3 S/m, c) 10^7 S/m

3.3. Conclusions

Three figures of merit evaluating the antenna performance within an UWB system have been presented: i) Spatially Averaged Fidelity for a single antenna (SAF_1), ii) Spatially Averaged Fidelity for a transmit-receive system (SAF_2), and iii) Averaged Energy Efficiency (AE). First two parameters, SAF_1 and SAF_2 , summarize the resemblance between received pulses in free space and at the load, respectively, and a given template in all directions of the space.

By using the SAF_1 we have shown that the antenna performance depends on the chosen template and that a good practice should be specifying this template for each particular antenna and application. The SAF_1 parameter summarizes the distortion introduced by the antenna in a single direction-independent number, but depending on the feeding pulse and the template used.

The SAF_2 parameter is more realistic from the point of view of the system than the SAF_1 because it evaluates the fidelity of the pulse delivered to the receiver load and contains the effects of both antennas mismatch and radiation patterns. In the same way as SAF_1 , SAF_2 and AE depend on both the feeding pulse and template shapes. It can be concluded that even an antenna not considered as UWB, such as the conventional $\lambda/2$ dipole, can have high values of fidelity SAF_1 or SAF_2 with a convenient definition of the template.

Our contributions in this chapter can be summarized in two points:

- 1) A direction-independent antenna descriptor SAF_1 , for a single UWB antenna was defined and its application was demonstrated
- 2) A pulse fidelity concept was enlarged to an entire transmit-receive system, defining two new figures of merit: fidelity SAF_2 and averaged efficiency AE
- 3) Using the two figures of merit SAF_2 and AE , we have demonstrated how antenna losses could improve the bandwidth of an UWB system, yielding less distorted pulses delivered to the receiver load.

4. MEASUREMENT METHODS OF UWB DESCRIPTORS

After the definition of UWB antenna performance descriptors in the previous chapter, their application in real antenna design and measurement are demonstrated here. The measurement procedure of both averaged fidelity SAF_I and radiation efficiency η in wide frequency ranges applicable to UWB is described.

The measurement of averaged fidelity SAF_I is much more straightforward than it could seem from its definition. It is basically a measurement of radiated field in an anechoic chamber with a correct calibration and a measurement post processing, paying special attention to the template pulse position in time. The calibration procedure and some aspects of the template positioning are explained as follows.

Up to now, the problem of antenna radiation efficiency measurement in wide frequency ranges was not explicitly treated. In this chapter some of the most known radiation efficiency measurement techniques are shortly recalled and their performance in wide frequency range is shown on some examples. Finally we propose an enhancement of one of these measurement methods to wide frequency range applicable to UWB.

4.1. Measurement of SAF_I

When measuring the SAF_I of an antenna, defined by the expression (3.1), there are basically three steps: (1) measurement of the radiated field \vec{E}_{rad} in all angular directions (θ, ϕ) over a hypothetical sphere surrounding the antenna, (2) definition of the antenna feeding pulse shape P and (3) definition of the template function T and correct shifting to be correlated with the radiated field.

For the sake of simplicity, the measurements were performed in frequency domain, since as explained before there is no real difference in SAF_I formulation in time-domain or frequency-domain. The radiated field \vec{E}_{rad} is a response to a unitary

amplitude signal having a flat spectrum within the frequency band of interest and is actually a transfer function of the antenna measured in an anechoic chamber. In this way a particular pulse shape P fed to the antenna will be radiated as field \vec{E} from expression (3.1), where \vec{E} is the product (convolution in time domain) of the field \vec{E}_{rad} and the feeding pulse P . The radiated field \vec{E} is then multiplied by the template function and integrated through all angular directions (θ, ϕ) .

From the point of view of the measurement post processing implemented in Matlab, it is interesting to use the symmetries of the measured antenna radiation pattern in order to simplify and accelerate the computation of SAF_I . For example in the case of a dipole shown on Figure 3.1, the radiation pattern has a circular symmetry in ϕ , so the radiated field \vec{E}_{rad} needs to be measured only in one section: $\phi=0$ and θ in all angular directions from 0° to 180° . In such a way the numerator of the expression (3.1) has to be integrated in θ and instead of integrating in ϕ , multiplied by 2π .

The influence of the template on the antenna performance in terms of SAF_I was illustrated in the previous chapter (section 3.1.2). In the sections 4.1.1 and 4.1.2, some of the measurement and post processing factors requiring a special attention are considered, such as the measurement calibration and template pulse positioning and sampling.

4.1.1. Wide Frequency Range Anechoic Chamber Calibration

In this section the emphasis is given on several issues concerning the calibration of an anechoic chamber in a wide frequency range. Instead of using a standard gain horn calibration kit, a simpler method using a long coaxial cable, is treated. A standard anechoic chamber configuration for radiation pattern measurements is used in addition to a pair of identical wideband ridge horn antennas and a long coaxial cable covering the distance between the two rotors. A very simplified schematic measurement setup, that will help us to describe the principle of the calibration procedure, is shown on Figure 4.1. Both, antenna under test (AUT) and ridge probe are here supposed to be reflection matched to a feeding coaxial cable impedance and a perfect polarization match between the AUT and the probe is supposed in all measurements.

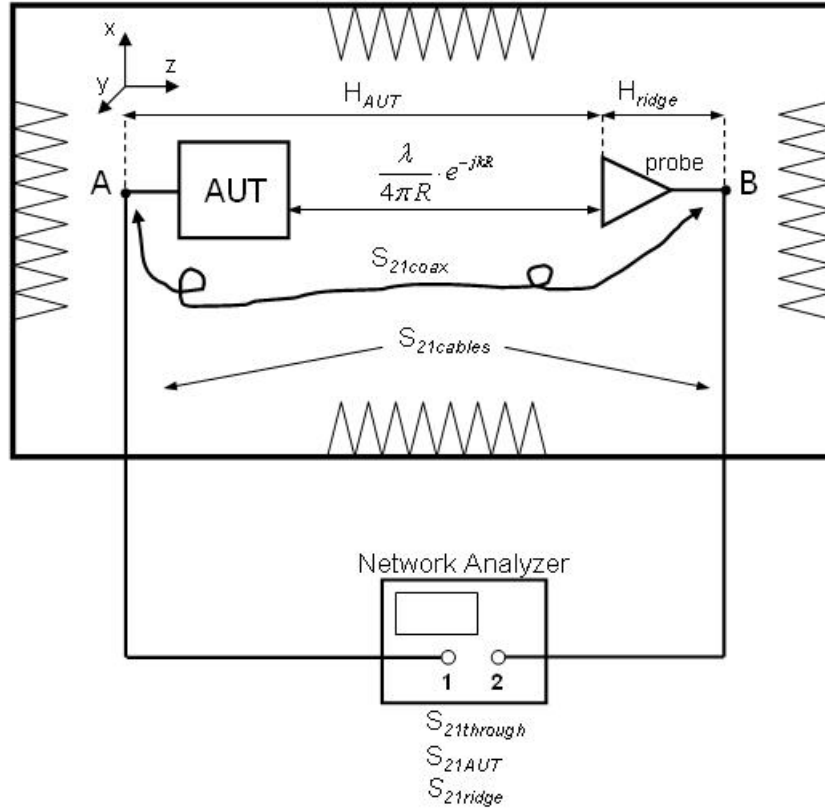


Figure 4.1: Scheme of anechoic chamber measurement setups with antenna under test (AUT), measurement probe at distance R and coaxial cable used as through

The measurement of the radiated field \vec{E}_{rad} can be understood as a measurement of a kind of antenna under test (AUT) transfer function $H_{AUT}(f, \theta, \phi)$, for all angular directions (θ, ϕ) . As shown on Figure 4.1, H_{AUT} is defined by the expression (4.1) as a transfer function between the input connector (A) where a feeding V_{in} is applied and the point at distance R from the AUT, where a co-polar component of the radiated field $E_{rad, cop}$ is received by a probe (ridge horn antenna). It means that the channel influence is included within H_{AUT} .

$$H_{AUT}(f, \theta, \phi) = \frac{E_{rad, cop}(f, \theta, \phi)}{V_{in}(f)} \quad (4.1)$$

The transfer function of the setup that includes the AUT and the ridge horn probe is measured as S_{21AUT} between ports 1 and 2 of the network analyzer of Figure 4.1. The measurement of S_{21AUT} given by the equation (4.2) includes the influence of the

anechoic chamber cables $S_{21cables}$ as well as the influence of the probe denominated H_{ridge} .

$$S_{21AUT}(f, \theta, \phi) = \frac{S_{21cables}(f) \cdot H_{AUT}(f, \theta, \phi)}{H_{ridge}(f, 0, 0)} \quad (4.2)$$

From the expression (4.2) H_{AUT} is obtained in form of equation (4.3), which summarizes the principle of calibration procedure in two steps: 1) measure S_{21AUT} 2) subtract cables $S_{21cables}$ and ridge probe H_{ridge} .

$$H_{AUT}(f, \theta, \phi) = \frac{S_{21AUT}(f, \theta, \phi)}{S_{21cables}(f)} \cdot H_{ridge}(f, 0, 0) \quad (4.3)$$

As S_{21AUT} is known from the measurement, only the quantities $S_{21cables}$ and H_{ridge} need to be identified, for a correct calibration.

In the scheme on Figure 4.1, a long coaxial cable with a previously known, measured transfer function S_{21coax} is connected between the two connector points (A) and (B). In this configuration the transfer function $S_{21through}$ measured between ports 1 and 2 of the network analyzer, involves S_{21coax} and also $S_{21cables}$. As S_{21coax} is known, $S_{21cables}$ can be easily obtained by dividing the measured $S_{21through}$ by S_{21coax} , as given by the expression (4.4).

$$S_{21cables}(f) = \frac{S_{21through}(f)}{S_{21coax}(f)} \quad (4.4)$$

The term $S_{21cables}$ being identified, the remaining term to identify from expression (4.3) that gives the AUT transfer function necessary for SAF_I computation, is H_{ridge} . The physical dimension of H_{AUT} that can be derived from (4.1) is $[m^{-1}]$, where, $E_{rad, cop}$ is in volts per meter $[V/m]$ and V_{in} in volts $[V]$. If the physical dimension of H_{AUT} is $[m^{-1}]$, it means that the physical dimension of H_{ridge} has to be $[m^{-1}]$, as obvious from expression (4.3). This is the first step in identification of H_{ridge} .

In the equation (4.3), H_{ridge} is defined in a similar way as abovementioned AUT transfer function. H_{ridge} is a transfer function of the ridge probe, taken from the input port in (B), (see Figure 4.1) up to the aperture of the ridge horn, but considered only in bore sight direction ($\theta=0^\circ; \phi=0^\circ$). Its physical dimension is $[m^{-1}]$. The Friis

transmission equation of such configuration (using AUT and ridge horn probe) would be defined as (4.5):

$$P_2 = \frac{P_1}{4\pi R^2} \cdot G_{AUT} \cdot A_{eff,ridge} \cdot |S_{21cables}|^2 \quad (4.5)$$

where P_2 is the power delivered to the load on the reception side (port 2 of the analyzer) and P_1 is the power radiated by the AUT (the output power of the port 1, considering that the AUT is perfectly matched), G_{AUT} is the gain of the AUT and $A_{eff,ridge}$ is the effective area of the ridge probe. The transfer function $S_{21cables}$ includes the transfer functions of both cables (not necessarily identical) connecting the network analyzer to points A and B. From Friis equation (4.5) the transfer function S_{21AUT} of such a system measured between ports 1 and 2 of the network analyzer can be described in terms of power as:

$$|S_{21AUT}(f, \theta, \phi)|^2 = \frac{P_2}{P_1} = \frac{1}{4\pi R^2} \cdot G_{AUT}(f, \theta, \phi) \cdot A_{eff,ridge}(f, 0, 0) \cdot |S_{21cables}(f)|^2 \quad (4.6)$$

The same transfer function in terms of voltages was expressed by (4.2), so in terms of power it can be rewritten as (4.7).

$$|S_{21AUT}(f, \theta, \phi)|^2 = \frac{|S_{21cables}(f)|^2 \cdot |H_{AUT}(f, \theta, \phi)|^2}{|H_{ridge}(f, 0, 0)|^2} \quad (4.7)$$

By the identification of different terms from (4.7) in the expression (4.6) it can be shown that the transfer function H_{ridge} is proportional to the square root of the effective area $A_{eff,ridge}$ of the ridge probe, as shown by the expression (4.8).

$$H_{ridge}(f, \theta, \phi) = \sqrt{\frac{1}{A_{eff,ridge}(f, \theta, \phi)}} \quad (4.8)$$

This fact confirms that the physical dimension of H_{ridge} is $[m^{-1}]$, as derived previously from the equations (4.1) and (4.3). Finally $A_{eff,ridge}$ is the effective area of the probe antenna and is defined by the equation (4.9),

$$A_{eff,ridge}(f, \theta, \phi) = G_{ridge}(f, \theta, \phi) \cdot \left(\frac{\lambda^2}{4\pi} \right) \quad (4.9)$$

where G_{ridge} is the gain of the ridge horn probe, containing the exponential term $e^{j\alpha}$ representing the phase shift introduced by the length of the probe. It is important to mention here that in the case of narrowband measurement, the transfer function H_{ridge} used in (4.3) could be defined only in terms of gain $G_{ridge} \cdot e^{j\alpha}$ instead of effective area $A_{eff,ridge}$, because the frequency variation within a narrowband is negligible.

From (4.8) and (4.9) the measurement of H_{ridge} is reduced to the measurement of the ridge horn probe gain. This measurement is realized in the anechoic chamber using two identical ridge horn antennas, in the measurement setup shown on Figure 4.1. A transfer function $S_{21ridge}$ is measured using the network analyzer and the effects of the anechoic chamber cables $S_{21cables}$ and the propagation path between the two antennas $(\lambda/4\pi R)e^{jkR}$ (k being the propagation constant) are subtracted from the measurement as shown by expression (4.10).

$$G_{ridge}(f, \theta, \phi) = \frac{S_{21ridge}(f, \theta, \phi)}{S_{21cables}(f) \cdot \left(\frac{\lambda}{4\pi R} \right) e^{-jkR}} \quad (4.10)$$

An example of such calibration will be shown on real antenna measurements in Chapter 6.

4.1.2. Template Position and Sampling

A fact that any arbitrary pulse can be used as a template, as mentioned in the previous chapter, raises a couple of issues to be taken into account in the measurements. In this section, for the sake of simplicity, numerical simulations are shown instead of measurements, knowing that the issues of template positioning and sampling are the same in the case of measurement and simulation.

First of all, in the expression (3.1) we are talking about correlation between the radiated field \vec{E} and the template T but the numerator of (3.1) has obviously not the same formulation as the definition of the cross-correlation. Actually in the expression (3.1) it is supposed that the template T is already shifted to the time instant τ where

the radiated pulse \vec{E} is found. The initial situation is illustrated on Figure 4.2, where the normalized Sinc template and the normalized field \vec{E} radiated by a 30 mm long wire monopole oriented along z-axis at $\theta=90^\circ$ and $\phi=0^\circ$, are represented. Once the template shape is fixed and the radiated field \vec{E} in all angular directions of interest is measured, the template needs to be shifted to a particular time instant τ . In other words, the SAF_I value depends on time instant τ , where the correlation in the numerator is carried out.

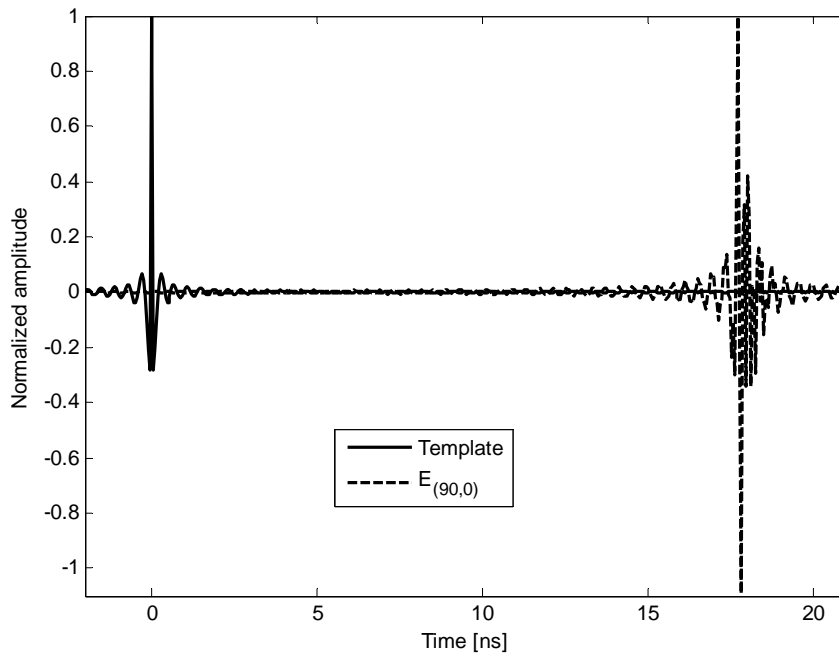


Figure 4.2: Arbitrary template defined at origin (continuous line) and simulated radiated electromagnetic field E (dashed line) at $\theta=90^\circ$, $\phi=0^\circ$ at distance $R=5.31$ m, radiated by a 30 mm long wire monopole

The template T (a sinc pulse having a flat spectrum within the operational frequency range 2.5 GHz – 10.5 GHz) is centered in $t=0$ ns and the radiated field was simulated at distance 5.31 m from the source which corresponds to $t=17.7$ ns. In order to compare the shape of the template T with the shape of the radiated field \vec{E} , the template T has to be shifted to where \vec{E} is found, ideally to $t=17.7$ ns. From the Figure 4.2 it is obvious that the radiated pulse \vec{E} suffers some distortion (ringing, spreading etc.) so the question that comes out is whether the template has to be shifted to exactly 5.31 m (*i.e.* if $t=17.7$ ns is the best option to match the template to the radiated \vec{E} field pulse). Instead of time positioning of the respective pulses, the

corresponding distance R (the distance that the electromagnetic field travels in time t) can be used, when working in the frequency domain.

In addition to the initial criterion (shifting the template to the distance where the field was simulated/measured, $R=5.31$ m) two more criterions can be considered.

- *maximum \vec{E} field peak criterion:* $R_{\max,\text{peak}}$ is determined as the distance to the maximum peak of the overall field matrix \vec{E} or $\vec{E}_{(\theta,\phi)}$ in a particular direction (θ, ϕ)
- *maximum correlation criterion:* the distance $R_{\max,\text{corr.}}$ is defined as the distance that maximizes the correlation in the numerator of the SAF_I in (3.1) which is the approach initially proposed by Lamensdorf in [Lamensdorf94]. The maximum peak criterion was used in the previous chapter in Table 3.1 where the Sinc template and its derivatives were analyzed.

The influence of the abovementioned template positioning criterions on SAF_I value is shown in Table 4.1. For each of the three criterions and two different sampling rates, the distance R (template shift) and the corresponding SAF_I values are shown.

Table 4.1: The fidelity SAF_I dependence on sampling and positioning criterion for 30mm long wire monopole of 0.8mm radius

Sampling step	Initial	Maximum \vec{E} peak	Maximum correlation
$\Delta t=47.6$ ps	$R = 5.31$ m	$R_{\max,\text{peak}} = 5.31$ m	$R_{\max,\text{cor.}} = 5.31$ m
	$SAF_I = 0.51$	$SAF_I = 0.51$	$SAF_I = 0.51$
$\Delta t/16=2.97$ ps	$R = 5.31$ m	$R_{\max,\text{peak}} = 5.3287$ m	$R_{\max,\text{cor.}} = 5.3091$ m
	$SAF_I = 0.51$	$SAF_I = 0.28$	$SAF_I = 0.52$

The influence of the sampling rate on average fidelity SAF_I performance will be explained in detail further in this section. Nevertheless, let us first look at the second row of the Table 4.1 with higher sampling rates ($\Delta t/16$), where the differences between SAF_I values dependence on positioning criterion are more obvious. Of course, the criterion maximizing the correlation between the template and the radiated field gives the highest value of SAF_I which is 0.52. This value is obtained as indicated in the Table (4.1), if the template pulse is shifted to, exactly, $R=5.3091$ m. Using the

criterion of maximum \vec{E} field peak, the template has to be shifted to $R=5.3287$ m and the averaged fidelity SAF_I in this position is much smaller, $SAF_I=0.28$. Further in this section it will be shown why this difference of only 1.96 cm in the template positioning represents a difference of almost 0.3 in SAF_I value. The difference in SAF_I value between the initial criterion and maximum correlation criterion is only of 0.01 because the distance R maximizing the correlation is very close to the distance $R=5.31$ m where the field was initially measured.

In order to emphasize some of the template positioning issues, templates shifted to $R_{\text{max.peak}}=5.3287$ m ($t=17.76$ ns) and $R_{\text{max.cor}}=5.3091$ m ($t=17.69$ ns), corresponding to maximum \vec{E} peak and maximum correlation criterions respectively, are shown on Figure 4.3. On the same figure, the \vec{E} field pulse radiated by a 30 mm long, 0.8 mm radius wire monopole oriented along z-axis is shown, at angular direction $\theta=56^\circ$ and $\phi=0^\circ$ which corresponds to the direction where the overall \vec{E} maximum peak is found. For comparison purposes the same pulse is shown in both cases a) and b). In both cases the template peak matches one of the \vec{E} field peaks and so the comparison of the template with the \vec{E} field pulse is not obvious. In other words, from the curves shown on Figure 4.3 it can not be concluded whether a) or b) will give better SAF_I , because it shows only one angular direction.

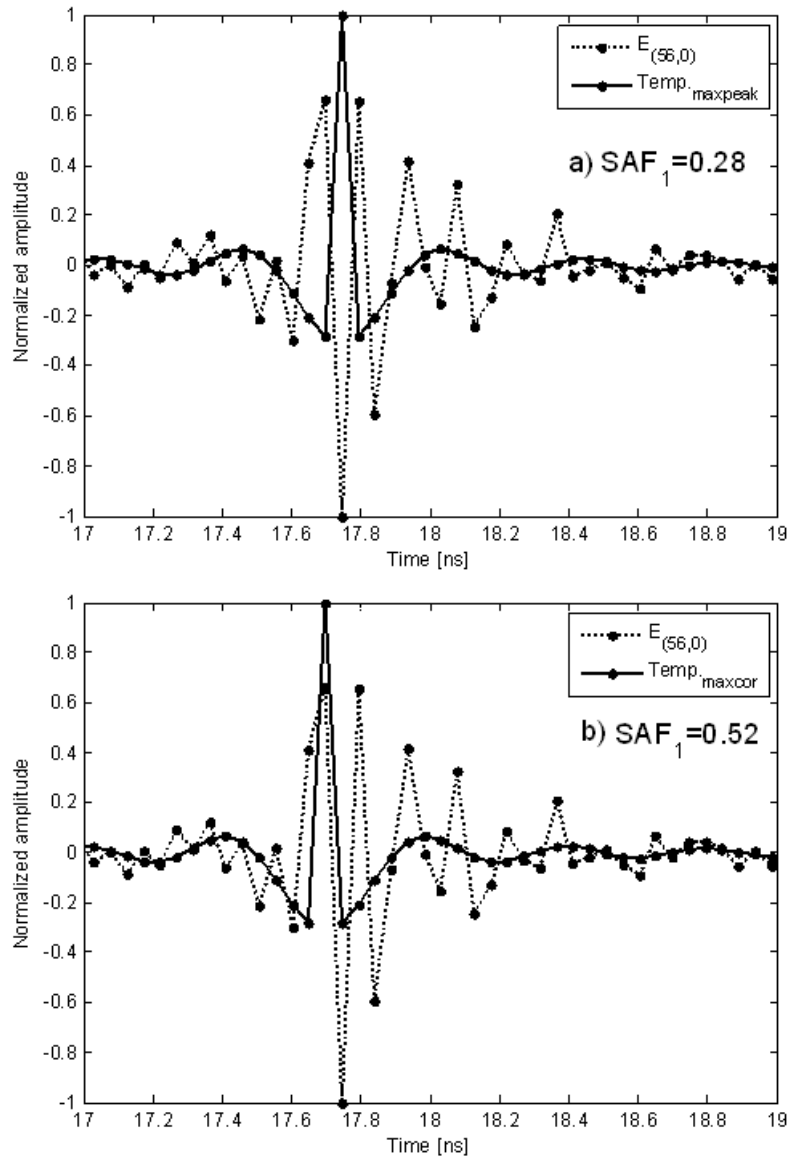


Figure 4.3: Comparison of criteria for template positioning in the case of a 30mm long monopole with wire radius 0.8 mm: a) radiated field $\vec{E}_{(56,0)}$ at $\theta=56^\circ$ and $\phi=0^\circ$ (dashed line), template (continuous line) shifted to the distance $R=5.3287m$, determined using maximum \vec{E} peak criterion, b) template shifted to the distance $R=5.3091m$ using maximum correlation criterion.

The difference of 1.69 cm between the two templates positions in a) and b) corresponds to 0.07 ns, which is a difference of only one sample. This single sample difference can make a difference of 0.24 in averaged fidelity SAF_I value, which is quite important. The correct template positioning and positioning criterion are important issues because, as shown here, a small positioning error can introduce an important variation of averaged fidelity SAF_I .

Another issue concerning an arbitrary template shape definition should be mentioned at this point. The field \vec{E} radiated by the AUT in an arbitrary reference direction (θ, ϕ) , can be taken as template for SAF_I computation. In this case the template positioning is not the issue because the template is already correctly positioned. This is the case of SAF_I shown on Figure 3.5 and Figure 3.9 in the previous chapter. Dissanayake used the same approach for a template definition in [Dissanayake06], where a parameter similar to SAF_I was used to characterize radiation pattern stability in a wide frequency range.

The influence of sampling rate on SAF_I value is also shown in Table 4.1. The need of signal oversampling can be explained qualitatively. Signals with large frequency content such as UWB pulses can be very rapidly changing signals with narrow peaks as it is the case of any radiated \vec{E} pulse shown previously. It means that a correlation function of two such signals will also have important variations and narrow peaks. In this case (looking for a maximum correlation between template and radiated pulse) a finer sampling would be necessary to depict all the cross-correlation peaks and so find the maximum with higher accuracy.

If the pulse is sampled at a rate following the Nyquist-Shannon sampling theorem [Shannon49], the minimum sampling frequency f_s for correct signal reconstruction at reception has to be the double of the maximum frequency f_{max} contained in the sampled signal, ($f_s=2 \cdot f_{max}$). The sampling interval corresponding to f_s is defined as Δt . If the template and radiated \vec{E} -field pulses are oversampled, for example 16 times ($\Delta t/16$), using zero padding, it allows two things:

- the template can be positioned with more precision (space shifting step is now $dR/16$)
- the maximum \vec{E} field peak or the maximum of cross-correlation can be found with more precision

As can be also seen from Table (4.1), the oversampling means higher resolution in template positioning and gives different values of R depending on the positioning criterion and so different SAF_I values. The influence of the sampling rate on SAF_I value in the case of maximum correlation criterion is illustrated in Figure 4.4. Finer

sampling at $\Delta t/16$ allows depicting all the variations of SAF_I through distance R of the template shift and so finding the maximum position with more accuracy. The difference of 0.01 in fidelity value shown in Table 4.1 is confirmed by SAF_I values shown in Figure 4.4.

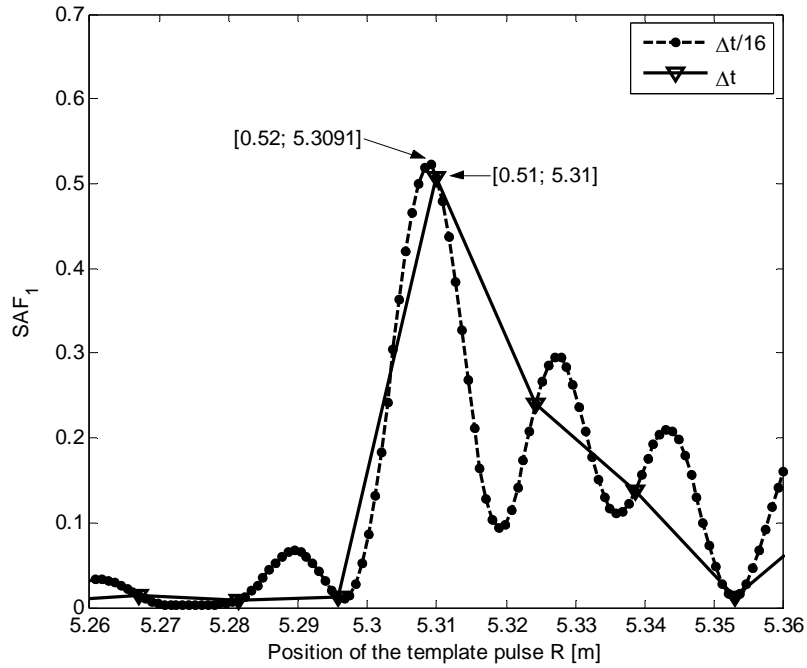


Figure 4.4: Influence of sampling rate on SAF_I value. Each sample is marked with a dashed line with dots (in the case of $\Delta t/16$) or continuous line with triangles (in the case of Δt)

In summary, the fact that the measurement of the spatially averaged fidelity SAF_I faces several issues originated from its definition, should be underlined. SAF_I depends on the template shape and on the particular time instant of correlation that appears in SAF_I numerator. The sampling rate influence on SAF_I value is related to these two issues. The template shape itself can be arbitrarily selected, but in order to attain the best SAF_I performance it should be selected considering also the shape of the pulse fed to the AUT. Finally, the comparison of antennas in terms of SAF_I performances should always be realized in the same conditions of feeding, template pulse shapes and sampling rate. Concerning the template positioning, the maximum correlation criterion is the best option because when comparing with the other two criteria, it gives the maximum SAF_I value and rapidly converges if the sampling rate is increased.

4.2. Measurement of Radiation Efficiency in UWB

An improvement of the Johnston-Geissler (J-G) method for the measurement of UWB antennas is proposed in this section. The J-G method was originally applied to narrowband antennas and is exhaustively described in [Johnston98] and [Geissler03].

First the potential of J-G method for wideband measurement is assessed by comparison with some of the above stated measurement methods. Then the method is validated through simulations and finally an application to UWB antenna radiation efficiency measurement is shown. To our knowledge only one author [Schantz01] has explicitly treated the problem of UWB antenna radiation efficiency measurement up to now. The results presented in this section were published in [Miskovsky09].

4.2.1. Application of Johnston-Geissler method to UWB

As mentioned in [Johnston98], J-G method could be extended to a wider frequency range. In this case the reflection coefficient of the antenna within the cap $S_{11, cap}$ should be measured at several frequencies around the frequency of interest. Then a circumference should be fitted through the resulting data points and the values of $\Delta_{S, max}$ and $\Delta_{S, min}$ determined according to Johnston's formulation. J-G radiation efficiency is then computed from expression (4.11), defined by Johnston [Johnston98].

$$\eta = \frac{2}{(\Delta_{S, max})^{-1} + (\Delta_{S, min})^{-1}} \cdot \frac{1}{1 - |S_{11, fs}|^2} \quad (4.11)$$

For the measurement in an ultra wide frequency range, the same procedure is applied with the only difference that all of the measured $S_{11, cap}$ data points are used to obtain the radius and center of the circumference according to the minimum mean square error (MSE). A routine to fit a circle to the measured data has to be implemented. For each frequency f_N a subset $S_{11N, cap}$ of the original $S_{11, cap}$ data points corresponding to a half-circumference in the Smith chart is selected using expression (4.12), where φ is the unwrapped phase at a given frequency.

$$\varphi(S_{11, \text{cap}}) \in \left[\varphi(S_{11N, \text{cap}}) + \frac{\pi}{2}; \varphi(S_{11N, \text{cap}}) - \frac{\pi}{2} \right] \quad (4.12)$$

In our case all S_{11} data are measured in frequency range from 2.5 GHz to 10.5 GHz with 1601 frequency samples.

The procedure is shown on Figure 4.5 for the particular frequency of 6.92 GHz where the subset of the selected $S_{11, \text{cap}}$ data points (red dots) corresponds to the frequency interval from 5.85 GHz to 7.12 GHz. In our case, only 187 out of the 1601 frequency data points are used to plot the required half-circumference. On the same figure, a complete circumference (blue line) is fitted to the measured data by means of the MSE. The required values of $\Delta_{S, \text{max}}$ and $\Delta_{S, \text{min}}$ are determined as shown on Figure 4.5.

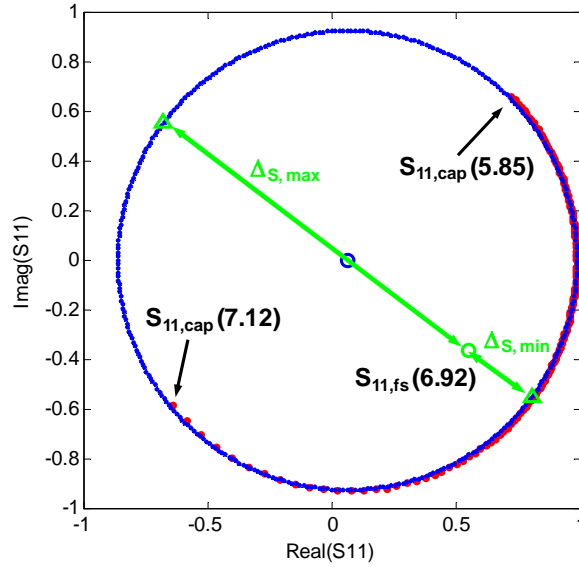


Figure 4.5: Measured $S_{11, \text{cap}}$ (red dots) and fitted (blue line) circumference, for the measurement at 6.92 GHz [Miskovsky09]

Instead of a half-circumference, a complete circumference can be used to determine the radius and the center of the fitted circumference. However, we have empirically verified that the error of the computed radiation efficiency is greater when using a complete circumference. More details concerning the use and properties of circumference fitting in J-G measurement method are shown in the Annex A3.

4.2.2. J-G Method Assessment on a Lossy Monopole

In order to assess the validity of the J-G method, we need to measure the efficiency performance of an antenna which radiation efficiency is known a priori. For this purpose we used a lossy antenna with known losses, as a reference. The lossy antenna was obtained by cascading a standard attenuator with an 800 MHz resonant $\lambda/4$ straight wire monopole. The copper wire monopole is supposed to have, at least theoretically, 100% radiation efficiency. The attenuators of 3 dB and 6 dB, used in the following measurements, cascaded with the wire monopole should allow reaching radiation efficiencies close to 50% and 25% respectively. The antenna cascaded with an attenuator is called here a virtual lossy antenna and is schematically shown on Figure 4.6.

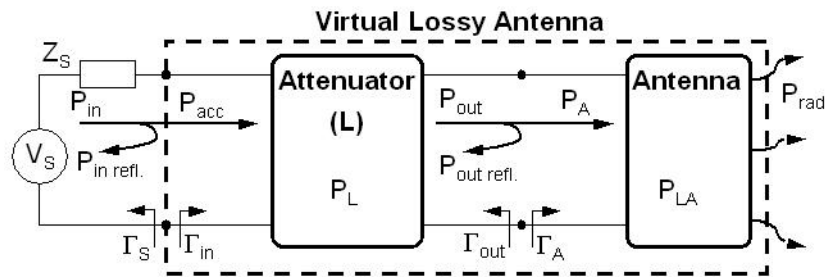


Figure 4.6: Circuit model of the lossy antenna [Miskovsky09]

Firstly, a measurement using J-G method in the frequency range from 100 MHz to 11 GHz was performed on three antennas: the 800 MHz monopole alone (on Figure 4.7 referenced as $L=0$ dB), and the same monopole cascaded with 3 dB and 6 dB attenuators. These measurements are represented by continuous lines on Figure 4.7. The majority of cap resonant modes above 7.67 GHz do not appear because of the circumference fitting algorithm.

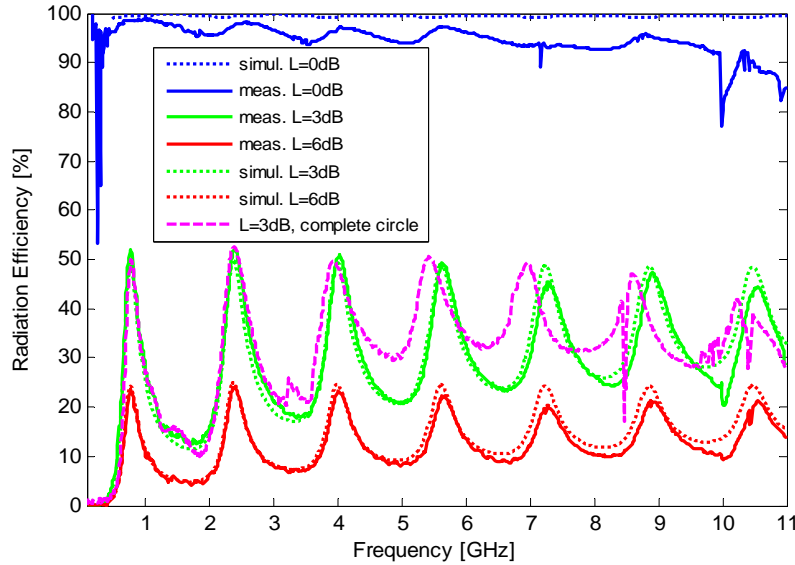


Figure 4.7: Measurements and simulations of the 800 MHz monopole alone ($L=0$ dB) and cascaded with the 3 dB and 6 dB attenuators [Miskovsky09]

Secondly, the radiation efficiency of a copper wire monopole cascaded with 3dB and 6dB attenuators was simulated using NEC [Burke81]. The corresponding attenuator of attenuation L was modeled using a resistive T-network as explained in [Poza98] and shown in Annex A2.

The difference between the measurement and simulation in the case of antenna without attenuator (blue curves in Figure 4.7) is due to the losses of the cap and the ground plane that predominate over the antenna losses. However, the measured radiation efficiency values still remain within the error range of methods based on Wheeler cap principle [Poza88].

In the case of antennas cascaded with attenuators (green and red curves on Figure 4.7), the agreement between measurements (continuous lines) and simulations (dotted lines) is better because the losses of the cap and ground plane are negligible compared to the losses due to the attenuators. The radiation efficiency peaks are due to the frequency variation of the radiation resistance over the operational frequency band.

For the case of the antenna with the attenuator of 3dB, a measurement using a half $S_{11,cap}$ circumference (green continuous line) and complete circumference (magenta dashed line) are compared on Figure 4.7. The frequency shift at high frequencies is evident and the measurement using a half $S_{11,cap}$ circumference is in better agreement with the simulation.

The very good agreement between the measurement and the simulation, shown on Figure 4.7, assesses the potential of the method to get radiation efficiencies in an ultra-wide frequency band. Therefore, in the following section this method will be used to measure the radiation efficiency of UWB antennas.

In addition, Figure 4.8 compares the resulting measured efficiencies using J-G, Wheeler cap and McKinzie methods, for the 800 MHz monopole cascaded with the 3dB attenuator. The McKinzie method that gave reasonably stable efficiency values for the wire monopole (see preliminary results in Chapter 2) shows several efficiency steep nulls, as well as the Wheeler method. Moreover, the radiation efficiency figures obtained from these two methods are far from the figures given by the J-G method.

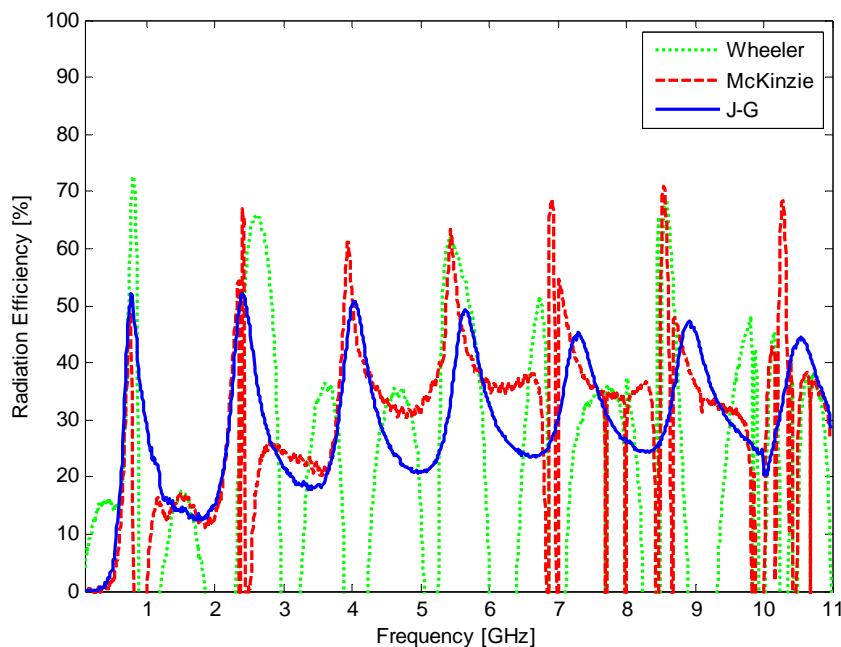


Figure 4.8: Comparison of Wheeler, McKinzie and J-G radiation efficiency measurement methods for the 800 MHz monopole cascaded with a 3 dB attenuator [Miskovsky09]

4.2.3. Application of J-G method to UWB antennas

The J-G method extended to UWB frequency range was applied to determine the radiation efficiency of a conical monopole (similar to a volcano smoke antenna [Paulsen03]) and a trapezoidal monopole [Evans99], shown on Figure 4.9. Both monopoles are matched to 50Ω as shown on Figure 4.10 (return losses are always better than 10 dB) at all frequencies above 2.7 GHz and 4.4 GHz, respectively.

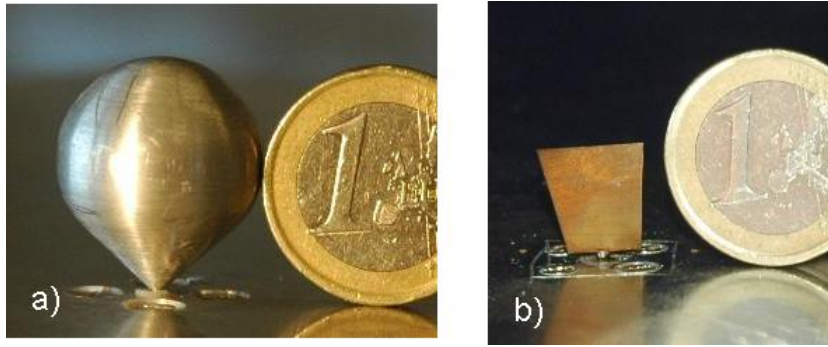


Figure 4.9: Size comparison of UWB antennas with one euro coin: (a) conical monopole, (b) trapezoidal monopole

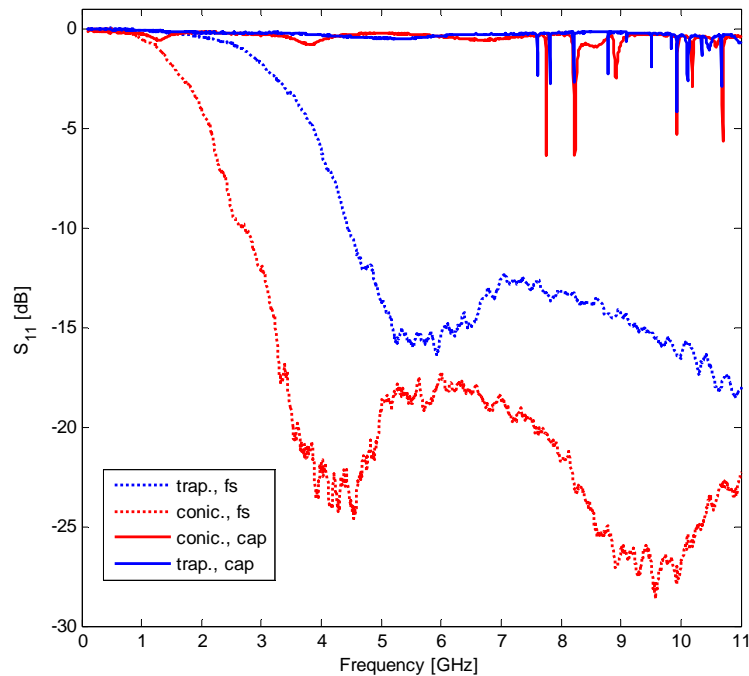


Figure 4.10: Conical and trapezoidal monopoles input port reflection coefficient measured in free space (dashed curves) and within the aluminum cap (continuous curves).

The aluminum tube ($L=120$ mm, $d=23$ mm) shown on Figure 2.3 was used as a Wheeler cap. Its resonant modes are shown on Figure 4.10 (solid lines). The measurement results over the frequency range from 100 MHz to 11 GHz are shown on Figure 4.11. Both monopoles achieve radiation efficiencies around 95% across the whole frequency band. Due to the circumference fitting algorithm only few efficiency notches appear at higher frequencies. As shown on Figure 4.11 the measurements at low frequencies (left yellow band) are not accurate because they are below the lowest Wheeler cap working frequency ($ka=1$). The first resonant mode at 7.67 GHz limits

the useful frequency range of the cap. Above this frequency (right yellow band) the measurement is not accurate because of the efficiency notches that were not removed by the fitting algorithm. A cap having the first resonant mode above 10.5 GHz should be used for a correct efficiency measurement in the UWB frequency range. Unfortunately the dimensions of the antenna were the limiting factor that did not allow its use.

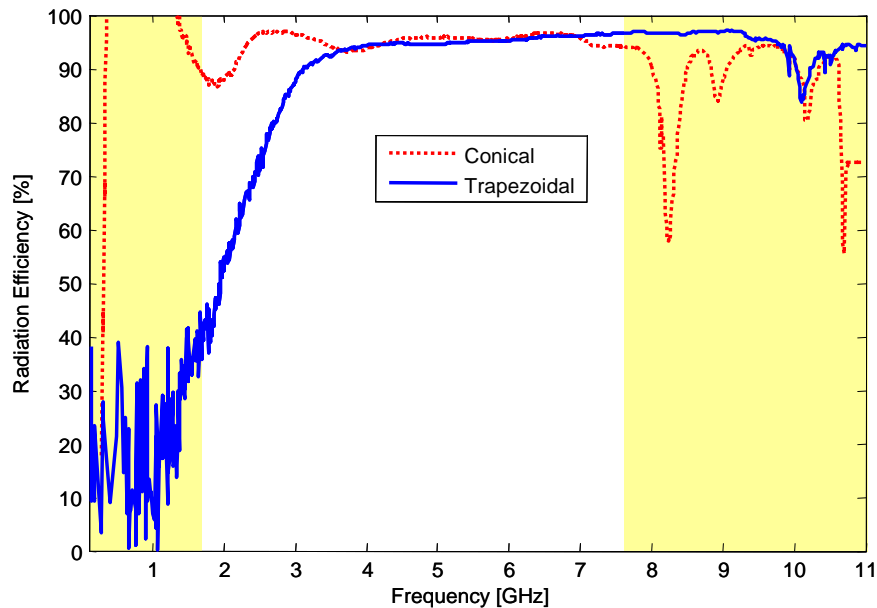


Figure 4.11: J-G efficiency measurement of the two UWB antennas: conical and trapezoidal monopoles. The limited accuracy zones are also shown with yellow bands [Miskovsky09]

Finally our improvement in radiation efficiency measurement achieved by the enhanced J-G method can be underlined by the measurement of the same two UWB antennas by conventional methods. The radiation efficiency measurements of the conical and trapezoidal monopoles using the traditional Wheeler cap method and McKinzie method are shown on Figure 4.12 and Figure 4.13. As expected, in both cases for both antennas, several steep nulls and efficiency notches appear over the whole measurement bandwidth. An exception is the measurement of the trapezoidal monopole using McKinzie method shown on Figure 4.13, which gives similar efficiency values as the J-G measurement on Figure 4.11, up to the first resonant mode of the cavity at 7.67 GHz. In this case a serial circuit loss model was forced by McKinzie measurement post-processing algorithm and so the loss mechanism of the trapezoidal monopole can probably be modeled very well by a series RLC circuit. If the loss mechanism would be more complicated, and so couldn't be modeled by either

a series or a parallel RLC circuit (such as in the case of non-resonant UWB antennas), the McKinzie method would not give such a satisfactory result. From Figure 4.13 it seems that this would be the explanation of the behavior of the conical monopole.

Definitely the J-G method gives more stable efficiency values due to fact that it is not dependent on antenna loss mechanism circuit model and that the circumference fitting manages to filter some of the efficiency notches appearing in other measurement methods.

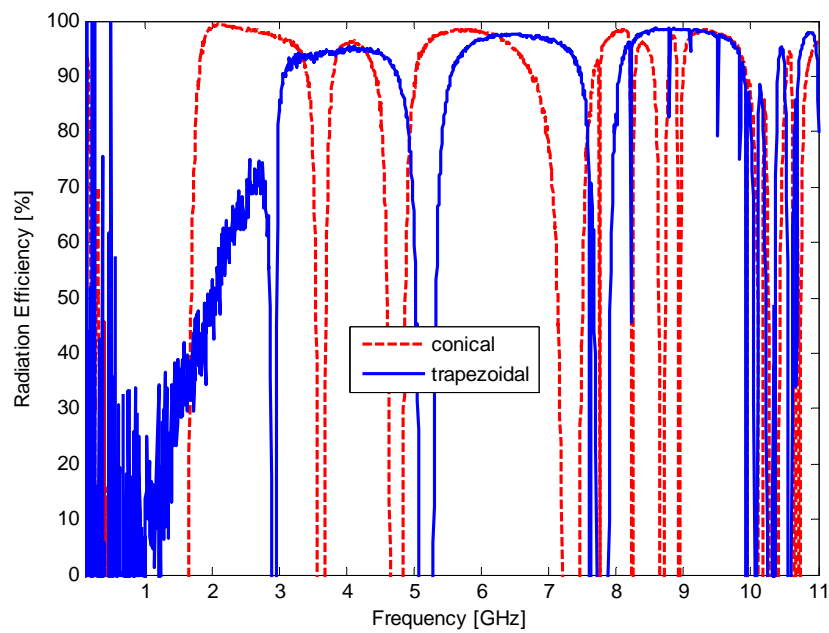


Figure 4.12: Conical and trapezoidal monopoles radiation efficiencies measured by Wheeler cap method

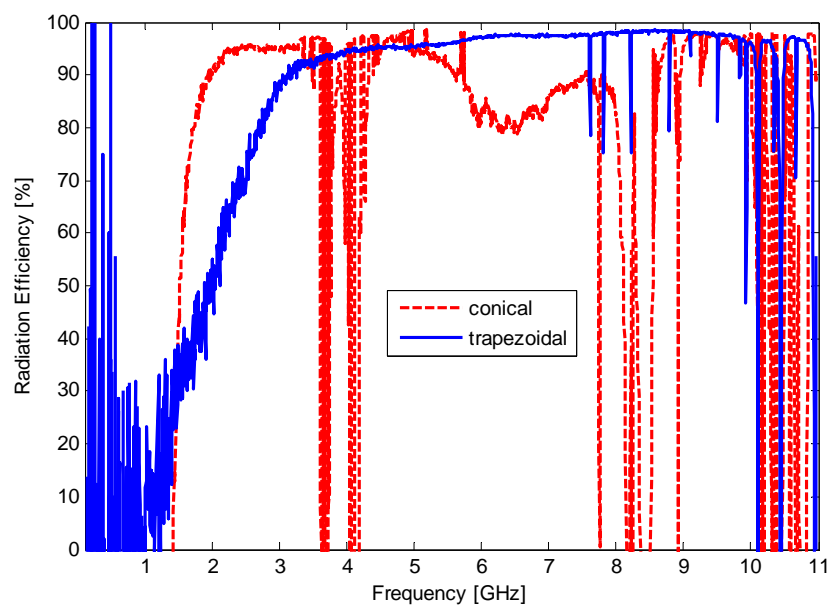


Figure 4.13: Conical and trapezoidal monopoles radiation efficiencies measured by McKinzie method

4.3. Conclusions

Two measurement procedures of two UWB antenna performance descriptors were outlined in this chapter: Spatially Averaged Fidelity (SAF_I) measurement and radiation efficiency measurement in an Ultra-Wide frequency range.

First of all a simplified calibration of the anechoic chamber based on a long previously characterized cable used as a through was shown. This calibration method is much cheaper and simpler than calibration using a standard gain horns calibration set, and is enough accurate for the measurement purposes shown here.

It was shown that the measurement of antenna figure of merit SAF_I is basically a measurement of the radiated field \vec{E}_{rad} which is the response to the unitary amplitude signal having a flat spectrum within the frequency band of interest. The field \vec{E}_{rad} is measured in all angular directions of interest (θ, ϕ) and can be considered as a transfer function of the antenna under test. Then a feeding pulse and a template are chosen and the SAF_I computation implemented. The SAF_I figure of merit depends on the particular feeding pulse shape and the template pulse shape. As a consequence, antennas comparison based on SAF_I should always be carried out in the same conditions including feeding and template pulses. A special care has to be taken on sampling rates but also template positioning, maximizing the overall cross-correlation between radiated pulses and template and so maximizing the SAF_I value.

Moreover the potential of the enhanced Johnston-Geissler method for radiation efficiency measurement in an ultra-wide frequency range was shown through simulations and measurements, on a lossy monopole (emulated by a wire monopole with a cascaded attenuator). The method seems to be useful for its application to UWB antenna radiation efficiency measurements as shown on two common UWB antennas (conical and trapezoidal monopoles). It was used for example in [Perruisseau09] and [Gemio09]. The most attractive features of J-G method are its independence from the antenna circuit model and the simplicity of implementation, inherited from the original Wheeler cap method. In addition the J-G model eliminates the efficiency steep nulls and reduces the number of notches.

The major contributions of the author concern the definition and the measurement procedure of a figure of merit called spatially averaged fidelity SAF , and the enhancement and experimental assessment of radiation efficiency measurement method to UWB frequency range.

Our contributions in this chapter can be summarized as follows:

- 1) Definition of fidelity SAF_I measurement procedure and basic guidelines
- 2) An enhancement of the measurement method proposed by Johnston and improved by Geissler for wide frequency ranges
- 3) Explanation of radiation efficiency notch filtering mechanism (shown in Annex A3) through the circumference fitting algorithm.

The following guidelines summarize the most important measurement steps and give a practical insight to antenna performance descriptors treated in this chapter.

Spatially Averaged Fidelity SAF_I :

The measurement of SAF_I can be resumed in 5 steps:

- 1) Four measurements, as shown in Figure 4.1, in the whole frequency band of interest:
 - a) S_{21coax} , measured using a network analyzer
 - b) $S_{21through}$ with a coaxial cable connected between two points A and B
 - c) $S_{21ridge}$ with two identical ridge probes connected to points A and B
 - d) S_{21AUT} with AUT and ridge probe
- 2) A calibration of the anechoic chamber (cables and probe), finding the probe transfer function H_{ridge} from expressions (4.8), (4.9), (4.10) and transfer function of anechoic chamber cables $S_{21cables}$ from (4.4).
- 3) AUT transfer function H_{AUT} is obtained from (4.3).
- 4) A definition of antenna feeding pulse shape P and template pulse shape T , in time or frequency domain.
- 5) Calculation of SAF_I from expression (2.5) where \vec{E} is a convolution of H_{AUT} with the feeding pulse P

J-G radiation efficiency in wide frequency range:

The measurement of J-G radiation efficiency in a wide frequency range is summarized in four steps:

- 1) Wheeler cap selection: a general rule for cap selection is that the frequency band of interest should fit between the lowest working frequency of the cap ($ka=1$) and the frequency of its first resonant mode. As shown above, several resonant modes are filtered by the circumference fitting algorithm so the useful range of the cap can be enlarged. The useful range enlargement depends on each particular case as shown in Figure 4.11, where the trapezoidal monopole can be measured up to 9.5 GHz whereas the conical monopole (probably for its size and proximity to cap's wall) can only be measured up to the frequency of the first resonant mode of the cap.
- 2) Measurement of antenna in free space $S_{11,fs}$ and antenna within the cap $S_{11,cap}$.
- 3) Calculation of $\Delta_{S,max}$ and $\Delta_{S,min}$ using a circumference fitted to half-circumference $S_{11,cap}$ data.
- 4) Radiation efficiency calculation from expression (4.12)

5. DESIGN AND OPTIMIZATION OF AN UWB LOADED MONOPOLE

As proposed by the third aim of the thesis, a practical use of UWB antenna descriptors through an optimization of a loaded UWB antenna is demonstrated here.

As mentioned by Montoya [Montoya96], for UWB pulse radiation, transmitting antennas should ideally have low reflected voltage at the feeding port, they should radiate a waveform of a shape similar to the exciting pulse (transmission without pulse distortion) or its derivative (transmission with known pulse distortion), but they also should have high radiation efficiency. Various antenna impedance loading schemes that potentially could attain these characteristics, have been proposed by different authors: Wu [Wu65], Rao [Rao69], Kanda [Kanda78] [Kanda83], and Esselle [Esselle90]. Some of these designs intend to extend the bandwidth of the antenna [Wu65], preserve the radiated pulse shape [Kanda78] or improve the farfield pattern over a range of frequencies [Rao69], what makes them potentially interesting in the context of antenna design for UWB systems. Inspired by the monopole designs proposed by Wu, Rao or Kanda, our purpose is to design a loaded monopole for UWB systems, using antenna descriptors defined in chapters 3 and 4.

Any antenna performance descriptor defined by a single number, such as fidelity SAF_I can result very practical for antenna optimization using CAD tools, as well as for a measurement comparison of different antennas. Despite of the inconvenience of being a custom descriptor (for comparison of two different antennas, SAF_I has to be computed in exactly the same definitions of feeding and template pulse shapes, frequency band, angular directions, etc.), it is shown in this chapter how such descriptor can be used in the optimization of UWB antennas. For this purpose, a particular attention will be given to resistively and capacitively loaded antennas able to reach wide bandwidths and whose performance in terms of radiated pulse fidelity can easily be varied by modification of impedance values. Consequently, our aim is to design an impedance loaded UWB antenna with optimum performance in terms of

spatially averaged pulse fidelity SAF_I , but also in terms of radiation efficiency and so to demonstrate the applicability and usefulness of the figure of merit SAF_I .

Like in many multi-dimensional multi-objective problems, there is not always a single best solution but a set of solutions, known as Pareto front [Reyes06], representing all possible trade-offs that can be made for given problem and criteria. Once the front is identified, the designer can choose the best solution for the current application. The Pareto front of a set of possible resistive loading profiles carried out on a monopole antenna is determined using a Particle Swarm Optimization (PSO) technique. This Pareto front is the result of an optimization in terms of spatially averaged fidelity SAF_I and mean value of radiation efficiency for a given bandwidth.

To overcome the main limitation of resistively loaded antennas (low radiation efficiency mainly due to ohmic losses in loading resistors) a capacitive loading can be used. A capacitively loaded antenna is also optimized using PSO in terms of averaged pulse fidelity SAF_I and reflected energy at the feeding point of the antenna.

5.1. Impedance Loading Profile Definition

5.1.1. Geometry Definition

First, the geometry of the loaded monopole optimization problem is defined. A monopole of length h and radius r , oriented along z -axis can be divided into a number of discrete segments N , such as shown on Figure 5.1 and each of them is loaded with a resistance.

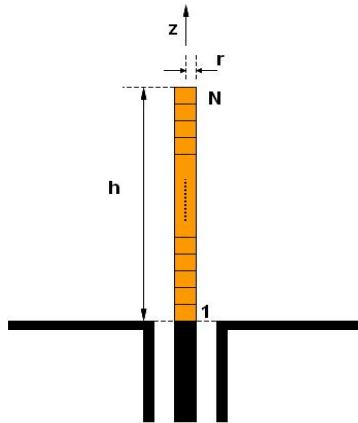


Figure 5.1: Scheme of the monopole with loaded segments

This defines a multidimensional problem of dimension equal to the number of segments N . In order to illustrate the complexity of the optimization of such monopole in terms of computational load, consider the following example:

The monopole presented on Figure 5.1 is divided into 20 segments and each of them is loaded with one resistor ($R_1, R_2, R_3 \dots R_{20}$), selected among a set of 100 different resistor values. In this example, the goal of the optimization is to find the combination of 20 resistors that give the best performance for example in terms of monopole's bandwidth. In order to do so, we need to try all variations of 20 resistors with repetition, among 100 resistor values. We need to use variations and not combinations, because the specific order of resistors is important. The total number of such variations is given by the expression (5.1), where $k=20$ and $n=100$ and attains the value of 10^{40} .

$$V_k'(n) = n^k \quad (5.1)$$

If a simulation of one single monopole loaded with 20 resistors would take for example 10 seconds, a simulation of all these combinations would take 10^{41} seconds. Taking into account that the age of the universe is $13.69 \cdot 10^9$ years (approx. $4.32 \cdot 10^{17}$ seconds) [NASA], the computation time would take $2.3 \cdot 10^{23}$ times longer.

Fortunately, the computational load of such a multidimensional problem can be simply reduced, by reducing the dimension of the problem, or using evolutionary optimization algorithms such as genetic algorithms or PSO. Evolutionary algorithms such as PSO can reduce significantly the computational load and converge very rapidly to the solution of the optimization problem [Robinson04].

5.1.2. Loading Profile

The dimension of the loaded antenna optimization problem is equal to the number of loading elements. Consequently, in order to reduce the dimension of the problem, the loading profile should be defined by fewer parameters. Instead of optimizing the value of each loading element separately, as shown in the previous example, a specific loading profile defined as a function of position along the antenna should be optimized.

A selection of the loading profile function is arbitrary. Rao used a capacitive loading defined as an exponential function with decreasing reactance towards the free ends of the antenna [Rao69]. Wu derived an impedance loading profile [Wu65] that can be approximated by a resistive loading, increasing towards the free ends of the antenna [Esselle90]. In this section a resistively loaded antenna is used to demonstrate how the dimension of the optimization problem can be reduced by a definition of a loading profile.

In our case, a resistive loading profile was defined as a parabolic function (expression 5.2) along the monopole length (wire monopole oriented along z -axis), because it allows a profile quite similar to the profile derived by Wu [Wu65].

$$R(z) = R_0 \cdot (z - z_0)^2 \quad (5.2)$$

In the expression (5.2) R_0 represents the aperture of the parabola and z_0 is the position of the parabola minimum with respect to the origin, $z=0$ (the feeding point of the monopole). By a variation of R_0 and z_0 , this type of parabolic loading profile allows three types of loading profile: increasing or decreasing towards the free end of the monopole, and also convex, as shown on Figure 5.2.

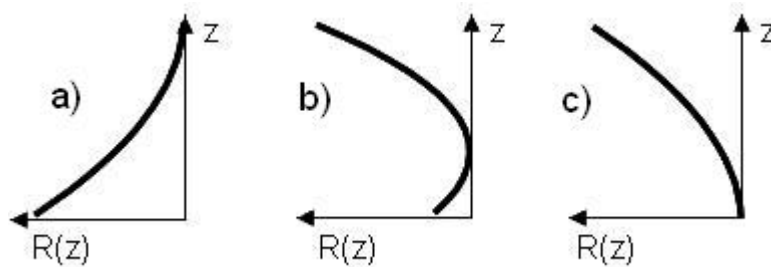


Figure 5.2: Parabolic loading function allows three types of loading profile: (a) decreasing, (b) convex and (c) increasing.

The goal of the optimization is to find the loading profile specified by the values of R_0 and z_0 that fulfils the desired antenna performance objective. By this way, the number of optimization variables was reduced from N (number of segments of the monopole, which was 20 in the previous example) to 2, which lowers the computational load.

The optimization of the loaded monopole was realized in Matlab[®] [MathWorks] using Numerical Electromagnetics Code (NEC) as electromagnetic simulator [Burke81]. NEC is free software, designed for the simulation of antennas made of wires and/or

patches. Each wire is defined by a set of coordinates of its two end points and modeled as a set of segments. Modeling a wire structure with segments involves geometrical and electrical factors. The main electrical consideration is the segment length related to the wavelength, whereas the main geometrical consideration is the segment length related to the radius of the wire [Burke81]. The segment length fulfilling electrical and geometrical criteria within the whole simulation bandwidth, determines the number of segments used to model each wire of the structure. The criteria on segment length ensure that the wire segments will have the form of cylinders but not disks.

5.2. Particle Swarm Optimization-PSO

The Particle Swarm Optimization is a robust stochastic evolutionary computation technique based on the movement and intelligence of swarms observed in the nature. This technique was developed in 1995 by Kennedy and Eberhart [Kennedy95] and applied to antenna design in 2002 by Robinson and Rahmat-Samii [Robinson02], who gave a conceptual overview of PSO and explained the algorithm, promoting its use in electromagnetic optimizations [Robinson04].

5.2.1. Basic Overview of PSO

The objective of this thesis is to use PSO for antenna optimization. Consequently, only the most important aspects of PSO needed here, are outlined.

Modeling the swarm of bees: Kennedy and Eberhart attempted to model a social behavior of a bird flock or fish school, that are moving to avoid predators, seek food etc. A very nice analogy, describing the behavior of the swarm of bees was reported by Robinson [Robinson04]. Robinson describes a swarm of bees in the flowered field that is trying to find a location with the highest density of flowers. The swarm does not have any knowledge about the field, its size, distribution of flowers etc. The bees look for flowers in random locations of the field and they are moving with random velocities from one flower to another. Each of them has the capacity to remember the place where it found the most flowers (nostalgia). Each of them has also the capacity to communicate with other bees in the swarm and to know the location where one of

these bees has found the most flowers of all (social influence). At each moment when the bee moves from one flower to another, its displacement depends on nostalgia and social influence; each of them influences in the resulting displacement by different weight. In this manner the bees explore the field and if there is one global maximum (a location that has the highest concentration of flowers) they will finish flying around this location.

PSO vocabulary: A specific vocabulary that will ease the use and understanding of such a nature inspired algorithm needs to be introduced. This vocabulary was defined by Kennedy [Kennedy95], and explained on the analogy of the bee swarm by Robinson [Robinson04].

particle: A bee is a particle. A particle is each individual in the swarm. In our case, a monopole loaded with a particular loading profile is a particle.

position: A geographical position of the bee in the 2-dimensional plane of the flowered field, given by its coordinates x and y . In our case, a position is represented by the coordinates of the particle within the N -dimensional space where the optimization solution is searched. The dimensions of this space are determined by the parameters to be optimized. In our case (resistively loaded monopole) the dimension is 2 and the position is determined by the pair R_0, z_0 .

fitness: The density of flowers is a fitness. Every bee knows where the other bees of the swarm are and what the density of flowers they have found is. This is the principle of evolutionary techniques. Each position in the optimization space has to have a fitness which is a measure of goodness of the position. In our case, fitness could be any antenna parameter such as gain, radiation efficiency, SAF_l , electrical size, etc. or any weighted sum of these parameters.

pbest: The location that each bee remembers and where it has personally found the highest density of flowers is the called *personal best* (*pbest*). In our case, it is the *position* with the highest *fitness* value personally discovered by a *particle* along the entire path travelled within the space where the solution is being searched.

gbest: The location of the bee that has found the highest density of flowers among all the bees from the swarm is called *general best (gbest)*. It is the *position* of the *particle* with the best *fitness* among all particles of the swarm.

PSO algorithm: The scheme of the PSO algorithm is shown on Figure 5.3. Prior to the execution of the loop shown on the flow graph on Figure 5.3, a *Solution Space* and *Fitness Function* have to be defined.

Solution Space: A *Solution Space* is defined by the range of the parameters that have to be optimized. Each of these parameters has to have a defined minimum and maximum. In the analogy with the bee swarm and flowered field, the *Solution Space* would be a 2-dimensional space defined by the coordinates x and y . A flowered field would be square field of 100 m by 100 m, so the minimum and maximum of x and y would be 0 m and 100 m respectively.

Fitness Function: The *Fitness Function* is the link between the algorithm and the physical world [Robinson04]. It represents a goodness of the solution in a single number. In the analogy with the bee swarm the Fitness Function would be the same as *fitness*. If several physical characteristics (such as density of flowers and their size) are to be optimized, a *Fitness Function* has to represent the weighted function of these characteristics. The weights represent the relative importance of each characteristic within the optimization problem.

Both, *Solution Space* and *Fitness Function* are specific for every optimization problem.

Once the *Solution Space* was defined it is important to initialize the swarm location within this space and the initial random velocities of each particle. The PSO optimization has to begin with all the swarm particles in some location. This location can be randomly chosen but it can also be chosen as uniform distribution of particles within the *Solution Space*. After this initialization the PSO algorithm such as shown on Figure 5.3 really begins, moving all the particles through the *Solution Space* one by one. First of all, just after the initialization the *fitness* of each particle is evaluated.

The *Fitness Function* gives the value of the *fitness* for a given position of the particle. If the fitness value of the particle is greater than the value of *pbest* or *gbest* then these attributes are given to the current location.

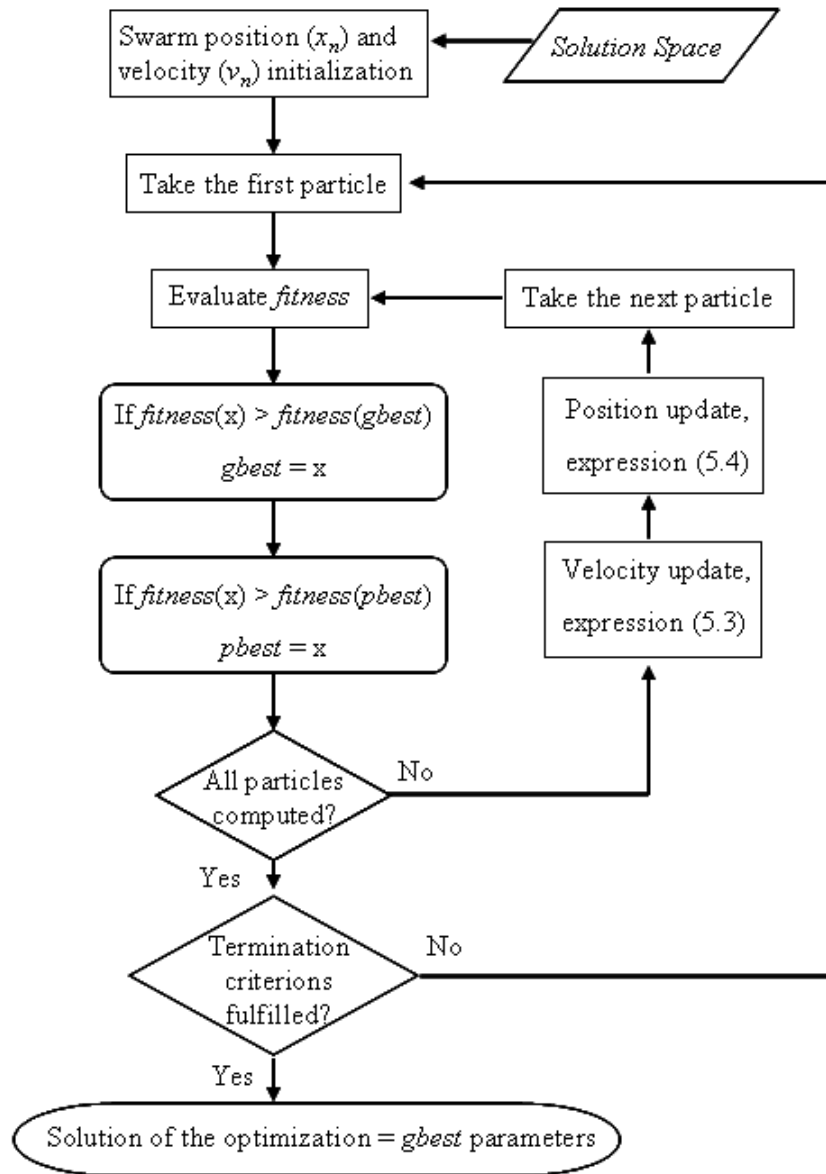


Figure 5.3: Flow chart of the PSO algorithm used in UWB monopole optimization. Coordinate of the particle in the n -th dimension: x_n , velocity of the particle in the n -th dimension: v_n .

The next step of the algorithm is the update of the particle's velocity. The velocity is updated according to the positions of particles with attribute *pbest* and *gbest*, such as defined by Robinson in [Robinson04] and given by the expression (5.3).

$$v_n = w.v_n + c_1.rand().(pbest_n - x_n) + c_2.rand().(gbest_n - x_n) \quad (5.3)$$

The new velocity of the particle v_n in the dimension n , such as given by the expression (5.3) is the weighted sum of the original velocity v_n and two velocity vectors pointing toward the positions of particles with attributes $pbest$ and $gbest$. In the expression (5.3) x_n is the coordinate of the particle in the n -th dimension. Similarly the quantities $pbest_n$ and $gbest_n$ are the coordinates of $pbest$, $gbest$ in the n -th dimension. The weighting in the velocity update is represented by coefficients w , c_1 and c_2 . The coefficient w is a random number between 0 and 1, which represents the inertia of the particle to continue with its original velocity. The coefficients c_1 and c_2 represent how much the particle is attracted towards the positions of $pbest$ and $gbest$. The function $rand()$ from the expression 5.3, returns a random number between 0 and 1, different in each multiplication of the constants c_1 and c_2 . This random component in the velocity update provides better exploration of the *Solution Space*.

The discussion on the influence of these weighting coefficients is not the objective of the thesis. More information on the topic of velocity update and weighting can be found in [Eberhart01] and [Robinson04]. The coefficients c_1 and c_2 are set to the value of 2, as suggested in [Robinson04].

An important thing to remark in the flow graph from Figure 5.3 is that the main loop, the core of the PSO, is repeated for each particle of the swarm in all iterations. This makes it very suitable for parallel execution on several processors, what can significantly reduce the computation time of the optimization.

After velocity update, each particle is moved to a new position within the *Solution space*. The update of the position is given by the expression (5.4), where Δt is a given time step usually taken equal to 1, as in our case.

$$x_n = x_n + \Delta t.v_n \quad (5.4)$$

More details on the problems of particle motion and its influence on the overall PSO performance can be found in [Robinson04].

The process described by the loop on the Figure 5.3 (fitness evaluation, velocity and position update) is repeated for every particle of the swarm. At each iteration (when the positions of all particles have been updated) the position of $pbest$ and $gbest$ are

updated. This process is repeated until the termination criterion is met. There are different ways of defining the termination criteria. The termination criteria can be: used-defined maximum number of iterations or user-defined target fitness. In our implementation of PSO we have used both termination conditions simultaneously.

One remaining important aspect of PSO is the definition of *Solution Space* boundaries. In engineering optimization problems it is often very important to limit the space where the solution is being searched to a physically relevant solution space. Robinson in [Robinson04] proposed three different types of boundary conditions:

- *absorbing walls*: when a particle hits the boundary, the velocity component orthogonal to the boundary is zeroed
- *reflecting walls*: when a particle hits the boundary it is reflected back, the orthogonal velocity component changes the sign
- *invisible walls*: particles are allowed to move without any restriction but once they go outside of the Solution Space their fitness is not evaluated.

In our PSO implementation the absorbing boundaries were used.

Finally the *elitism* within the swarm can be applied by giving priority to particles that are closest to the *gbest*. The priority means that the velocity of the particles is not actualized in the next iteration.

Once the optimization strategy was exposed, the implementation of PSO for UWB loaded monopole optimization is described in the following section.

5.2.2. PSO Implementation in Matlab

The PSO algorithm used in this thesis was inspired by the UCLA-PSO, whose principles are described in [Robinson04].

The frequency range used in all the simulations is going from 2.5 GHz to 10.5 GHz. The antenna feeding pulse is defined in frequency domain as a pulse having a flat spectrum in the whole frequency band of interest. It corresponds to a Sinc pulse in time domain.

The block diagram of the PSO algorithm implemented for impedance loaded UWB wire monopole is shown on Figure 5.4.

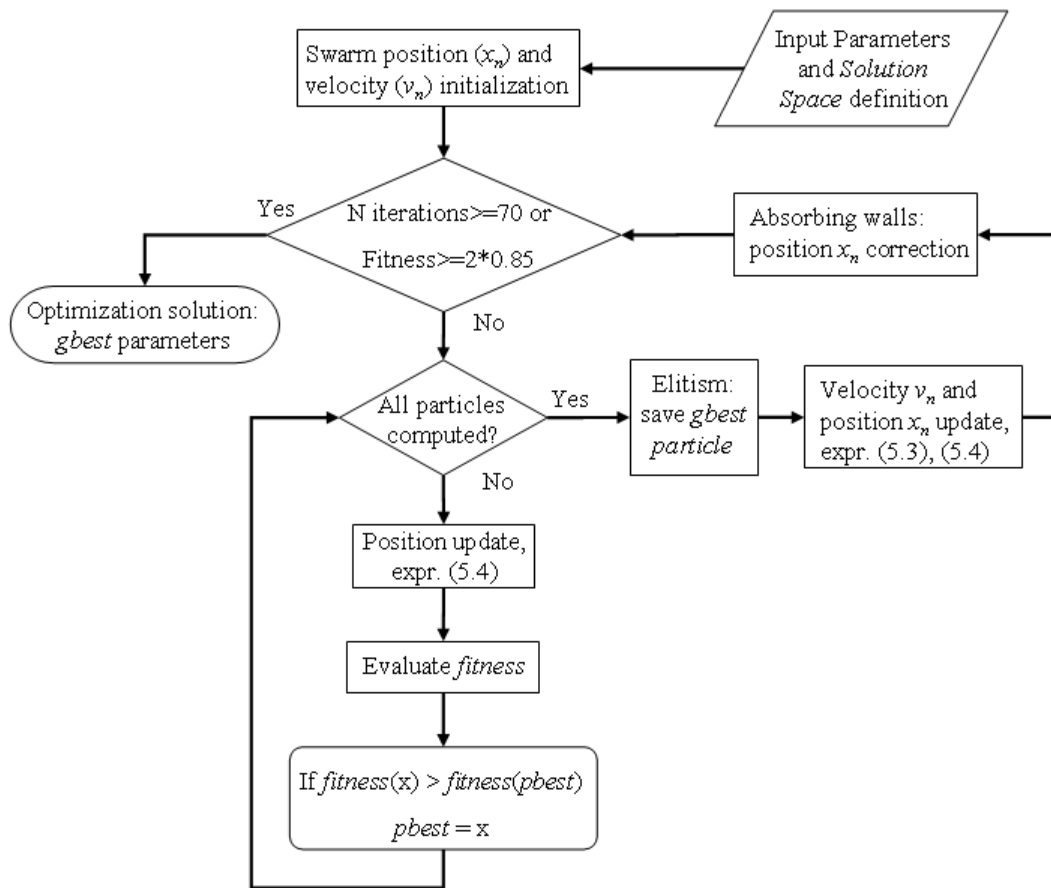


Figure 5.4: Flowchart of the PSO implementation in Matlab. Coordinate of the particle in the n -th dimension: x_n , velocity of the particle in the n -th dimension: v_n .

Values of commercially available resistors and capacitors were used in all simulations. Concretely, resistor series E12 (12 resistor values per decade with tolerance of 10%) with values between 0Ω and $1 \text{ M}\Omega$ (total of 86 resistor values) and capacitors from *muRata* capacitor kit, GRM18-KIT-B [Murata09] with values between 0.5 pF and $10 \mu\text{F}$ have been used.

The size of the swarm is also one of the important parameters of PSO. Based on parametric studies, Carlisle [Carlisle01] states that the optimal size of the swarm for many problems is 30 particles. In our implementation, the size of the swarm was set to 40.

The number of iterations is also determined empirically. Generally after a few first PSO runs the value of *fitness* in position *gbest* plotted as a function of number of iteration converges. In this manner, the number of iteration used in loaded antenna optimization problem was set to 70.

The termination criterion implemented was a combination of 2 criteria. The optimization stops when the iteration number reaches 70 or the *fitness* of the position *gbest* reaches 85% of target *fitness* value.

The position and velocity of all particles at initialization are random.

The *Solution Space* as well as the *Fitness Function* is determined specifically for every optimization problem (section 5.3 and section 5.4).

5.3. Resistively Loaded Monopole

5.3.1. Specific PSO settings

A wire monopole of length h , oriented along the z -axis and radius r was used as a candidate. The parabolic resistive loading profile, defined by the expression (5.2) was used. As mentioned before (section 5.2.2) the values of the loading function $R(z)$ were chosen from a commercially available resistors kit with values from 0Ω to $1 \text{ M}\Omega$. The parameters that are optimized (R_0 and z_0) define the dimension of the *Solution Space*. In order to define the range of the *Solution Space* the limits of R_0 and z_0 were set as: R_0 belongs to interval $[0; 10^{10}] \Omega/\text{m}^2$ and z_0 goes from $-h$ to $2h$. The length of the monopole is a parameter that will be discussed in the section 5.3.3.

The *Fitness Function* was defined by the expression (5.5) as a weighted sum of fidelity SAF_l and mean value of the radiation efficiency η over the whole frequency band.

$$fitness = k_1 \cdot SAF_l + k_2 \cdot mean(\eta) \quad (5.5)$$

The weighting coefficients depend on designer's choice. As mentioned before, a good UWB antenna should ideally have a good pulse transmission properties as well as high radiation efficiency. Consequently both antenna parameters (SAF_l and η) should be weighted by the same weight. For this reason the weighting coefficients k_1 and k_2 were set to 1. The radiation efficiency was scaled from the range 0-100% to the interval 0-1. As the maximum attainable value of radiation efficiency is 1 and maximum attainable value of fidelity SAF_l is also 1, thus the target *fitness* (maximum attainable fitness defined by the expression (5.5) and used as a termination criterion

parameter) was set to the value of 2. The optimization terminates if the number of 70 iterations is reached or if the *gbest* particle attains 85% of the target *fitness* value.

5.3.2. Resistive Profile Optimization

In order to show how the PSO does work an example is analyzed in this section. A resistively loaded wire monopole of 30 mm length and 0.8mm radius was optimized. Following the NEC wire segmentation criteria, the monopole was divided into 17 segments. The length and radius were arbitrarily chosen. The Figure 5.5 shows all the particles that were simulated.

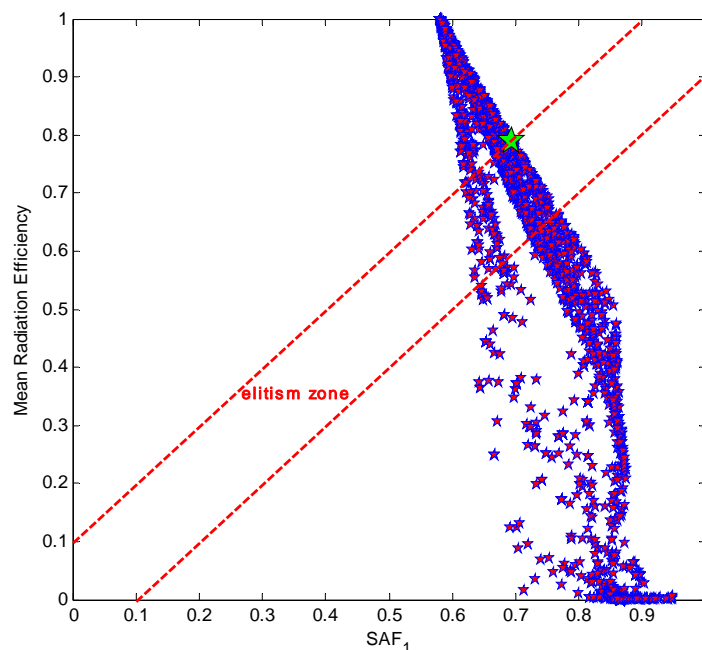


Figure 5.5: Pareto front of the optimization of a resistively loaded wire monopole (30 mm length; 0.8 mm radius). The big green star indicates the optimization solution obtained as a compromise between the mean radiation efficiency and average fidelity SAF_1 . The red lines delimitate the zone where the optimum solution is located and define the area used to apply the elitism.

Each star in the Figure 5.5 represents one particle position, which means one resistively loaded antenna, placed in the space defined by their values of fidelity SAF_1 and mean radiation efficiency. The optimum solutions should be located on the diagonal of the Figure 5.5, going from the point [0;0] to the point [1;1], because the fitness function was defined as equally weighted sum of fidelity and efficiency values. In order not to be so strict, rather than a diagonal line, a diagonal band (band between

the two red diagonal lines in the Figure 5.5) is considered, for optimum solution location. This diagonal band is used to realize *zone elitism* within the swarm, multiplying the fitness of particles outside the diagonal band by some constant lower than 1, here equal to 0.3. The particles in the Figure 5.5 formed a Pareto front, where the *gbest* particle (particle with the highest value of fitness) is indicated by the green star. The parameters of the solution of the optimization are given by the coordinates of the *gbest* particle in Figure 5.5: $SAF_l=0.69$ and $mean(\eta)=0.79$. No particle has reached the point [1;1] corresponding to the maximum fidelity and efficiency. Nevertheless the Pareto front shows what performance can be expected from a resistively loaded monopole in terms of SAF_l and mean radiation efficiency.

The initial position of the swarm at the beginning of the PSO run is shown on Figure 5.6. As in the previous figures in this section, the position of the *gbest* particle is marked by a green star. The initial swarm in the Figure 5.6 is randomly distributed in the *Solution Space*, defined by R_0 and z_0 . The initial *gbest* particle is in position [$R_0=2.29 \text{ k}\Omega/\text{m}^2$; $z_0=59.1 \text{ mm}$] and is shown by a big green star.

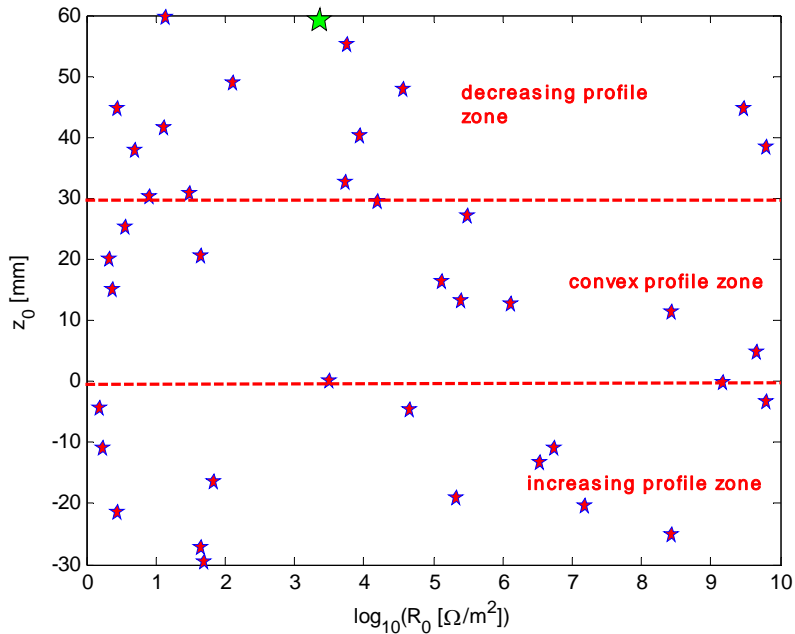


Figure 5.6: Initial random position of the swarm in the *Solution Space* (R_0 ; z_0) at the beginning of the optimization. The *gbest* particle is marked by the green star.

Obviously, the initial distribution of the swarm within the *Solution Space* on Figure 5.6 overlays the whole space. Through the course of the PSO the swarm is moving and explores the *Solution Space*.

The final position of the swarm (40 particles) in the *Solution Space* defined by R_0 and z_0 is shown on Figure 5.7. On horizontal axis the logarithm of R_0 is represented, for better visualization of the swarm distribution. The *gbest* particle is indicated by a green star and its position is [$R_0=18.76 \text{ k}\Omega/\text{m}^2$; $z_0=6.8 \text{ mm}$]. The corresponding loading profile is given by the set of 17 resistors, shown in the Table 5.1. NEC divided the 30 mm long monopole into 17 segments, respecting the segmentation criterions explained in [Burke81]. The segments are numbered from the feeding point of the monopole.

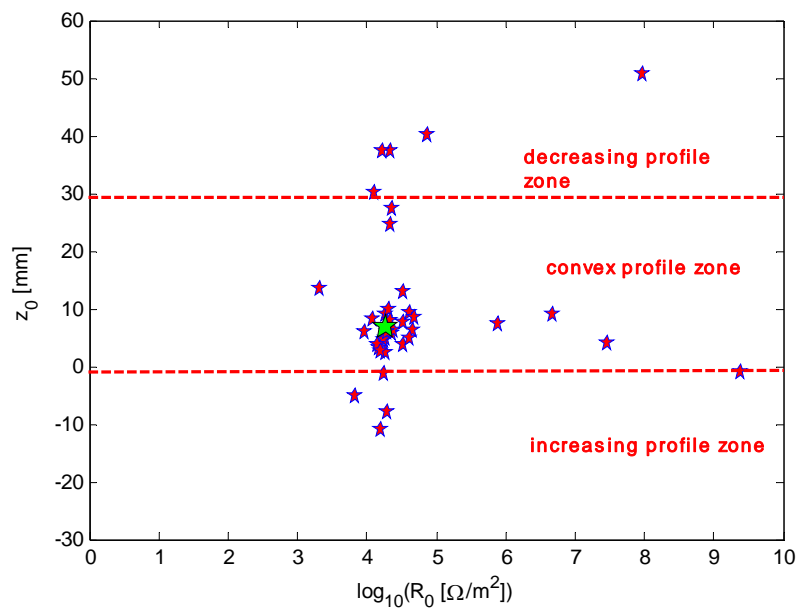


Figure 5.7: Position of the swarm in the *Solution Space* (R_0 ; z_0) at the end of the optimization. The *gbest* particle is marked by the big green star.

Table 5.1: Resistive profile of the solution for the resistively loaded 30 mm-long monopole

Segment	1	2	3	4	5	6	7	8	9	10	11	12	13	14	15	16	17
R [Ω]	0.68	0.33	0.1	0	0	0.15	0.39	0.82	1.2	1.8	2.7	3.3	4.7	5.6	6.8	8.2	10

All the explored positions of the *Solution Space* during the optimization run are shown on Figure 5.8. As can be observed from the comparison of the Figure 5.7 and the Figure 5.8, the highest density of particles is close to the position of the optimization solution (marked by a big green star) which is within the zone corresponding to a convex loading profile. A total amount of 2800 positions (40 particles in 70 iterations) was explored.

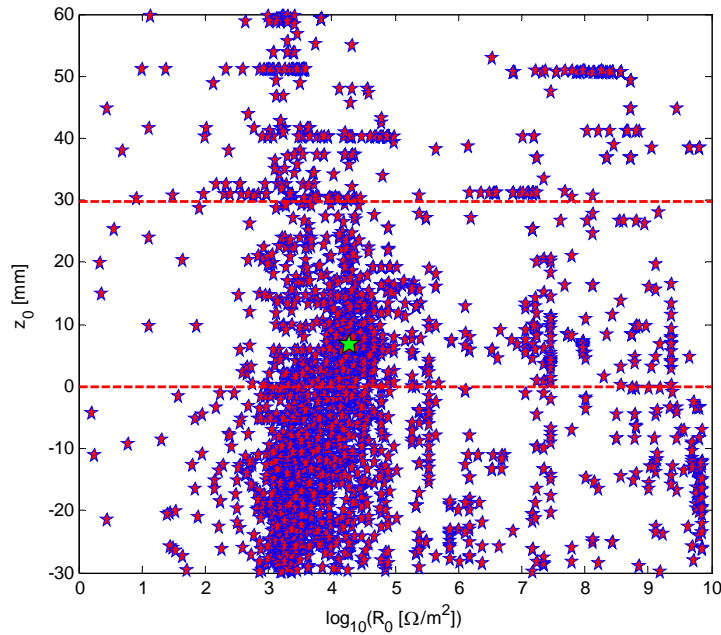


Figure 5.8: All simulated particle positions (40 particles . 70 iterations = 2800 positions) in the *Solution Space* (R_0 ; z_0). The *gbest* particle is marked by the big green star. The increasing, decreasing and convex profile zones are delimited by the red dashed lines, as in the previous figures.

For better illustration of the *zone elitism*, the fitness of all the simulated particles within the *Solution Space* is shown in Figure 5.9. Each star represents one particle. The red stars represent the particles within the diagonal elitism zone from Figure 5.5 (their fitness is the sum of SAF_1 and $mean(\eta)$). The blue stars represent the particles outside the elitism zone and their fitness is multiplied by 0.3. The *gbest* particle is represented by a big green star. The influence of *zone elitism* is evident from comparison of Figure 5.9 with Figure 5.10. The Figure 5.10 shows the fitness of all simulated particles without the *zone elitism*. In this case the *fitness* is the sum of SAF_1 and $mean(\eta)$ for all particles. There are several of them attaining a higher fitness values than the original *gbest* PSO solution.

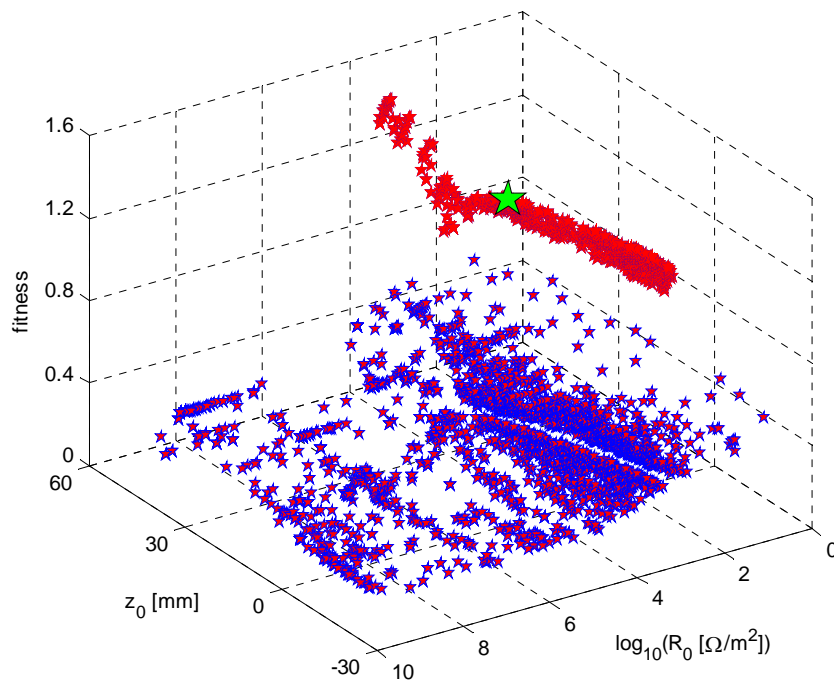


Figure 5.9: 3D representation of the fitness of all tested particles, within the *Solution Space* $(R_0; z_0)$, when the zone elitism is applied (diagonal band on Figure 5.5). The *gbest* particle is marked by the big green star and the particles from the elitism zone are marked by red stars.

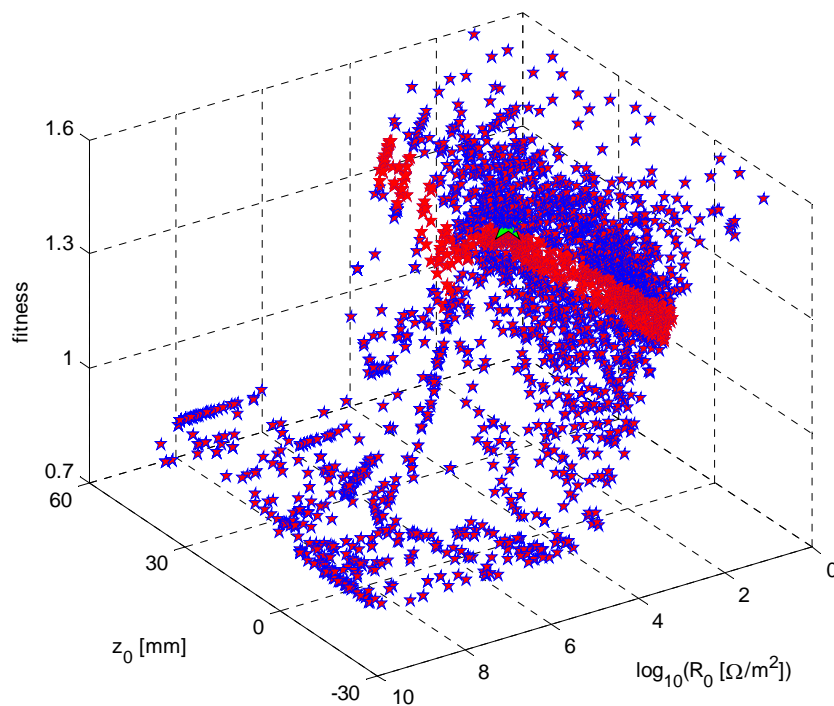


Figure 5.10: 3D representation of the fitness of all tested particles, without using the zone *elitism*, within the *Solution Space* $(R_0; z_0)$. The *gbest* particle is marked by the big green star and the particles within the elitism zone (diagonal band in Figure 5.5) are marked by red stars.

The evolution of the *gbest fitness* value during the PSO run is shown on Figure 5.11. The *fitness* converges to the value of 1.48 after approximately 55 iterations. It was verified that a much higher number of iterations than 70 does not give higher *fitness* than 1.48. The value of lowest fitness of the swarm, shown by green rectangles, is stable over all iterations while the value of the mean fitness of the swarm has an increasing tendency. This means that there are particles exploring the zones of the *Solution Space* that are far from the position of the *gbest* particle, but also that the main part of the swarm is converging towards the optimization solution.

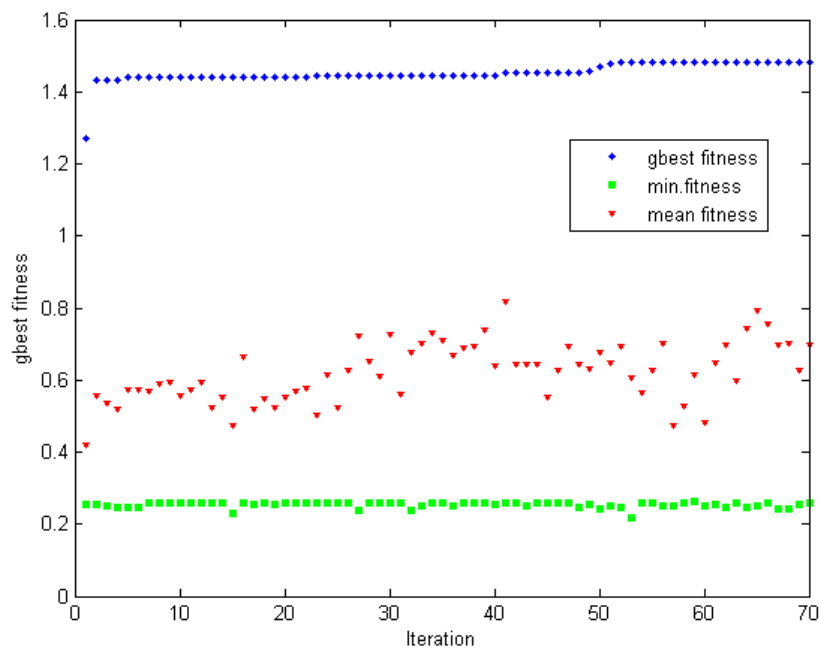


Figure 5.11: The evolution of the *gbest fitness* value, the highest fitness of the swarm (blue dots), the lowest fitness of the swarm (green squares) and the mean value of the swarm fitness (red triangles) during the optimization of the 30 mm long loaded monopole

In this section the mechanism of PSO algorithm was shown. The PSO parameters such as the size of the swarm (40 particles), number of iterations (70) and *Solution Space* range used in this example, will be used in all the simulations in the following sections.

5.3.3. Monopole Length

In the previous example (section 5.3.2) a 30 mm long monopole was optimized. The length of the monopole was arbitrarily selected. In this section several monopole

lengths close to 30 mm will be optimized, in order to see whether a better performance in terms of SAF_l and $mean(\eta)$ can be obtained. The Pareto fronts of three different monopole lengths (11.5 mm; 30 mm; and 40 mm) are shown on Figure 5.12, where each dot represents the explored particle position. For each monopole length, the best solution according to the compromise criterion of maximum SAF_l and $mean(\eta)$ is represented by a star symbol.

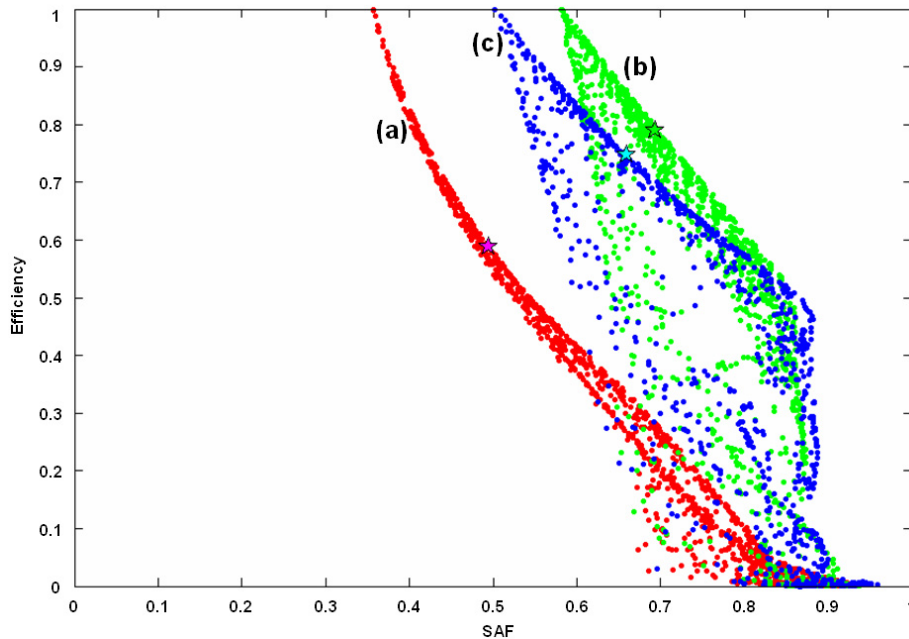


Figure 5.12: Pareto fronts for three monopole lengths (a) $h=11.5$ mm, (b) $h=30$ mm, and (c) $h=40$ mm [Miskovsky07b]

The empirically determined monopole length which gives the best performance in terms of fidelity SAF_l and $mean(\eta)$ is 30 mm, the same as the monopole length used in the section 5.3.2.

Radiated pulses from the 30 mm long monopole (oriented along z -axis) at four angular directions θ (10° , 30° , 60° and 80°) are shown in time domain on Figure 5.13 (solid line). They are compared with the source pulse (dotted line) used as template for SAF_l computation. The probe is located at 5.31 m. The radiated pulses are very similar to the template for $\theta=60^\circ$ and $\theta=80^\circ$. For $\theta=10^\circ$ and $\theta=30^\circ$ the pulse distortion is important compared to the main pulse peak, but still the major peak agrees with the position of the template maximum. The average fidelity SAF_l is 0.7, which means that the transfer function of the obtained antenna is highly wideband. The overall 3D

representation of radiated pulses (Figure 5.14) shows all angular direction between $\theta=0^\circ$ and $\theta=90^\circ$ and confirms the stable time position of the main peak.

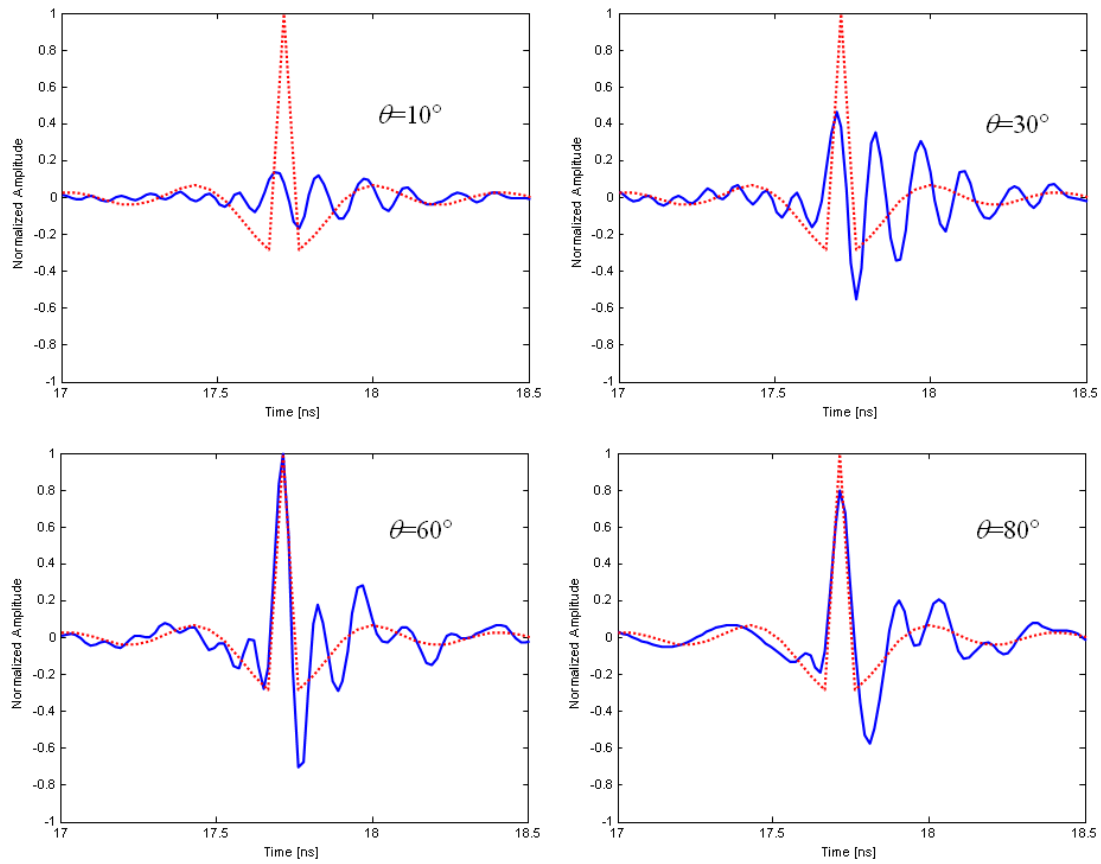


Figure 5.13: Amplitude and shape of the pulses radiated by the 30 mm long resistively loaded optimized monopole at different directions: $\theta=10^\circ$, $\theta=30^\circ$, $\theta=60^\circ$ and $\theta=80^\circ$. Radiated pulse (solid line), source pulse (dotted line).

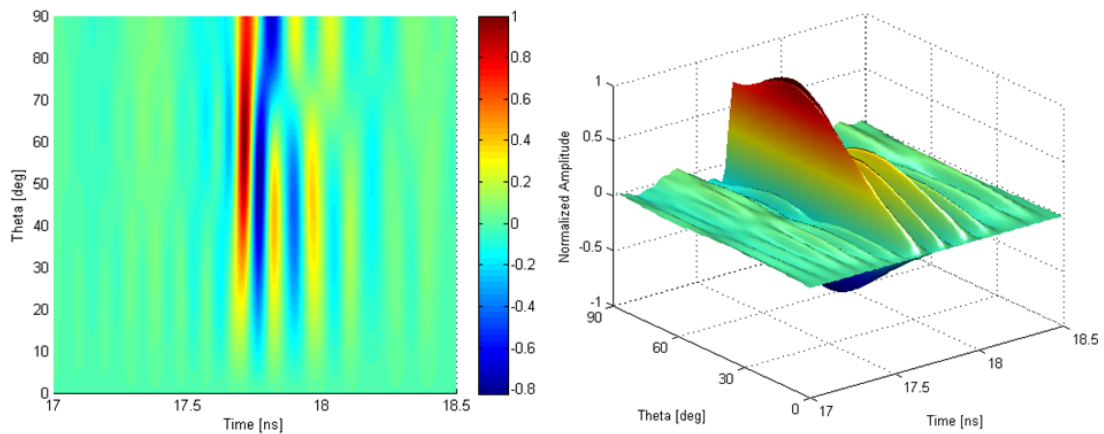


Figure 5.14: 3D representation of the pulses radiated by the 30 mm long resistively loaded monopole.

5.3.4. Discrete Resistor Tolerances

As mentioned previously, the resistor values used in the optimization are chosen from the commercially available set of resistors E12 which has a nominal value tolerance of 10%. In order to build the optimized resistively loaded antenna it is necessary to examine how this 10% resistivity value tolerance would influence the performance of the monopole. For this purpose a set of simulations was realized.

A routine that generates random uniformly distributed errors added to each of the loading resistors of the previously optimized 30 mm monopole and that computes SAF_l and mean radiation efficiency, was implemented in Matlab[®]. This error distribution process is repeated 100 times, meaning that 100 monopoles are loaded with the resistive profile from the Table 5.1 and that a random error is added to each resistor value. Tolerance of 5%, 10% and extreme case of 100% tolerance were simulated and the results are shown on Figure 5.15. The resistor tolerances of 5%, 10% and 100% introduce an approximate variation of 1%, 2% and 5% respectively, in both parameters SAF_l and mean efficiency. The resistive series E12 having a tolerance of 10%, is considered acceptable for the monopole construction.

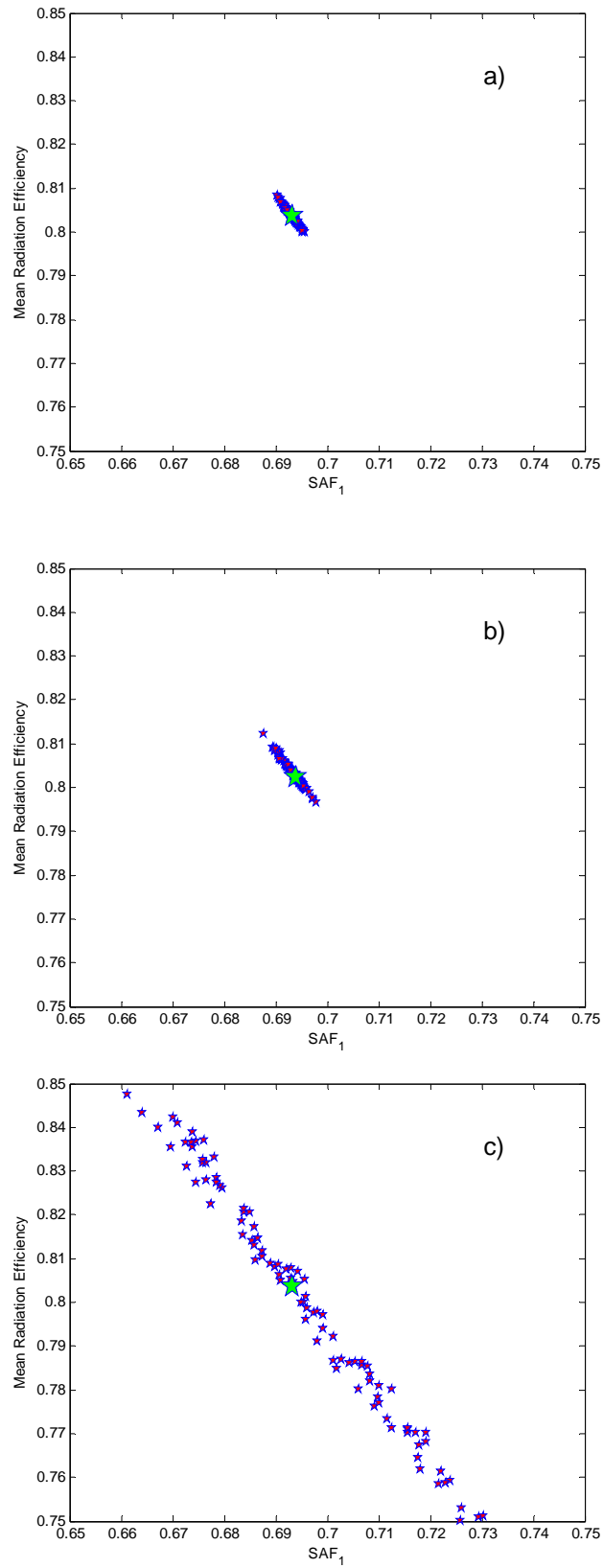


Figure 5.15: Influence of the resistor value tolerance (a) 5%, b) 10%, c) 100%) on the performance of the 30 mm long loaded monopole in terms of SAF_I and mean radiation efficiency

5.3.5. Discrete Resistors Parasitics

In high frequency circuit design, the impedance can change due to the parasitic inductance or capacitance introduced by the component package. An example of such behavior of RF resistors is shown in the datasheet of high frequency flat chip resistors [Vishay01]. Regarding the further construction of the optimized loaded monopole, the parasitics influence should also be taken into account during the optimization.

The parasitic impedance Z_C of the component package capacitance C is mainly due to the metallic contacts and the ceramic dielectric of the component. The parasitic impedance Z_L of the component package inductance L is due to the proper structure length of the component. Both parasitic effects are more visible at high frequencies due to their dependence on frequency as given by the expressions (5.6) and (5.7).

$$Z_C = \frac{1}{j \cdot 2\pi \cdot f \cdot C} \quad (5.6)$$

$$Z_L = j \cdot 2\pi \cdot f \cdot L \quad (5.7)$$

An example of an equivalent resistor circuit model containing the parasitic inductance and capacitance, (Figure 5.16 a) can be found in the datasheet of high frequency chip resistors [Vishay02] or in [Vishay03], where the variation of the nominal resistance value with respect to frequency is also shown. Unfortunately, this circuit model configuration from the Figure 5.16 a) can not be implemented in NEC simulator. In NEC, each wire segment can be loaded either by a purely series or a parallel RLC circuit. If two loading circuits are used in the same segment they are automatically connected in series [Burke81]. For this reason a circuit model configuration shown on Figure 5.16 b) is used [Herrero08]. It can be shown that both circuits from the Figure 5.16 are equivalent for small resistor values almost up to 50Ω , in the UWB frequency range. Since the optimized resistively loaded 30 mm monopole from the section 5.3.2 is loaded with small resistor values, the circuit model from the Figure 5.12 b) is valid for the demonstration of parasitics influence on optimized antenna performance. The values of parasitic inductance and capacitance used in the following simulations are $L=0.88$ nH, $C=35$ fF. These are the values of parasitics from the application note on resistors in microwave applications [Vishay03].

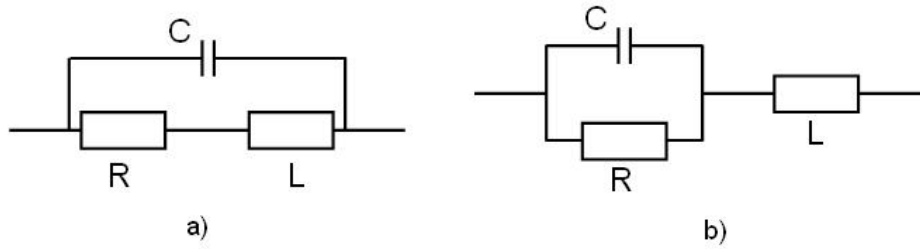


Figure 5.16: Equivalent circuit models of a resistor component with parasitic capacitance C and inductance L . a) model from Vishay [Vishay02], b) model implemented in NEC

In order to show the importance of parasitics in resistively loaded monopole, the same 30 mm long resistively loaded monopole was simulated with parasitic capacitance C and inductance L . Each monopole segment was loaded with a RLC circuit from the Figure 5.16 b) with the corresponding resistor value (Table 5.1) and the abovementioned inductance and capacitance. As shown on Figure 5.17, the performance of the monopole with parasitics, in terms of fidelity and efficiency is deteriorated. The average fidelity SAF_I decreased from 0.69 to 0.59 and the mean radiation efficiency decreased from 0.79 to 0.63 due to the additional losses of the resistors.

The result shown on Figure 5.17 means that if the 30 mm loaded monopole is optimized considering the parasitics; the resulting resistive profile would be different. For this purpose the PSO of such a monopole is realized in the same conditions (70 iterations, 40 particles) as in the section 5.3.2 and the resulting Pareto front is shown on Figure 5.18. The parameters of the optimum solution marked by a green star in the Figure 5.18 are $SAF_I=0.66$; $mean(\eta)=0.75$; $R_0=2.62e^8 \Omega/m^2$; $z_0=0.06$ m. The resistive profile of the optimum solution is shown in the Table 5.2.

Table 5.2: Resistive profile of the solution of 30 mm loaded monopole optimization with parasitics

Segment	1	2	3	4	5	6	7	8	9	10	11	12	13	14	15	16	17
R [Ω]	820	820	820	820	680	680	560	560	560	470	470	390	390	330	330	270	270

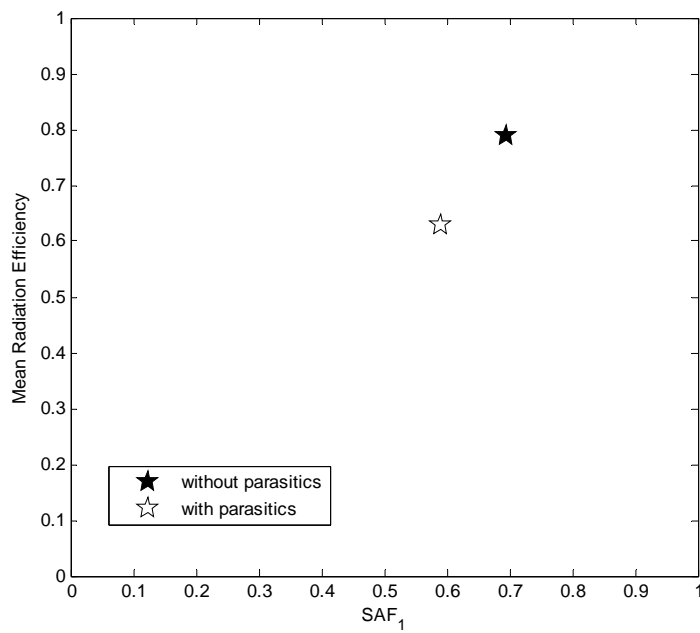


Figure 5.17: Optimum resistively loaded 30 mm monopole (Table 5.1) with and without considering the parasitic inductance and capacitance modeled by the RLC circuit from the Figure 5.16 b) ($L=0.875$ nH, $C=35$ fF).

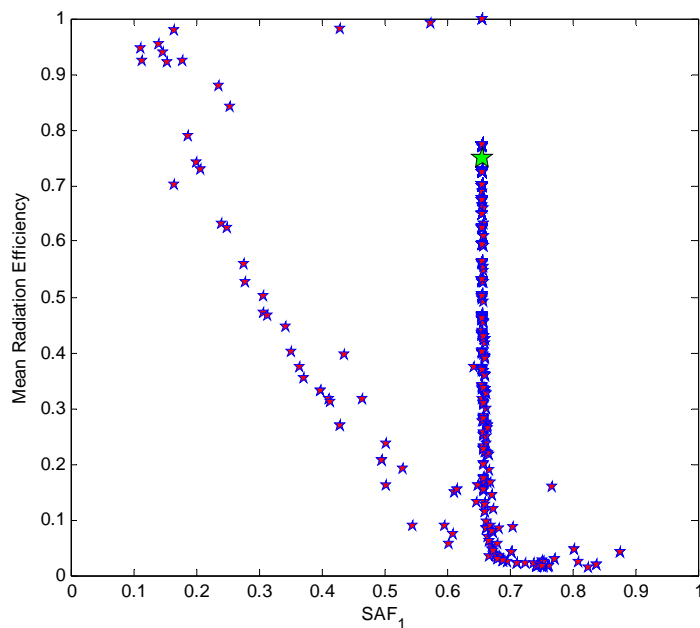


Figure 5.18: Pareto front of the resistively loaded 30 mm wire monopole, considering the parasitics ($L=0.875$ nH and $C=35$ fF). All the simulated positions are marked by red stars and the optimum solution by a green star.

The performance of the optimized solution with parasitics in terms of SAF_1 and efficiency is worst than in the case without parasitics, as expected. It is important to remark that the resulting resistive profile (Table 5.2) is decreasing contrary to the

solution profile from the Table 5.1 and that the values of resistors are much bigger (up to 1000 times bigger) than in the case without parasitics (Table 5.1). This is due to the frequency dependence of the parasitics. High resistor values compensate the impedances resulting from frequency dependent parasitics at high frequencies. In such way a good performance in terms of average fidelity and mean efficiency is obtained. The problem is that for such high values of resistance, the equivalence of circuit models from the Figure 5.16 is not preserved. Moreover for such high resistivity values the values of the parasitics would be much higher as 0.875 nH and 35 fF, as shown in [Vishay03]. Nevertheless, the objective of this section was only to illustrate the discrete component parasitics influence on the performance of the optimized antenna, but not to make an accurate quantification of its consequences.

5.3.6. PSO Solution Analysis

In the previous sections (from 5.3.2 to 5.3.6) a resistively loaded monopole optimization was shown. Optimization issues related to resistor series tolerances and discrete resistor parasitics were outlined because the objective is to build the optimized monopole and to assess its performance experimentally.

Contrary to resistor series tolerances, the effect of parasitics on monopole performance is quite important in the sense that taking them into account gives a different optimum resistive profile. For this reason it would be ideal if the resistively loaded monopole could be fabricated without the need of considering the parasitics. There are different ways how to achieve it, as will be shown in Chapter 6.

A closer examination of the resistive profile from Table 5.1 shows that first segments are loaded with very small resistances, lower than 1 Ω . This raises the idea that if these resistances would be removed, the overall performance of the optimum monopole should not change. In this way the construction of such a monopole would need fewer resistors and would certainly be cheaper. In order to verify this suggestion several simulations have been realized, removing up to 15 resistances, starting from the feeding point of the monopole. The evolution of the optimum solution performance (from section 5.3.2) in terms of SAF_l and mean efficiency is shown in Table 5.3.

Table 5.3: Evolution of SAF_1 and mean efficiency as a function of the number of removed resistors (N) starting from the feeding point of the monopole

N	1	2	3	4	5	6	7	8	9	10	11	12	13	14	15
SAF_1	0.69	0.69	0.69	0.69	0.69	0.69	0.69	0.69	0.69	0.68	0.68	0.67	0.65	0.63	0.6
$mean(\eta)$	0.79	0.79	0.79	0.79	0.79	0.79	0.8	0.8	0.81	0.82	0.83	0.85	0.88	0.92	0.96

Almost 8 first resistors could be removed from the 30 mm monopole, without changing its performance. Removing more than 8 resistors would change the monopole performance such as shown on Figure 5.19.

When the resistors 9, 10, 11 etc. are being removed, the particle representing the solution monopole is moving along the Pareto front in the space defined by SAF_1 and mean efficiency, shown by the red arrow on Figure 5.19. When all resistors are removed, the monopole becomes an ordinary $\lambda/4$ resonant monopole marked by a blue star in the Figure 5.19, with 100% radiation efficiency and average fidelity of almost 60%.

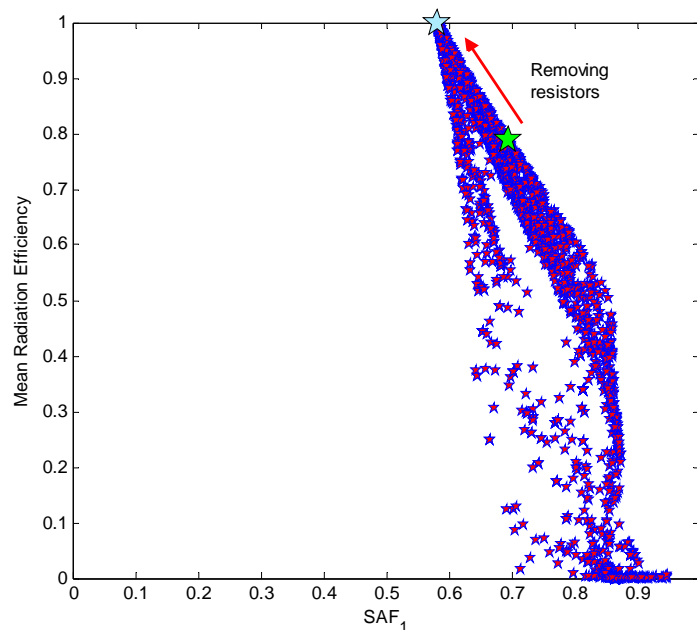


Figure 5.19: Pareto front of the resistively loaded 30 mm long monopole. The *gbest* particle is marked by the big green star and the, the resonant $\lambda/4$ monopole without any loading is marked by the big blue star.

5.4. Capacitively Loaded Monopole

A capacitively loaded monopole was optimized in terms of fidelity SAF_l and reflected energy at the feeding point. As will be explained further in this section, the radiation efficiency was not considered in the optimization because the capacitive loading should give efficiencies close to 100%.

5.4.1. Specific PSO Settings

A wire monopole oriented along z -axis with the same physical dimensions as the resistively loaded monopole ($h=30$ mm, $r=0,8$ mm) was used as a basic structure. The capacitive loading profile, optimized on such wire monopole follows an exponential distribution (5.8), as defined by Rao [Rao69], with capacity decreasing towards the end of the monopole. The capacities (5.8) are computed for positions z corresponding to the centers of the monopole segments.

$$C(z) = C_0 \cdot (e^{\alpha z} - 1)^{-1} \quad (5.8)$$

The *Solution Space* of the optimization was defined by the parameters that are to be optimized (C_0 and exponent α). The limits of C_0 and α were set as: C_0 belongs to interval $[8.863e^{-16}; 4.1473e^{-10}]$ and α goes from 0.001 to 10. In such way all the optimized capacity values are within the range of a commercially available capacitor kit GRM18-KIT-B [Murata09], going from 0.5 pF and 10 μ F.

Capacitively loaded antenna has practically no ohmic losses, compared to the case of resistively loaded antenna and its radiation efficiency should be very close to 100%, (of course the simulations agree with this expectation). For this reason it makes no sense to optimize this kind of antenna in terms of radiation efficiency. Instead of radiation efficiency, the antenna input port match was optimized. The goodness of input port match over the whole frequency band of interest was expressed in terms of the amount of energy reflected at the antenna feeding point E_{refl} . The goal of the optimization was to obtain a monopole with maximum SAF_l and minimum E_{refl} . The *Fitness Function* used in the capacitively loaded antenna optimization was defined in terms of average fidelity SAF_l and energy accepted at the input port E_{acc} , given by the expression (5.9), where $E_{acc} = 1 - E_{refl}$.

$$fitness = K.(k_1.SAF_1 + k_2.E_{acc}) \quad (5.9)$$

The reason for the definition of the *Fitness Function* in terms of accepted energy E_{acc} instead of reflected energy E_{refl} , is simply that in this way the goal of the optimization will be to maximize the fitness of the swarm. The reflected energy E_{refl} is computed from the expression (5.10).

$$E_{refl} = \int_{f_1}^{f_2} |S_{11}(f) \cdot P(f)|^2 df \quad (5.10)$$

where S_{11} is the reflection coefficient at the input port of the optimized antenna respect to 50Ω , f_1 and f_2 are the frequencies that define the frequency band of the simulation (2,5 and 10,5 GHz respectively) and $P(f)$ is the spectrum of the feeding pulse (defined as a unitary flat spectrum over the whole simulation frequency range). Weighting both antenna parameters (SAF_1 and E_{acc}) by the same weighting coefficients ($k_1=k_2=1$) and the definition of the Fitness Function by the means of E_{acc} defines the target *fitness* as equal to 2. The boundaries defined to implement the elitism within the swarm, will be explained in section 5.4.2. The optimization termination criteria are the same as in the previous resistively loaded monopole optimization (85% of target *fitness* and/or 70 iterations).

5.4.2. Capacitive Profile Optimization

The Pareto front of the 30 mm long monopole loaded with capacitive Rao profile is shown on Figure 5.20, in the space defined by average fidelity SAF_1 and reflected energy. The solution of the optimization ($SAF_1=0.57$; $E_{refl}=0.3$), marked by the big green star, represents the compromise between the minimum reflected energy and maximum fidelity performance. On the Figure 5.20 is represented the reflected energy, that should be minimized and fidelity that should be maximized, so the most optimum solution would be located at point [1;0]. No particle has reached the point [1;0] corresponding to the maximum average fidelity and minimum of reflected energy. Nevertheless the Pareto front shows what performance can be expected from a capacitively loaded monopole in terms of SAF_1 and E_{refl} . Regarding the position of the optimum solution [1;0], the elitism was realized by the definition of boundaries 1 and

2, as shown on Figure 5.20, where the *fitness* of the particles within each particular zone was multiplied by a different constant K .

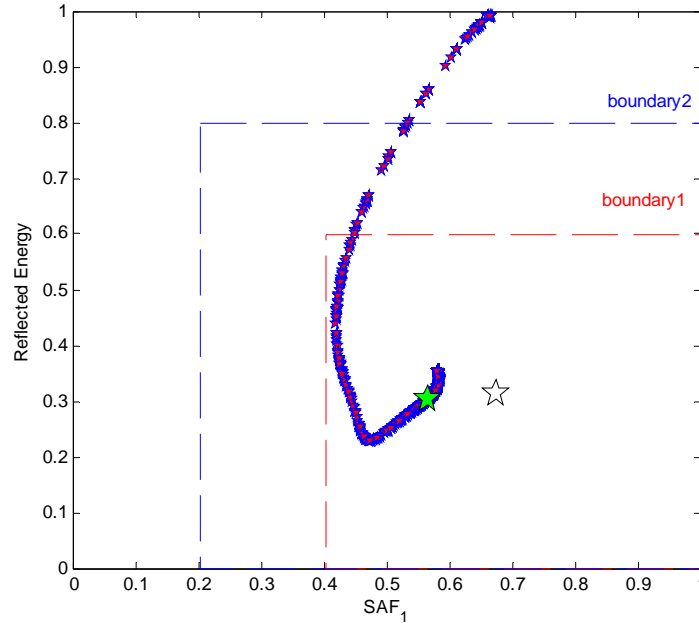


Figure 5.20: Pareto front of the 30 mm long monopole loaded with the capacitive profile defined by Rao [Rao69]. The *gbest* particle is marked by a big green star and the resistively loaded monopole from the section 5.3.2 is marked by a big white star.

Within the zone marked by boundary 1 the fitness value was not changed, between the boundaries 1 and 2, $K=0.6$ and outside the boundary 2, $K=0.2$. The reflected energy was scaled from 0-100% to the interval 0-1, for better graphical representation.

The parameters of the optimum solution from the Figure 5.20 are $C_0=1.5e^{-12}$ and $\alpha=10$. The values of the capacitive loading profile are shown in Table 5.4.

Table 5.4: The capacitive profile of the solution of 30 mm loaded monopole optimization.

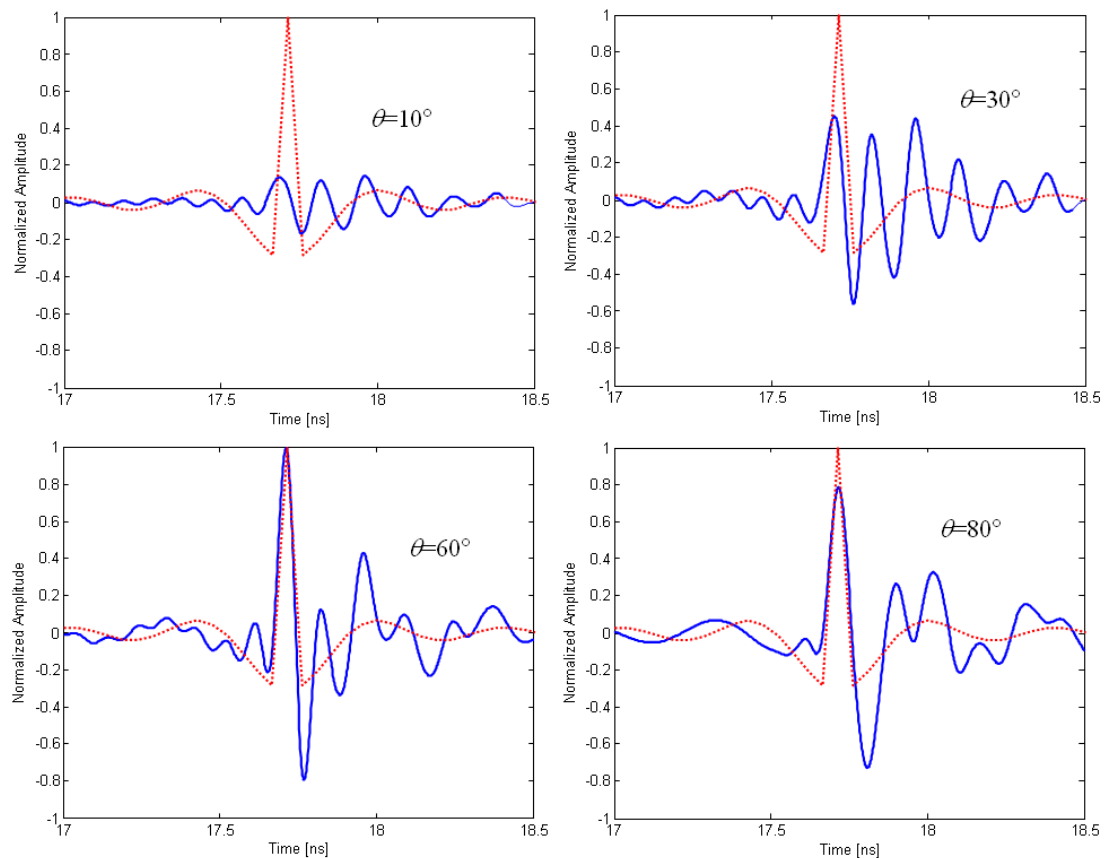
Segment	1	2	3	4	5	6	7	8	9	10	11	12	13	14	15	16	17
C [pF]	169	55.9	33.2	23.5	18.1	14.7	12.3	10.6	9.3	8.2	7.3	6.7	6.1	5.6	5.1	4.8	4.4

The optimized resistively loaded monopole from the section 5.3.2 was represented by a big white star in the Figure 5.20, for comparison with the optimum capacitively loaded monopole. The comparison is summarized in Table 5.5. The capacitively loaded monopole has worst performance in terms of average fidelity and is practically as well impedance matched at the feeding point as the resistively loaded monopole

Table 5.5: Performance comparison of the optimized resistively and capacitively loaded monopoles

Type of loading	resistive	capacitive
Mean radiation efficiency	0.79	1.00
Average fidelity SAF_I	0.69	0.57
Reflected energy E_{refl}	0.31	0.30

The pulses radiated by the 30 mm long capacitively loaded monopole (oriented along z -axis) at four angular directions θ (10° , 30° , 60° and 80°) are shown in time domain on Figure 5.21 (solid line). They are compared with the source pulse (dotted line) used as template for SAF_I computation. The probe is located at 5.31 m from the monopole.

**Figure 5.21:** Amplitude and shape of the pulses radiated by the 30 mm long capacitively loaded optimized monopole at different directions: $\theta=10^\circ$, $\theta=30^\circ$, $\theta=60^\circ$ and $\theta=80^\circ$. Radiated pulse (solid line), source pulse (dotted line).

The radiated pulses are very similar to the template for $\theta=60^\circ$ and $\theta=80^\circ$. For $\theta=10^\circ$ and $\theta=30^\circ$ the pulse distortion is important compared to the main pulse peak, but still the major peak agrees with the position of the template maximum. The overall 3D

representation of radiated pulses (Figure 5.22) shows all angular direction between $\theta=0^\circ$ and $\theta=90^\circ$ and confirms the stable time position of the main peak.

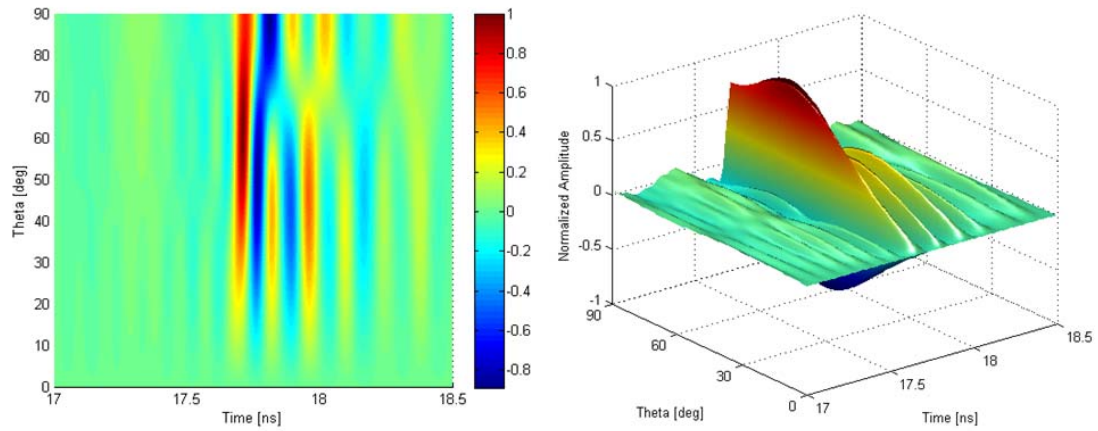


Figure 5.22: 3D representation of the pulses radiated by the 30 mm long capacitively loaded monopole

The objective of capacitively loaded monopole optimization was to design an antenna with good fidelity but also with good impedance match over the operational frequency band, expressed in terms of the amount of reflected energy E_{refl} . The reflection coefficient S_{11} of the optimized monopole with respect to 50Ω , has a typical resonant behavior as shown on Figure 5.17.

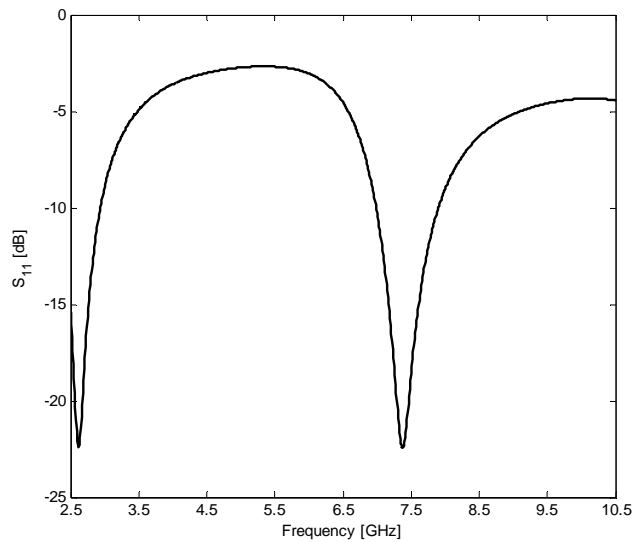


Figure 5.17: The reflection coefficient S_{11} (50Ω) of the optimized 30 mm long capacitively loaded monopole.

5.5. Conclusions

The design and optimization of two UWB monopoles were shown in this chapter. The need of evolutionary optimization technique was demonstrated and finally a technique called Particle Swarm Optimization was used. The basic principles and vocabulary of the PSO were outlined and some details of its implementation in Matlab[®] were shown.

A resistively loaded monopole of 30 mm length and constant radius 0,8 mm was optimized using PSO in terms of radiated pulse average fidelity SAF_l and mean radiation efficiency $mean(\eta)$. A resistive profile of such a monopole was defined by a parabolic function, allowing three types of profile shapes, increasing, decreasing towards the ends of the antenna and convex. The decreasing profile is similar to the profile defined by Wu [Wu65] for travelling wave antenna, providing wide bandwidths, and consequently interesting in the context of UWB monopole design. The influence of commercial discrete resistor component tolerances and parasitics was shown. The tolerance of the E12 resistor series used in all simulations does not influence significantly on the performance of the optimized monopole. The parasitics effects of the discrete component package influence seriously the monopole performance. Thus for the monopole fabrication some method without the need of considering the parasitics should be used. The solution profile of resistive monopole optimization was simplified removing some of the resistors with values inferior to 1 Ω , in order to simplify and cheapen the fabrication.

The capacitively loaded monopole of 30 mm length and wire radius of 0,8 mm was optimized, using PSO in terms of radiated pulse average fidelity SAF_l and amount of reflected energy E_{refl} at the monopole input port. The advantage of such monopole is that the radiation efficiency practically equals 100% because of the lack of ohmic losses.

The performances of the optimum capacitively loaded monopole and optimum resistively loaded monopole of the same length were compared in terms of SAF_l , $mean(\eta)$ and E_{refl} . The resistively loaded monopole attains better performance than the monopole with capacitive loading in terms of fidelity SAF_l . Its radiation efficiency is obviously lower than the efficiency of the capacitive monopole. The performances of

both monopoles in terms of the input reflected energy are almost the same. The simulation results presented in this chapter show what performance can be expected from such loaded monopoles in terms of spatially averaged fidelity, radiation efficiency and amount of energy reflected at the input port.

It can be concluded that the third aim of the thesis, the design and optimization of UWB antenna using a direction independent figure of merit fidelity SAF_l was attained. The performance of both resistively and capacitively loaded monopoles will be verified experimentally in Chapter 6.

Our contribution in this chapter can be summarized as follows:

- 1) Demonstration of resistively and capacitively loaded linear monopoles performance in terms of SAF_l , $mean(\eta)$, $E_{refl.}$, using PSO.
- 2) Comparison of capacitive and resistive loading performances, showing that the capacitive loading would be preferable for most UWB loaded antenna designs due to much higher radiation efficiency than the resistive loading.

6. LOADED MONOPOLE FABRICATION AND MEASUREMENT

In this chapter the previously designed monopoles are fabricated and their performance is verified through measurements in terms of the parameters that were used in the optimization: radiated pulse average fidelity SAF_l , mean radiation efficiency $mean(\eta)$, and reflected energy E_{refl} at the input port.

As demonstrated in the previous chapter, the parasitics of the discrete components can seriously influence the performance of the resistively loaded monopole. In order to reduce parasitics influence on antenna performance, notoriously accentuated at high frequencies, two solutions were proposed. The first is to use the geometrical antenna scaling into a low frequency range, where the parasitics effects are reduced, as a proof of concept to assess the figures given by the simulation. The second approach is to use components without package, such as resistors made of very thin resistive sheet. In this chapter both solutions are shown.

Firstly a fabrication of resistively loaded monopole was treated, using discrete resistors and secondly the capacitively loaded monopole, using discrete capacitors was fabricated.

Finally a parasitics-free approach to the resistively loaded monopole fabrication using very thin metal layers deposited through evaporation is shown in this chapter.

6.1 Scaled Resistively Loaded Monopole

The antenna geometrical scaling is a usual practice for very large antenna structures such as antennas for ships or aircrafts that are cumbersome for *in situ* measurements but also for very small antennas that due to their small size would be complicated and expensive to build [Cardama98], [Balanis97]. For the purpose of proving the concept of UWB impedance loaded monopole design in terms of average fidelity SAF_l , the scaling of antenna parameters was used in order to fabricate resistively loaded and capacitively loaded monopoles, as indicated in Table 6.1.

Table 6.1: Geometrical scaling of antenna parameters [Balanis97]

Length	$l' = l/n$
Wavelength	$\lambda' = \lambda/n$
Capacitance	$C' = C/n$
Inductance	$L' = L/n$
Effective area	$A_{eff}' = A_{eff}/n^2$
Frequency	$f' = n.f$
Conductivity	$\sigma' = n.\sigma$
Permittivity	$\epsilon' = \epsilon$
Permeability	$\mu' = \mu$
Impedance	$Z' = Z$
Antenna gain	$G' = G$

6.1.1 Fabrication Process

The scaling factor n was chosen to be equal to 5. This allows the scaling of the monopole from the original frequency band (2.5-10.5) GHz to the band (0.5-2.1) GHz where the parasitics should practically not influence the monopole performance. Thus, the original 30 mm-length and 0.8 mm-radius wire monopole was scaled to a 150 mm-length and 4 mm-radius monopole, following the rules from Table 6.1.

The values of resistors are not affected by the scaling. Consequently the scaled monopole was fabricated, loaded with the optimum resistive profile from the section 5.3 and indicated in the Table 5.1, the first 8 resistors being set to 0 Ω , for easier fabrication as explained in the section 5.3.6. In order to recall its optimized performance, the average fidelity and mean efficiency of the corresponding resistive monopole are: $SAF_I=0.69$, $mean(\eta)=0.8$.

The performance of the scaled 150 mm resistively loaded monopole (radius $r=4$ mm) in terms of average fidelity and mean efficiency was verified by simulation. As expected, the obtained values are practically the same ($SAF_I= 0.66$, $mean(\eta)= 0.8$) as in the case of 30 mm resistively loaded monopole. Originally the monopole was simulated as a thin wire of cylindrical shape with 0.8 mm radius. Consequently, the scaled monopole radius is 4 mm. In order to fabricate such a monopole using very thin copper strips (35 μm thickness), the equivalent strip width should be 16 mm as explained in [Balanis97]. The 16 mm wide strip would be too wide for the fabrication purposes, compared to the size of discrete resistors. As a consequence, the width of the strip was arbitrarily set to 5 mm for a fabrication convenience. The influence of such width adjustment on scaled monopole performance in terms of average fidelity and mean radiation efficiency is demonstrated by simulated results shown in Table

6.2. It is important to note that setting the antenna width to 5 mm has changed the value of average fidelity to $SAF_I=0.53$. For the fabrication of 150 mm long 5 mm wide, resistively loaded monopole, the set of the resistors shown in Table 6.3 was used.

Table 6.2: Influence of the scaling on simulated, resistively loaded monopole performance

length [mm]	30	150	150
wire radius [mm]	0.8	4	1.25
equivalent strip width [mm]	3.2	16	5
SAF_I	0.69	0.66	0.53
$mean(\eta)$	0.8	0.8	0.81

Table 6.3: The resistive profile of the 150 mm scaled monopole using commercially available resistor values

Segment	1	2	3	4	5	6	7	8	9	10	11	12	13	14	15	16	17
R [Ω]	0	0	0	0	0	0	0	0	1.2	1.8	2.7	3.3	4.7	5.6	6.8	8.2	10

The upper part of the monopole loaded with the SMD power resistors (MEGGITT CGS, type 3520 series), was made of a piece of ARLON 25N substrate ($\epsilon_r=3.38$) of thickness 0.508 mm and width 5mm and used as the support. The resistors were then placed soldered on copper segments as illustrated on Figure 6.1.

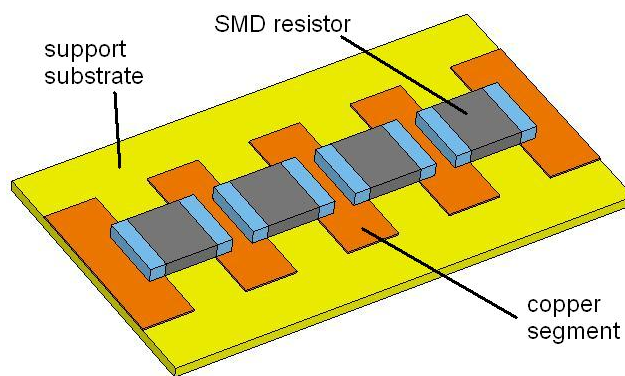


Figure 6.1: Fabrication detail of the monopole resistive loading

Instead of 0Ω resistors, the first lower part of the monopole was made of a copper strip, as shown on Figure 6.2.

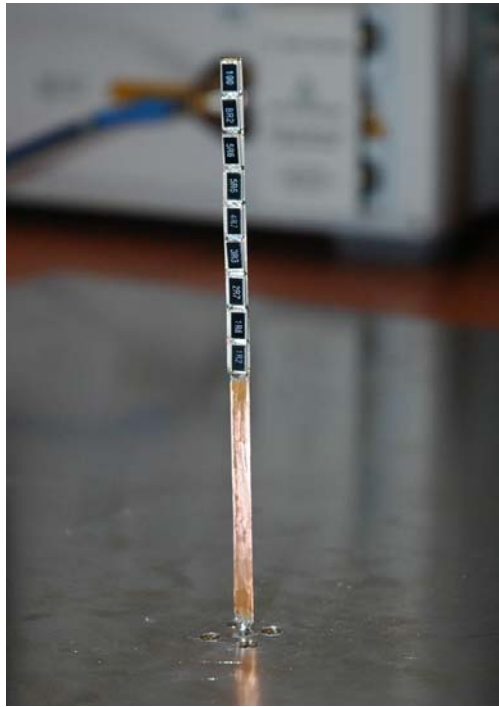


Figure 6.2: Optimized resistively loaded monopole from the section 5.3, scaled to the frequency range from 0.5 GHz to 2.1 GHz. Instead of using resistors with 0Ω , a copper strip was used in the first section of the monopole. The monopole is mounted on a 60 cm by 60 cm ground plane and fed by a standard SMA connector.

6.1.2 Characterization of the Resistively Loaded Monopole

As the antenna was scaled, all the measurements were performed and shown in the scaled frequency range 0.5GHz - 2.1 GHz.

The measurement of SAF_l : The value of average fidelity SAF_l was measured as explained in Chapter 4, using the maximum correlation criterion. The measurement was performed in the anechoic chamber at UPC facilities, adequately calibrated as already explained. The feeding pulse and the Template pulse for SAF_l computation were also defined in Chapter 4, but here the definition extends only over the scaled frequency band ranging from 0.5 GHz to 2.1 GHz and over the angular range $\theta=0^\circ$ to $\theta=90^\circ$. An example of the anechoic chamber calibration procedure, as explained in Chapter 4, is shown on Figure 6.3 (see sections 4.1.1 and 4.3)

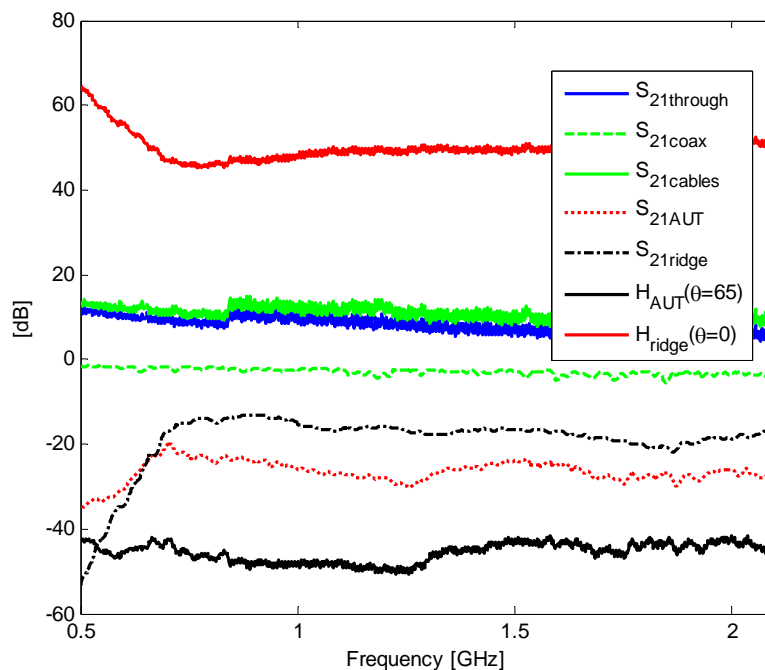


Figure 6.3: Anechoic chamber calibration procedure from Chapter 4, for the resistively loaded monopole (Figure 6.2) measurement at distance $R=5.31$ m from the probe.

The measured value of SAF_l is 0.57. This is 0.4 higher than the simulated value of the scaled antenna (0.53) shown in Table 6.2, which is an acceptable measurement error (4%). The comparison of measured radiated pulses with the template and simulated pulses for three angular directions ($\theta=10^\circ$, 30° , 60° and 80°), is shown on Figure 6.4. The agreement between the measured and simulated pulses is very good especially because of the position of the main pulse peaks. The Figure 6.5 gives an overall idea of the measured radiated pulses through all angular directions, up to $\theta=180^\circ$.

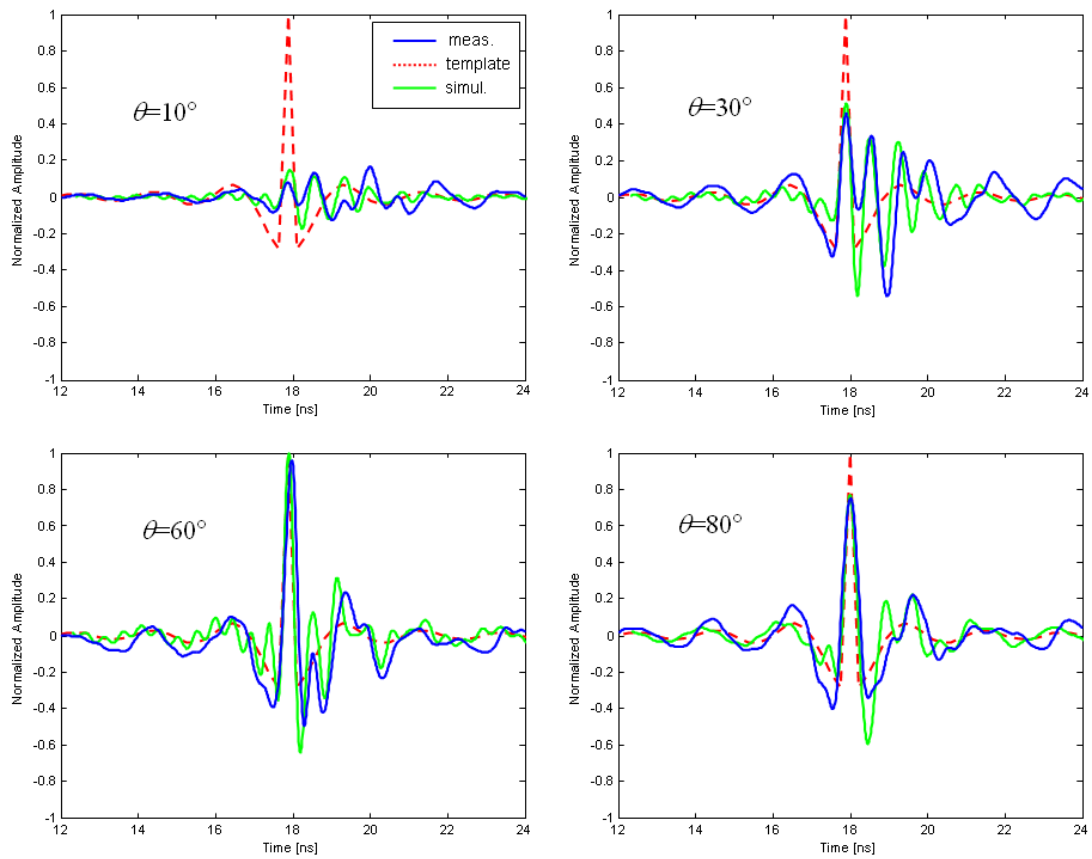


Figure 6.4: Measured pulses radiated by a 150 mm long resistively loaded monopole, shown on Figure 6.10 (blue solid line), compared with the simulated pulse (green solid line) and the source pulse (red dotted line)

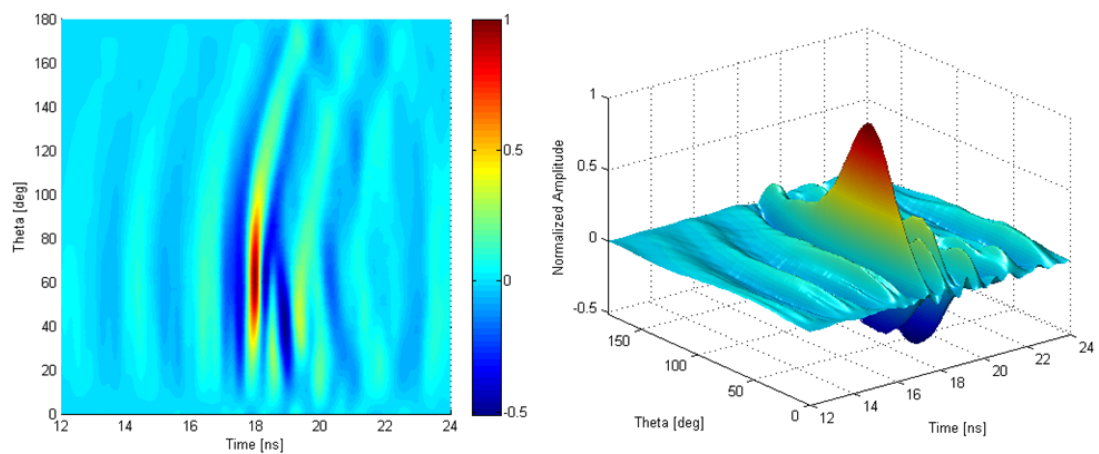


Figure 6.5: The 3D representation of the measured pulses, radiated by the 150 mm long resistively loaded monopole, shown on Figure 6.2

The measurement of radiation efficiency: The radiation efficiency was measured using the Johnston-Geissler method extended to UWB frequency range, such as explained in the Chapter 4. Due to the physical size of the antenna (150 mm), a longer Wheeler cap was fabricated, concatenating two metallic cans. The cap shown on Figure 6.6 has a 73 mm diameter and 187 mm length. The resonant modes of such a cylindrical



Figure 6.6: Metallic can (diameter=73mm, length=187 mm) used as a Wheeler cap for J-G radiation efficiency measurement of the 150mm long resistively loaded antenna

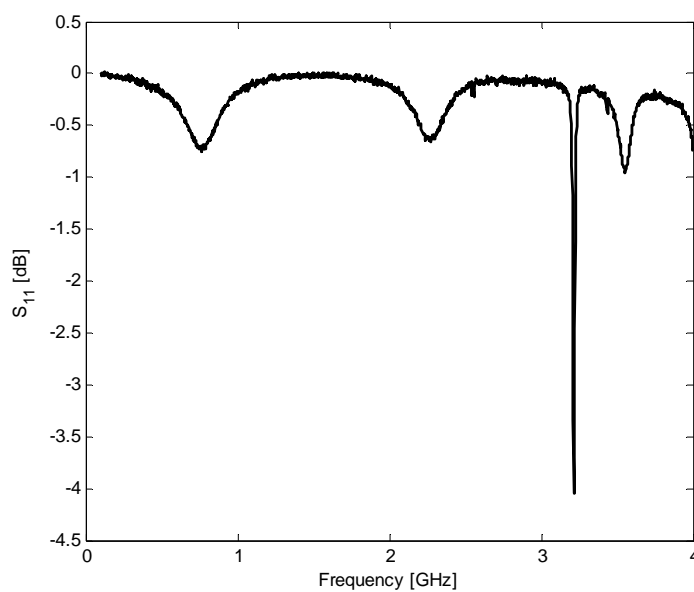


Figure 6.7: Identification of resonant modes of the Wheeler cap used for radiation efficiency measurement.

cavity were verified previously (see Figure 6.7), using a non-loaded copper wire monopole. Considering the cap resonant modes filtering properties of the radiation efficiency measurement method exposed in the Chapter 4, such a resonant cap should be convenient for the measurement purposes within the frequency range from 0.5GHz to 2.1 GHz.

The measured reflection coefficient at the resistively loaded monopole input port with respect to 50Ω , in free space and within the Wheeler cap is shown on Figure 6.8. The resistively loaded antenna shows a resonant behavior at 1.35 GHz. The measured S_{11} of the antenna within the cap shows a minimum around the same frequency.

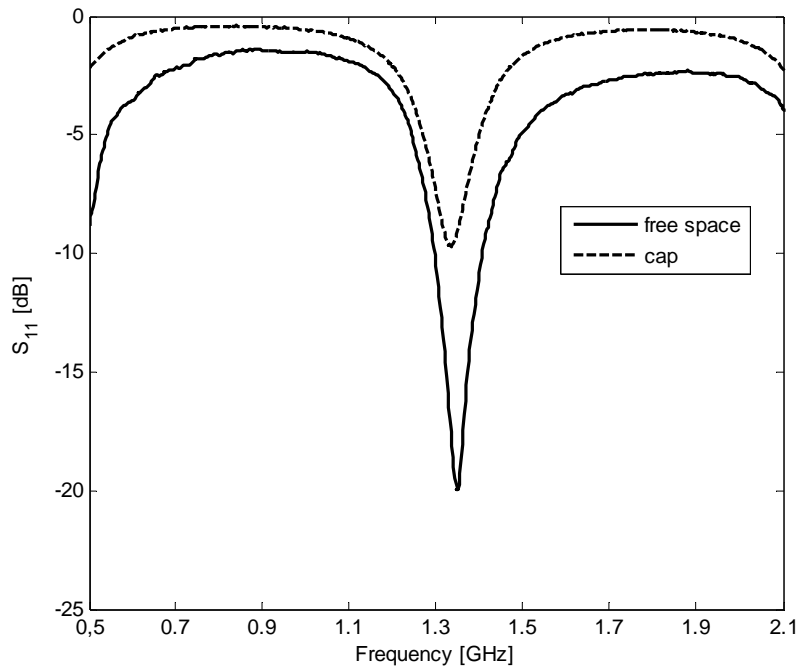


Figure 6.8: Measured reflection coefficient S_{11} of the resistively loaded monopole with respect to 50Ω in free space (solid line) and within the Wheeler cap (dashed line).

The radiation efficiency was measured over the frequency band (0.5-2.1) GHz and scaled to the range 2.5 GHz to 10.5 GHz for easier comparison with the 2 simulated monopoles: 1) original 30 mm long resistively loaded wire of 0.8mm radius obtained as PSO result in section 5.3, using NEC simulator, 2) scaled 150 mm monopole simulated using CST Microwave Studio®, that allows the exact reproduction of the physical shape of the monopole from Figure 6.2). The general trend of the measured efficiency shown in Figure 6.9 agrees with the simulated efficiency. However, the measured radiation efficiency attains slightly lower values than the simulated one.

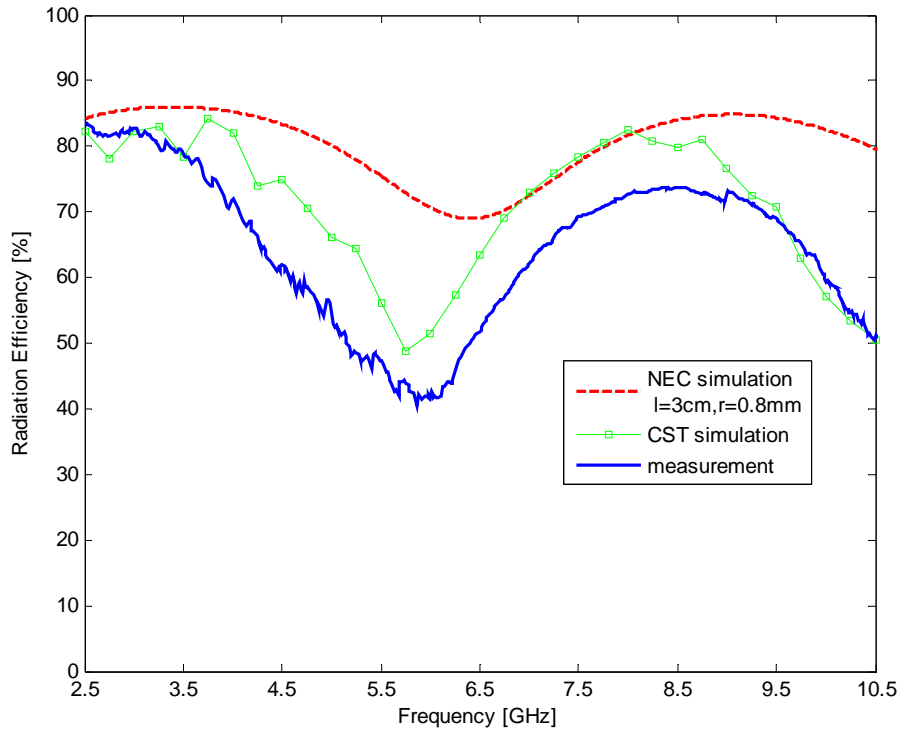


Figure 6.9: Radiation efficiency of the resistively loaded scaled monopole: original 30 mm long wire PSO-result efficiency (red dashed line), scaled 150 mm long monopole CST simulated efficiency (green squared line), measured efficiency (continuous blue line).

The differences between measured and simulated efficiency figures are certainly due to the fabrication process imperfections such as bulky soldering points and probably also to the imperfections of the radiation efficiency measurement method. The measured mean radiation efficiency (0.65) is in acceptable agreement with the mean CST simulated radiation efficiency (0.71).

The measured input impedance Z_{in} of the resistively loaded monopole is shown on Figure 6.10 compared to the simulated input impedance. The real and imaginary parts of Z_{in} are in a very good agreement. The small discrepancies in Z_{in} values that could be assigned to the fabrication process (soldering of discrete components and the lossy substrate used as a support) partially confirms the difference between measured and simulated efficiency performance.

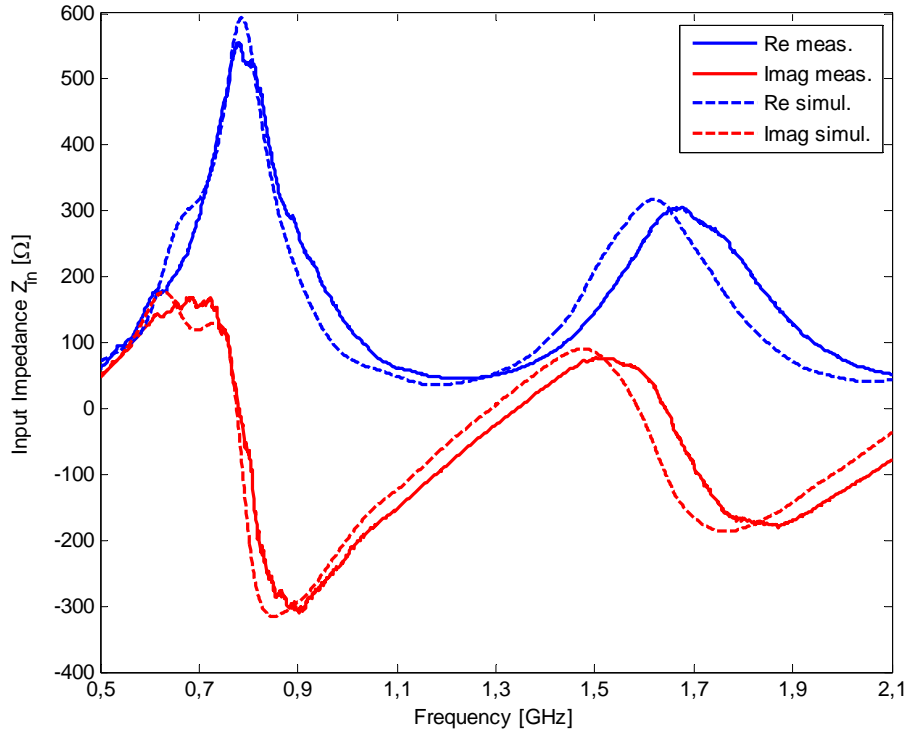


Figure 6.10: Measured and simulated (CST) input impedance of the resistively loaded geometrically scaled monopole.

In summary, the discrepancies between the measured and simulated performances are most likely due to the fabrication process and probably also to the imperfections of the radiation efficiency measurement method. Nevertheless it can be concluded that the measured resistively loaded monopole performance in terms of average fidelity SAF_l as well as in terms of radiation efficiency is satisfactory, despite of differences with the simulated performance. The concept of resistively loaded linear wire monopole design in terms of average fidelity and radiation efficiency was demonstrated.

6.2 Scaled Capacitively Loaded Monopole

6.2.1 Fabrication process

The objective was to build and measure the optimum monopole from the section 5.4.2 loaded with the capacitive profile from Table 5.5. Its performance is ($SAF_l=0.57, E_{refl}=0.3$). Similarly to the case of the resistively loaded monopole, the capacitively loaded monopole was scaled to a lower frequency range in order to avoid the parasitics effects in the measurement. The scaling factor of 5 was applied, as in the

previous case. It is important to mention here that contrary to resistances, capacitances have to be scaled as shown in the Table 6.1. Consequently the scaled monopole (length=150 mm) was loaded with new capacitance values, 5 times bigger than the values from the Table 5.5. The scaled capacitance values selected from a commercially available capacitor kit are shown in the Table 6.4.

Table 6.4: The capacitive profile of the 150 mm, scaled monopole, using commercially available capacitor values.

Segment	1	2	3	4	5	6	7	8	9	10	11	12	13	14	15	16	17
C [pF]	820	270	180	120	82	68	56	56	47	39	33	33	27	27	27	22	22

The fabricated capacitively loaded monopole is shown on Figure 6.11. The monopole structure is made of a piece of ROGERS 4003 substrate ($\epsilon_r=3.38$) of thickness 0.508 mm used as the support. The ceramic capacitors from the *muRata* GRM18-KIT-B design kit were soldered on copper pads such as schematically illustrated on Figure 6.1.



Figure 6.11: Capacitively loaded monopole optimized in the section 5.4, scaled to the frequency band 0.5 GHz-2.1 GHz

Originally the monopole from section 5.4 was simulated as a thin wire of cylindrical shape with 0.8 mm radius. For the same reasons as in the case of the resistively loaded monopole, the width of the monopole was arbitrarily set, in this case to 3 mm. Such a narrow strip tends to minimize the coupling effects between the copper pads on which the capacitors are soldered. The influence of such width adjustment on scaled monopole performance in terms of average fidelity and reflected energy is demonstrated by simulated results shown in Table 6.5. It is important to note that setting the antenna width to 3 mm will change the value of average fidelity to $SAF_I=0.46$ but also increased the amount of reflected energy to 0.52.

Table 6.5: The influence of the scaling on simulated, capacitively loaded monopole performance

length [mm]	30	150	150
wire radius [mm]	0.8	4	0.75
equivalent strip width [mm]	3.2	16	3
SAF_I	0.56	0.61	0.46
E_{refl}	0.3	0.3	0.52

6.2.2 Measurement of Capacitively Loaded Monopole

The measurements were performed in the frequency range (0.5-2.1) GHz.

The measurement of SAF_I : The measurement was performed in exactly the same manner as in the case of the resistively loaded monopole in the section 6.2.2. The measured value of SAF_I is 0.47, which is in a very good agreement with the simulated value (0.46) from Table 6.5.

The comparison of measured radiated pulses with the template and simulated pulses for three angular directions ($\theta=10^\circ$, 30° , 60° and 80°), is shown on Figure 6.12. The agreement between the measured and simulated pulses is very good especially because of the position of the main pulse peaks. The ripple that appears on the measured pulse after 20 ns can probably be attributed to the coupling on the gaps where the discrete capacitors are soldered. Despite of that, the measured performance in terms of average fidelity SAF_I is coherent with the simulated value. The Figure 6.13 gives an overall idea of the measured radiated pulses through all angular directions, up to $\theta=180^\circ$.

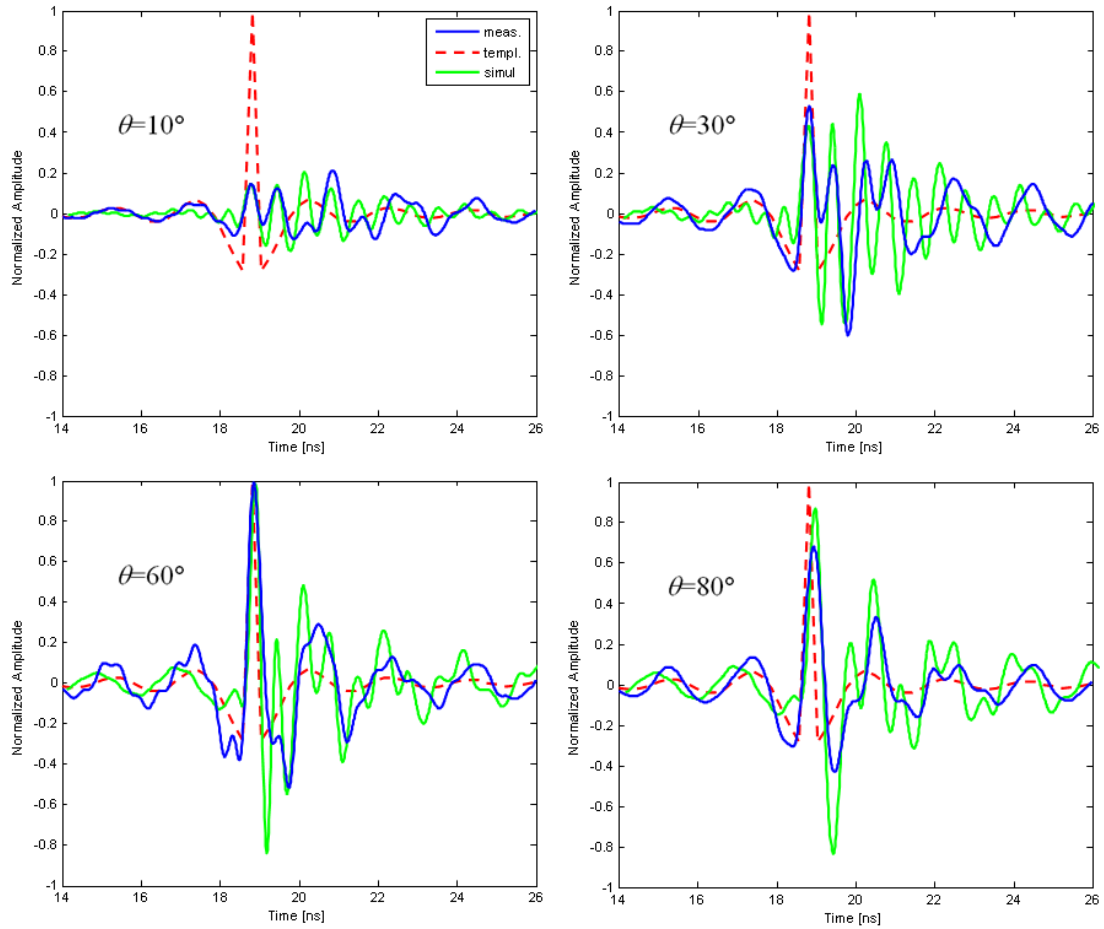


Figure 6.12: Measured pulses radiated by a 150 mm long capacitively loaded monopole, shown on Figure 6.11 (blue solid line), compared with the source pulse (red dashed line) and a simulated pulse (green solid line)

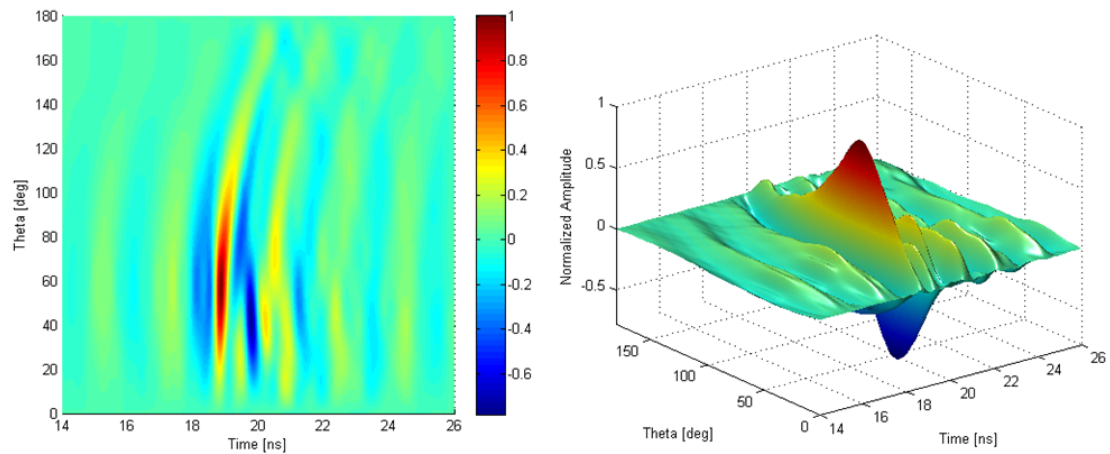


Figure 6.13: The 3D representation of the measured pulses, radiated by the 150 mm long capacitively loaded monopole, shown on Figure 6.11.

Reflected energy at the input port: The amount of reflected energy at the monopole input was computed from expression (5.10). The obtained value is $E_{refl}=0.56$, which is a very good agreement with the simulated value $E_{refl}=0.52$, shown in Table 6.5.

The comparison of the measured and simulated reflection coefficient of the scaled monopole is shown on Figure 6.14. The measured S_{11} resonance appears 800MHz below the resonance of the simulated monopole. This difference between the measured and simulated monopole is probably due to the lossy substrate used as a support.

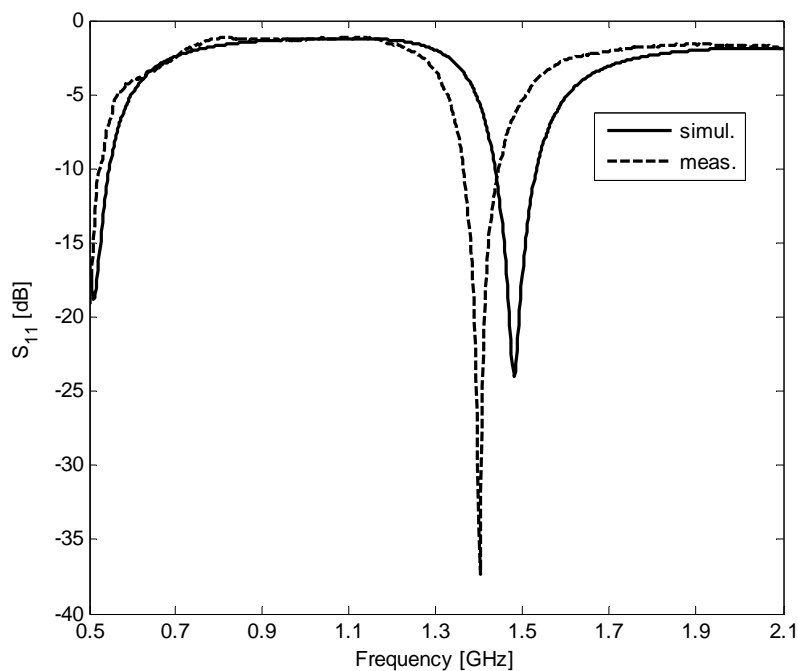


Figure 6.14: Measured and simulated reflection coefficient S_{11} of the capacitively loaded monopole with respect to 50Ω .

The real and imaginary parts of the measured (length=150 mm, width=3mm) and simulated (length=150 mm, radius=0.75 mm) monopoles, using NEC and CST are shown on Figure 6.15. Despite the small frequency shift, a relatively good agreement of input impedance values is observed through the whole operational bandwidth.

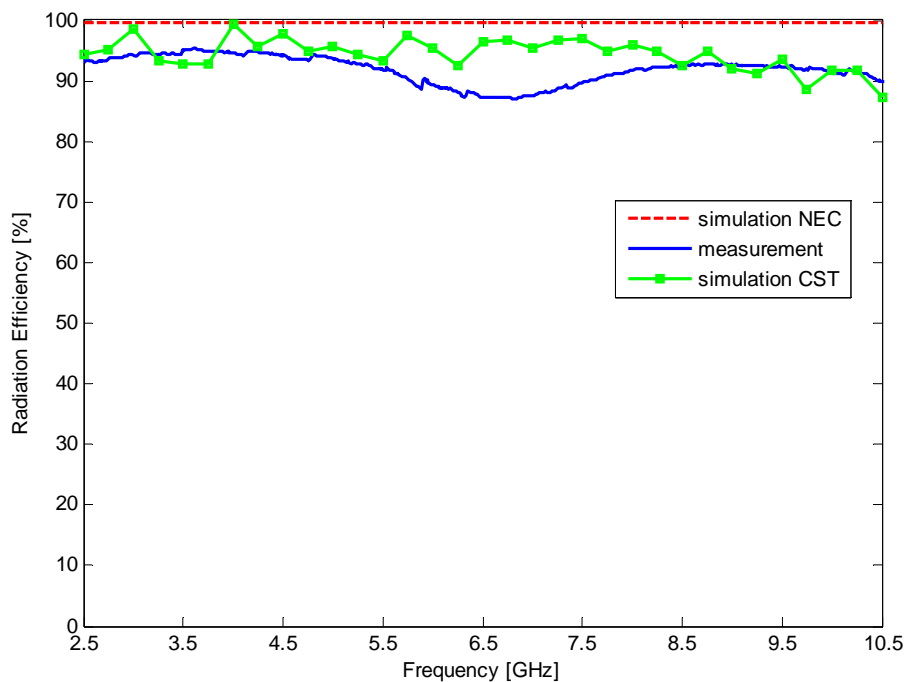


Figure 6.15: Radiation efficiency of the scaled 150mm long capacitively loaded monopole (measured: blue continuous line, NEC simulated: red dashed line, CST simulated: green squared line), scaled to the frequency range 2.5-10.5GHz

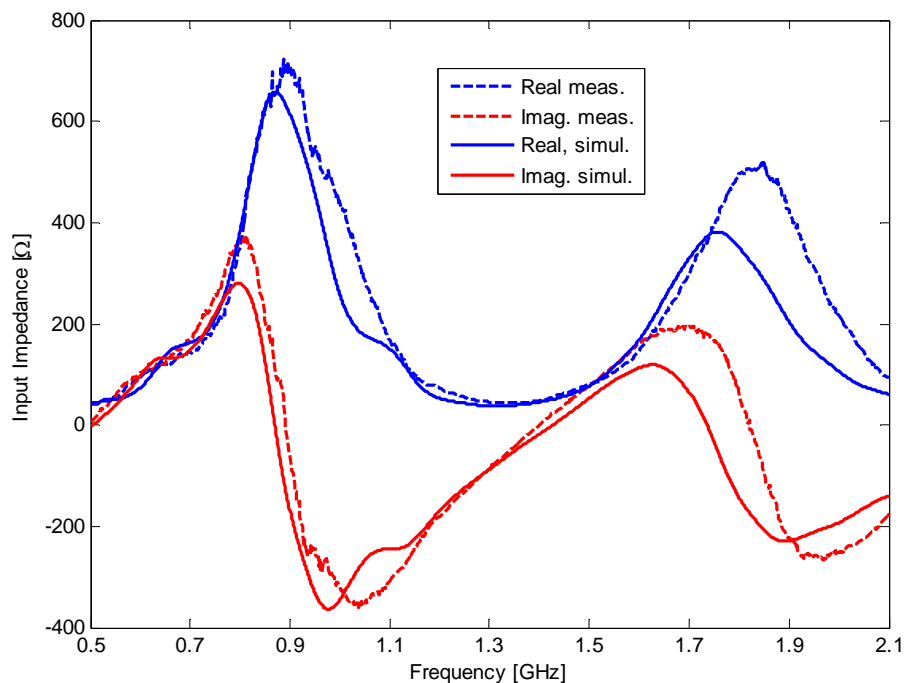


Figure 6.16: Measured and simulated (CST) input impedance of the capacitively loaded geometrically scaled monopole

In summary, the discrepancies between the measured and simulated performances are most likely due to the fabrication process. Nevertheless it can be concluded that the capacitively loaded monopole performance in terms of average fidelity SAF_l as well as in terms of input port reflected energy E_{refl} is in agreement with the simulated performance. The concept of capacitively loaded linear wire monopole design in terms of average fidelity and reflected energy was demonstrated.

6.3 Thin Metal Layer Monopole

6.3.1 Fabrication Process

As mentioned before, the main performance limiting problem of loaded antenna seems to be the parasitics of discrete components. This problem could be avoided by using resistors without the package. Such resistors can be fabricated using resistive sheets such as the one commercialized by Reinhardt Microtech [Reinhardt07]. A specific resistor value R can be computed from the physical dimensions of the piece of resistive layer (shown on Figure 6.17) from the expression 6.1, where ρ is the resistivity of the material.

$$R = \rho \cdot \frac{l}{A} \quad (6.1)$$

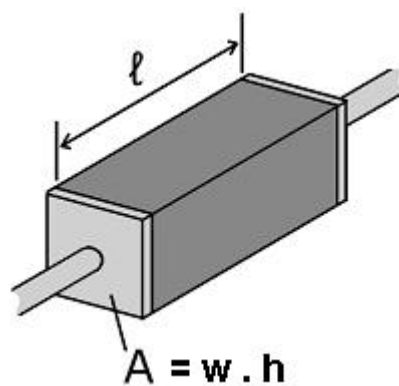


Figure 6.17: Geometry of a resistor.

In the case of thin resistive layers, the layer height h is very small and consequently the sheet resistance is given in Ω/\square (ohms/square). In the case of the 30 mm resistively loaded antenna from the section 5.3.2 a length of one segment is $l=1.76$

mm. The standard values of commercially available thin film sheet resistances are usually between $20 \Omega/\square$ and $250 \Omega/\square$. In order to fabricate the desired resistors, the corresponding widths w of the selected thin film have to be computed from the expression (6.2), where R_S is the sheet resistance.

$$w = \frac{R_S \cdot l}{R} \quad (6.2)$$

The values of the width of the optimum resistive profile from the section 5.3.2 with first 8 resistors set to 0Ω are shown in the Table 6.6.

Table 6.6: The thin film width of the resistors from the optimum resistive profile of the 30 mm optimized monopole

Segment	1	2	3	4	5	6	7	8	9	10	11	12	13	14	15	16	17
R [Ω]	0	0	0	0	0	0	0	0	1.2	1.8	2.7	3.3	4.7	5.6	6.8	8.2	10
w[mm]	-	-	-	-	-	-	-	-	29.3	19.5	13.03	10.6	7.5	6.28	5.18	4.29	3.52
$R_S=20 \Omega/\square$																	

The widths of the resistors shown in the Table 6.6 are relatively wide (segment 9 is almost 30 mm wide), and so this is not considered as the best option for fabrication. In order to obtain narrower resistors, a lower sheet resistance or much thicker resistive film is needed. Neither of these two options is commercially available. Consequently, other resistor fabrication method should be used. The solution would be to fabricate the thin resistive layers with desired parameters (resistivity, thickness, material type etc).

Thin metal layers of few nanometers can be deposited by evaporation. For this purpose a coating machine was used. This machine was made by a company Oerlikon as a turn-key solution for The Institute of Photonic Science (ICFO). It is based on Leybold Univex 350 coating system [Leybold]. Two evaporation techniques were available: a) e-beam for the heating of the carousel with up to 4 different materials, b) Joule effect (thermal evaporation) that allows the use of two different materials. The choice of the method depends on the deposited material type. The deposited thin layer thickness is controlled by a system based on a quartz crystal resonance variation. Solid state metals such as copper, aluminum, gold or silver can be heated in order to evaporate them. The metal vapor condensates on a piece of substrate, positioned few

centimeters above the heated metal. The evaporation is performed within a very high vacuum environment and very clean dustfree substrates have to be used. For this purpose, ideally a glass substrate is used. Using such a machine for thin film deposition, layers of order of nanometers can be deposited. The conductivity of the metal layer deposited on the glass substrate obviously depends on the conductivity of the evaporated metal but, it is not exactly the same due to the evaporation and condensation process. For a desired resistive profile fabrication, the conductivity and thickness of the thin deposited layer have to be accurately dimensioned, by previous measurement, in order to obtain resistors of reasonable dimensions (few millimeters).

For this purpose several materials of different conductivities, such as aluminum (Al), copper (Cu), gold (Ag), titanium (Ti) or chromium (Cr) were tested in order to estimate the variation of the conductivity due to the deposition method. Each of these metals was deposited on a glass substrate (thicknesses between 20 nm and 60 nm) and rectangles of different size were made by lithography, such as shown on Figure 6.18.

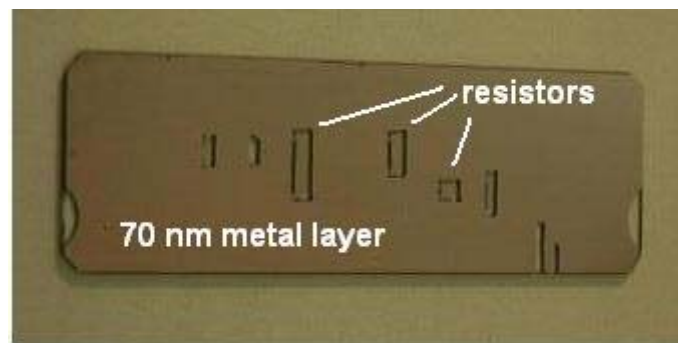


Figure 6.18: Glass board with deposited 70 nm thin metallic layer. Different rectangles emulate resistors of different values.

A multimeter and a probe station were used to measure the DC resistance R of each rectangle. The resulting conductivity σ [S/m] was estimated using expression 6.3.

$$\sigma = \frac{1}{R} \cdot \frac{l}{w \cdot h} \quad (6.3)$$

It was empirically verified that the conductivity of the material deposited by evaporation can significantly change from the original solid state conductivity value. For example, in the case of the first tested material, chromium (Cr) with solid state

conductivity $\sigma=8e^6$ S/m, the deposited chromium layer conductivity reached approximately the value of $7e^5$ S/m, which is 10 times lower.

Knowing that the deposited metal conductivity can vary as much as 10 times from its solid state value and that the layer thickness can be selected between 20 nm and 60 nm, the resistor width dimensioning was done as shown in Annex A5. An example of aluminum ($\sigma=37.8e^6$ S/m) is shown. Supposing that the deposited aluminum conductivity variation could be for example $1/10^{\text{th}}$, $1/2$ or $1/20^{\text{th}}$ of the solid state aluminum conductivity, that means $3.8e^6$ S/m, $1.9e^7$ S/m and $1.9e^5$ S/m, the width of each resistor was computed for three different layer thicknesses $h=60$; 40 or 20 nm.

Finally the deposited aluminum gave the conductivity of approximately $\sigma=19e^6$ S/m, and a layer of 40 nm thickness was chose as the best option, regarding the resistor widths, to realize the desired resistive profile (Table 6.6).

As mentioned before, the monopole has two sections: first section of first 8 segments (length 14.3 mm) without loading realized by a good conductor such as gold or silver, second section (length 15.7 mm) of the remaining 9 segments following the resistive profile made of 40 nm thick aluminum layer. The layout of such a monopole realized by thin layer deposition is shown on Figure 6.19.

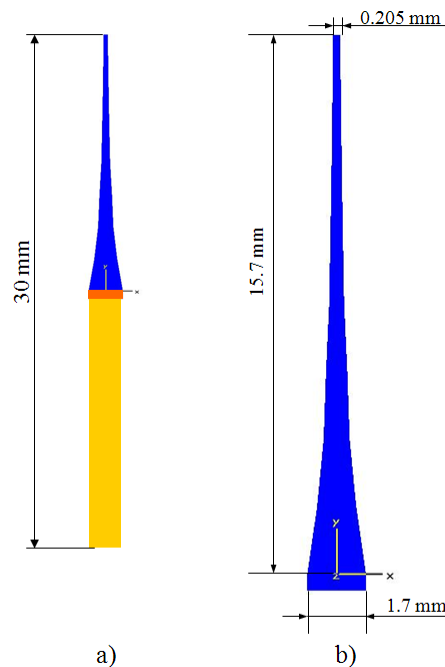


Figure 6.19: Schematic layout detail of the resistively loaded monopole fabricated by thin layer deposition on glass substrate. a) monopole with conductive section made of 40 nm gold layer (yellow), overlapping contact section of 0,5 mm (orange), resistive section (blue), b) detail of the resistive section made of 40 nm aluminum layer

In order to assure a good contact between the first (conductive) and the second (resistive) section a 0.5 mm long overlapping section was made as shown on Figure 6.19. A total of 4 monopole prototypes were fabricated on the glass substrate as shown on Figure 6.20. During the substrate cutting one of them was damaged, so only three of them were mounted on a ground plane as shown on Figure 6.21.

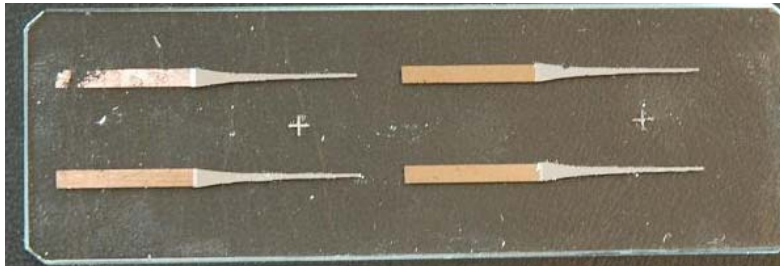


Figure 6.20: Glass substrate with 4 resistively loaded monopoles before cutting.



Figure 6.21: The resistively loaded monopole mounted on a ground plane.

6.3.2 Measurement of the Thin Layer Resistive Monopole

Reflection coefficient and input impedance: The measured reflection coefficient and input impedance of one of the three thin layer resistively loaded 30 mm long monopoles are shown on Figure 6.22 and Figure 6.24, and compared to the simulated results.

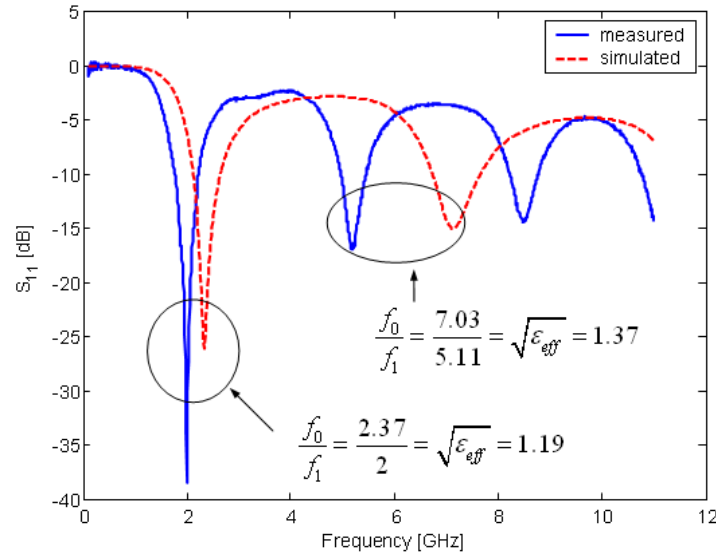


Figure 6.22: Reflection coefficient of the 30 mm long resistively loaded monopole made of thin layers on glass substrate (measurement with and simulation without glass substrate)

A frequency compression of S_{11} with respect to the measurement can be observed on Figure 6.22. This difference between the measurement and the simulation is most likely due to the glass substrate (measured permittivity approx. $\epsilon_r=5.6$), which couldn't be considered in the simulation using NEC, the fact that was confirmed by the measurement (shown on Figure 6.23) and the simulation of a resonant 30 mm long copper monopole, with and without the glass substrate. The frequency compression factor due to the glass substrate has almost the same value for both cases Figure 6.22 and Figure 6.23.

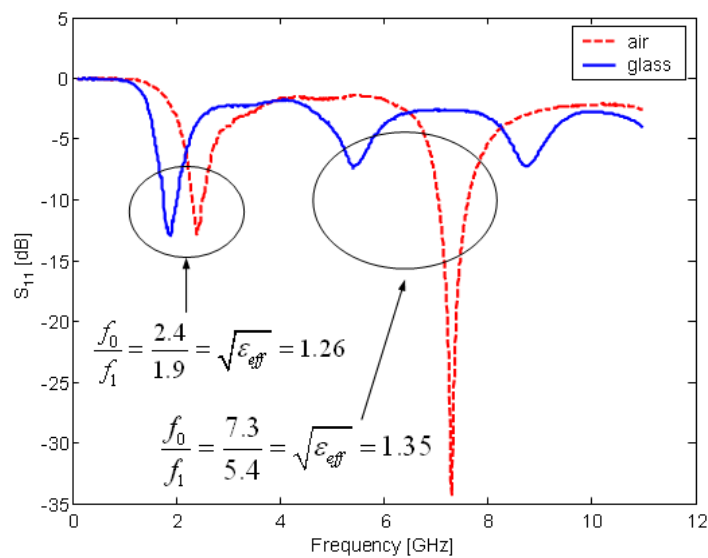


Figure 6.23: Reflection coefficient of the 30 mm long copper wire monopole on glass substrate (blue continuous line) and air substrate (red dashed line).

The glass substrate certainly affects the input impedance values as is shown on Figure 6.24 (measurement with and simulation without glass substrate). Important discrepancies between simulation and measurement are seen especially at higher frequencies. Thus, the main difference between the measurement and the simulation is certainly due to the presence of glass substrate, but a minor contribution of a fabrication process which requires a very high precision cannot be completely excluded.

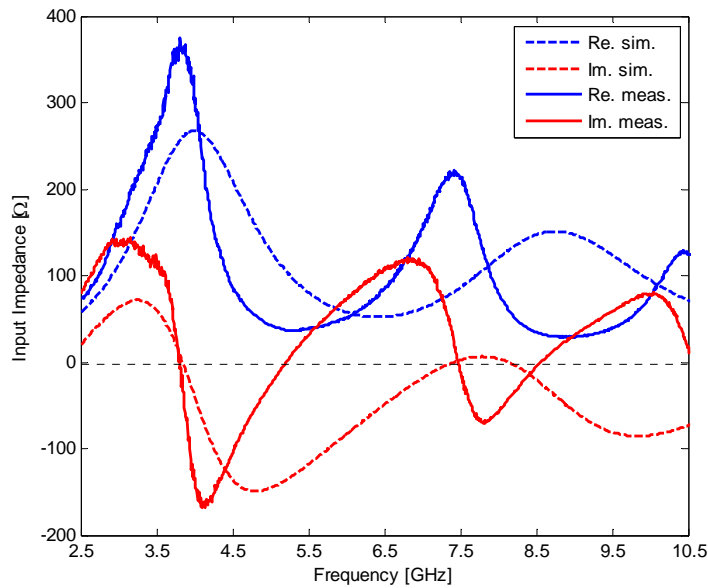


Figure 6.24: Input impedance of the 30 mm long resistively loaded monopole made of thin layers on glass substrate.

Radiation Efficiency: The radiation efficiency was measured using the J-G measurement method described in the Chapter 4. The aluminum tube shown on Figure 2.3 was used as a cap. The measured radiation efficiency in the range of 0-1 is shown on Figure 6.25. From the first sight it is evident that the measured radiation efficiency does not agree with the simulated value. The low efficiency values are most likely due to the fabrication process where the deposited material thickness or conductivity require high precision.

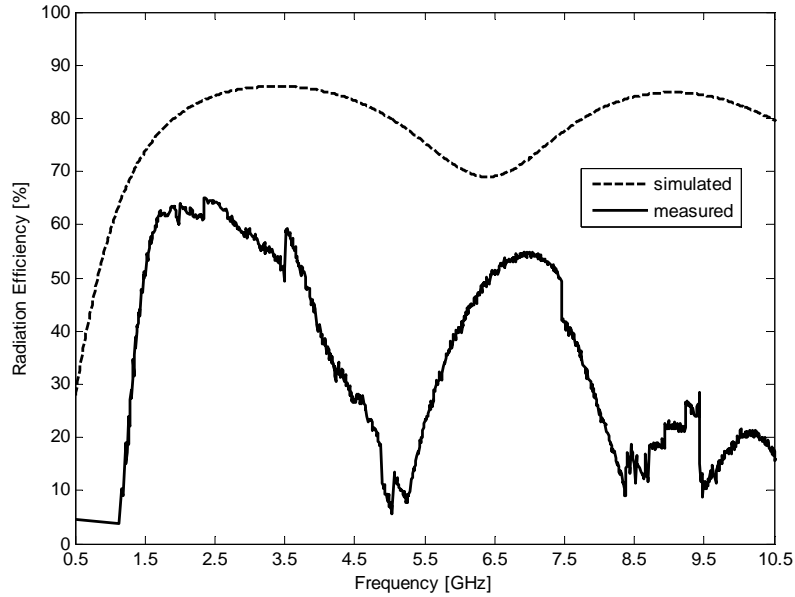


Figure 6.25: Measured radiation efficiency of the thin layer resistively loaded monopole compared to the simulation.

Fidelity SAF_I measurement: Due to the frequency compression shown on Figure 6.22, which is approximately 1.2 (it vary from 1.19 to 1.37 over the frequency range) the fidelity SAF_I originally simulated in the range 2.5 GHz – 10.5 GHz should probably be measured in a 1.2 times compressed range, approximately from 2 GHz to 8.7 GHz. The value of the measured fidelity corresponding to this frequency range is $SAF_I = 0.55$, which is 0.14 difference with the fidelity of the simulated antenna ($SAF_I=0.69$). As the frequency compression factor originated by the glass substrate is not constant over the operational bandwidth, it is not possible to compute the fidelity value with enough precision and objectively make a comparison with the simulation.

The pulses radiated by the 30 mm long resistively loaded monopole on glass substrate and oriented along z-axis, are shown on Figure 6.26 and Figure 6.27. On Figure 6.26 the radiated pulses (blue solid line) are compared with simulated pulses (green solid line) and with the template pulse (red dashed line) used for SAF_I computation. A relatively good agreement between the simulated and measured pulse shapes is consistent with the SAF_I performance. Moreover, the pulses match relatively well the template shape especially at $\theta=30^\circ$, 60° and 80° .

The Figure 6.27 gives an overall idea of the measured radiated pulses through all angular directions, up to $\theta=180^\circ$. It is important to remain that the average fidelity

SAF_I was computed in angular range from $\theta=0^\circ$ to $\theta=90^\circ$, corresponding to the space above the ground plane. Despite of the stable position of the main peak between $\theta=10^\circ$ and $\theta=90^\circ$, observed on Figure 6.27, as explained previously, the obtained SAF_I performance is lower than expected from simulation.

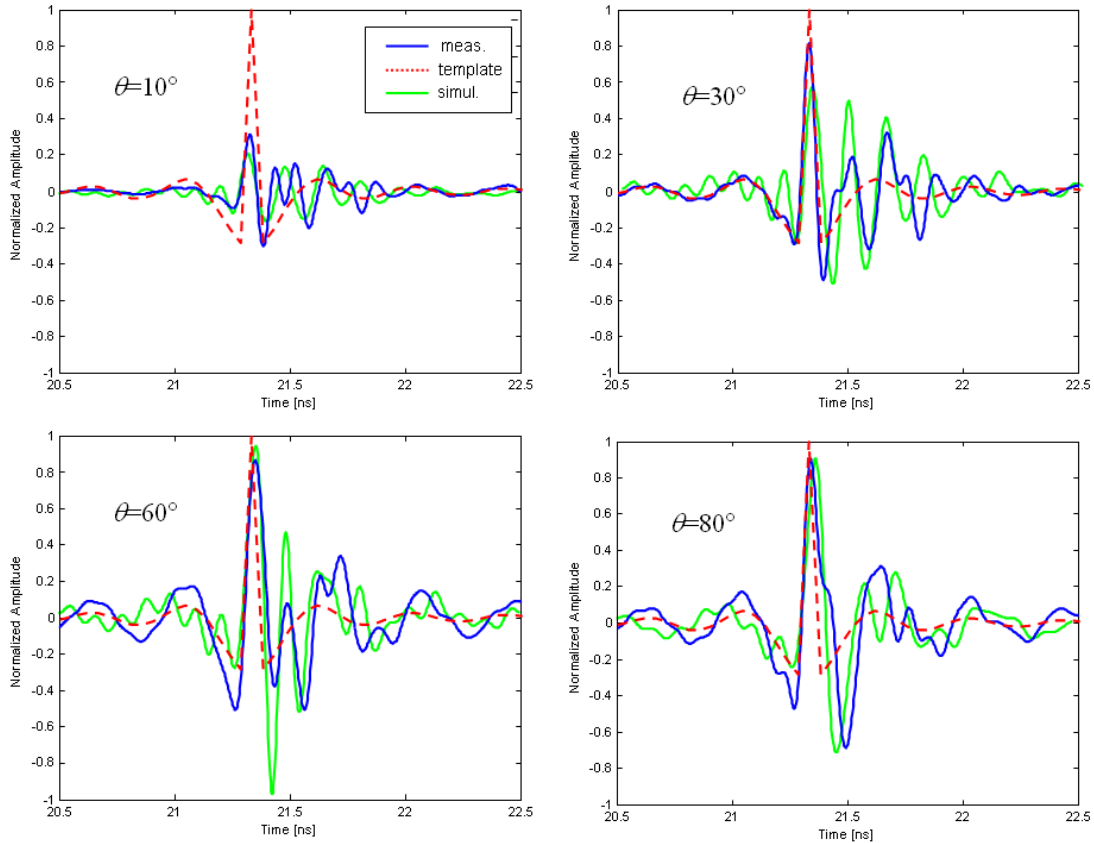


Figure 6.26: Measured pulses radiated by a 30 mm long resistively loaded monopole, shown on Figure 6.5 (blue solid line), compared with the simulated pulse (green solid line) and the source pulse (red dashed line) used as template.

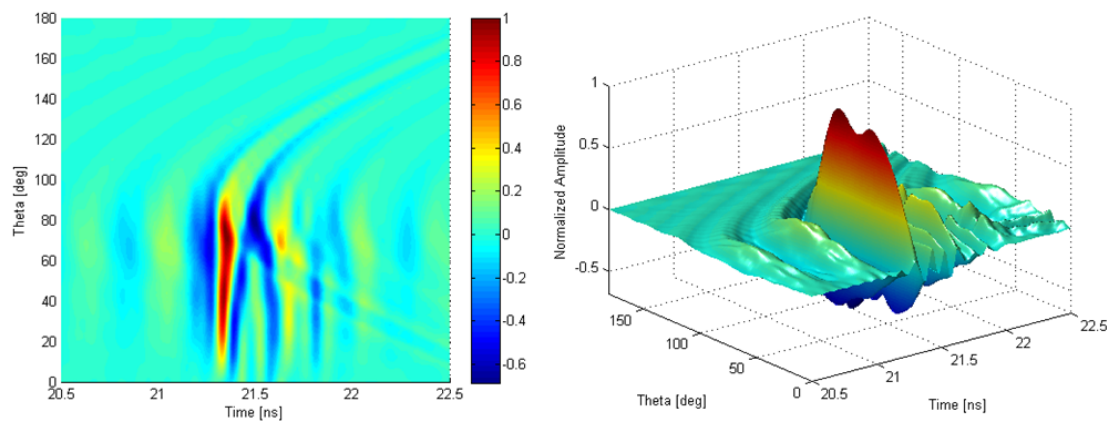


Figure 6.27: 3D representation of the measured pulses, radiated by the 30 mm long resistively loaded monopole, shown on Figure 6.20.

Finally, due to several fabrication constraints such as the high requirements on fabrication accuracy, the need of a glass substrate of the ineffective control of the thin metallic layer conductivity, the fabricated antenna does not reach the performance in terms of spatially averaged fidelity and radiation efficiency established by simulation.

6.4 Conclusions

The objective of this chapter was to prove the concept of UWB resistively loaded monopole design in terms of average fidelity SAF_l , radiation efficiency and reflected energy at the input, through the fabrication and measurement of optimized monopoles. The main limitation that was identified prior to the fabrication was the parasitics influence.

The first approach to this problem was to fabricate scaled monopoles using discrete components. The scaled monopoles are only models so their size is bigger and operational frequency band is lower than the originally intended. However, the concept of UWB monopole design in terms of proposed parameters was proved on such monopoles.

The second approach was to use components without package. A resistively loaded antenna using thin metallic layers was fabricated and its performance measured. The comparison of the measured performance with the simulation revealed important discrepancies, mainly attributed to the fabrication process and the use of glass substrate. The fabrication method didn't provide an effective control of the metallic layer conductivity. Due to this limitation the resistively loaded monopole fabricated with thin metallic layers didn't fulfill the expected performance requirements. In order to fabricate the resistively loaded monopole with thin metallic layers more rigorous and precise fabrication conditions would be necessary.

CONCLUSIONS

7. CONCLUSIONS AND RESEARCH PERSPECTIVE

This dissertation has dealt with UWB antenna performance assessment, alone and within a transmitter-receiver system. Particular emphasis was placed on UWB antenna design and characterization for optimum communication system performance. Especially the transmitted and received UWB pulses distortion needed to be characterized. For this purpose various antenna descriptors were analyzed and due to the dispersion properties of UWB antennas the need of new UWB descriptors was identified as a first objective of the thesis. Consequently, three new figures of merit evaluating the antenna performance within the UWB system have been presented in Chapter 3. Namely, spatially averaged fidelities SAF_1 and SAF_2 and averaged energy efficiency AE . SAF_1 and SAF_2 parameters summarize the distortion introduced by the single antenna or by the tx-rx system formed by 2 antennas respectively, in a single direction-independent number. It has been shown that all these new figures of merit (SAF_1 , SAF_2 and AE) depend on both the feeding pulse and template shapes. Moreover, using SAF_2 and AE , it was demonstrated how antenna losses could improve the bandwidth of an UWB system.

The next objective of the thesis was the fabrication and measurement of the antenna optimized in terms of the new previously defined figures of merit, and so to prove their relevancy for antenna design. For this purpose, the measurement procedures of the new descriptors were analyzed first, in Chapter 4. For the correct measurement of the spatially averaged fidelity SAF_1 a simple method for calibrating the anechoic chamber in a wide frequency range was detailed. Analyzing the SAF_1 measurement issues it was concluded that the comparison of antennas in terms of SAF_1 should always be realized in the same conditions of feeding, template pulse shapes and sampling rate. Some of these parameters should be known *a priori* for a given application. Moreover a radiation efficiency measurement method based on the Wheeler cap principle and improved by Johnston and Geissler, was enhanced to allow its use in a very wide frequency range. The enhanced measurement principle was experimentally assessed on several antennas over the UWB frequency range. The

simplicity of implementation inherited from the original Wheeler cap method as well as the independence from the antenna loss mechanism circuit model proved by Johnston, makes this enhanced method very practical for the measurement of UWB antennas.

A practical use of UWB antenna descriptors was demonstrated through an optimization of resistively and capacitively loaded monopoles in terms of spatially averaged fidelity SAF_1 , mean radiation efficiency and energy reflected at antenna input port. To that effect an evolutionary optimization technique (PSO) was used. Moreover, since our objective was the monopole fabrication and experimental performance assessment, the influence of parasitic behavior and tolerance of discrete components on monopole performance was analyzed. It was concluded that due to the strong influence of parasitics on antenna performance a parasitics-free loaded monopole fabrication method is needed. Consequently two approaches were adopted.

Firstly, the resistively and capacitively loaded monopoles using discrete components were scaled to a frequency range 5-times lower than the frequency range used originally in simulations, expecting lower parasitics influence. The measured performance of scaled monopoles is in good agreement with the simulated performance and so proves the concept of UWB antenna design in terms of proposed parameters.

Secondly, a resistively loaded monopole using very thin metallic layers was fabricated. Unfortunately, the fabrication method didn't provide an effective control of the metallic layer conductivity and consequently of the resistive loading profile. For this reason the resistively loaded monopole didn't reach the expected performance.

In summary, new UWB antenna performance descriptors were defined and their relevancy proved through design and experimental verification of loaded monopoles for optimum UWB system performance. As an output of this work, 1 book chapter, 2 journal papers and 4 international conference papers were presented.

The objectives proposed in Chapter 2 were reached, however several improvements can be proposed. In the following some research perspectives are outlined.

Multi-objective PSO optimization of impedance loaded monopole

In Chapter 5, the optimization of resistively and capacitively loaded monopoles was presented. The fitness function for performance evaluation of such monopoles was defined in terms of 2 parameters, as a weighted sum of SAF_1 and mean radiation efficiency or SAF_1 and input port reflected energy. A multi-objective PSO can be implemented defining the fitness function as a combination of more than only 2 parameters, for example spatially averaged fidelity, radiation efficiency, input port impedance, beamwidth etc.

Moreover the optimized impedance loading profile was defined as purely resistive or capacitive. In order to exploit the impedance loading performance, the loading profile could be defined by general complex impedances such as proposed by Wu [Wu65] or Montoya [Montoya96].

Further validation of enhanced (J-G) method

The measurement method proposed in Chapter 4 was validated mainly on monopoles and for this reason a cylindrical Wheeler cavity was always used. The original work by Johnston and Geissler does not impose any limitation on antenna and resonant cavity geometries. Hence different antenna and cavity geometries can be analyzed in order to completely validate the J-G method enhancement for wide frequency ranges.

Experimental performance validation within a real UWB system

The antennas fabricated for experimental verification shown in Chapter 6, are only models so their size is bigger and the operational frequency band is lower than the originally intended. For this reason the experimental verification of the optimized antenna performance from Chapter 3, in terms of SAF_2 within a real UWB system wasn't accomplished. Hence an improvement of fabrication method would be necessary.

ANNEX

A1: Acronyms

AE	Averaged Efficiency
CAD	Computer Aided Design
DC	Direct Current
FCC	Federal Communications Commission
NEC	Numerical Electromagnetics Code
PSO	Particle Swarm Optimization
RF	Radio Frequency
SAF	Spatially Averaged Fidelity
SMD	Surface Mounted device
SNR	Signal to Noise Ratio
tx-rx	transmitter-receiver
UWB	Ultra Wide Band

A2: T-network of 3dB and 6dB attenuators

The T-network shown on Figure A2.1, used to simulate the attenuators in NEC has the resistors of following values:

- a) 3dB attenuator: $R_1=8.54 \Omega$, $R_2=141.92 \Omega$
- b) 6dB attenuator: $R_1=16.61 \Omega$, $R_2=66.93 \Omega$

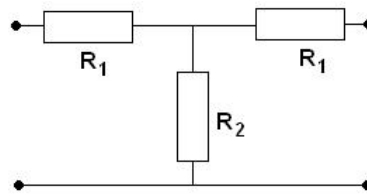


Figure A2.1: T network

A3: J-G radiation efficiency measurement properties

The J-G method showed the capacity to remove some of the inherent resonant modes of the resonant cavity using a circle fitting algorithm. Here some of the details about J-G method properties are shown on a measurement example of an 800MHz straight wire $\lambda/4$ monopole over a 60x60cm ground plane. The monopole is fed by a standard SMA coaxial connector. The wire radius is 0.28mm.

The measured reflection coefficients of such monopole in free space and enclosed within a Wheeler cap (aluminum tube $L=120mm$, $d=23mm$) are shown on Figure A3.1. In the analyzed frequency band (100MHz-11GHz), different resonances of the monopole (0.8, 2.45, 4.1, 5.8, 7.4) GHz in free space appear (blue dashed curve) as well as the first resonant mode of the cap at 7.67GHz (red continuous curve). The radiation efficiency is then computed in Matlab from these measurements. On Figure A3.2 are shown two cases of radiation efficiency obtained by J-G method: with (blue continuous curve) and without (red dashed curve) fitted circumference in $\Delta_{S,\min}$ and $\Delta_{S,\max}$ coefficients computing. The difference between the two cases is evident especially between 7-8 GHz. If the circumference fitted to measured data is not used, the efficiency figures fall into very low values, down to 10%, whereas if it is used the efficiency reaches 95%.

First the case when the coefficients $\Delta_{S,\min}$ and $\Delta_{S,\max}$ are computed over a perfect circumference is shown on Figure A3.3 explaining the computation mechanism. On the left, Figure A3.3.a) shows the $S_{11,cap}$ measured data (red dots) and a free space measurement point $S_{11,fs}$ (green cross) at 7.66GHz, so exactly within the band that shows the biggest difference in Figure A3.2. The coefficients $\Delta_{S,\min}$ and $\Delta_{S,\max}$ used to compute the J-G efficiency, are the minimum and maximum distances of the particular measured point $S_{11,fs}$ at frequency f_N (here 7.66GHz) to the circle formed by the $S_{11,cap}$ data in the vicinity of the frequency f_N . The $S_{11,cap}$ data does not form a perfect circumference (red dots), especially at higher frequencies, due to resonant modes of the cap. There is one $S_{11,cap}$ point (red dot) very close to $S_{11,fs}$ point (green cross). This point corresponds to the cap resonant mode at 7.67GH, shown also at Figure A3.2. When a circumference is fitted to $S_{11,cap}$ data (blue dots on Figure

A3.3a), most of these resonances are filtered. Finally $\Delta_{S,\min}$ and $\Delta_{S,\max}$ are computed as minimum and maximum distances from $S_{11,fs}$ to the fitted circle.

Now, if the $S_{11,cap}$ data is used directly for $\Delta_{S,\min}$ and $\Delta_{S,\max}$ computation, without the fitted circle, the cap resonant modes will strongly influence the measurement result. The resonant mode at 7.67GHz will be the point that gives the minimum distance to several $S_{11,fs}$ points, and so will be used for $\Delta_{S,\min}$ computation in the vicinity of this frequency. This is shown on Figure A3.3b). As the J-G radiation efficiency is proportional to $\Delta_{S,\min}$ and $\Delta_{S,\max}$, a smaller value of $\Delta_{S,\min}$ will result in a very small efficiency value, $\Delta_{S,\max}$ being almost the same in both cases a) and b). This explains the efficiency notch in the case of not using the circle fitting (red dotted curve) shown on Figure A3.2.

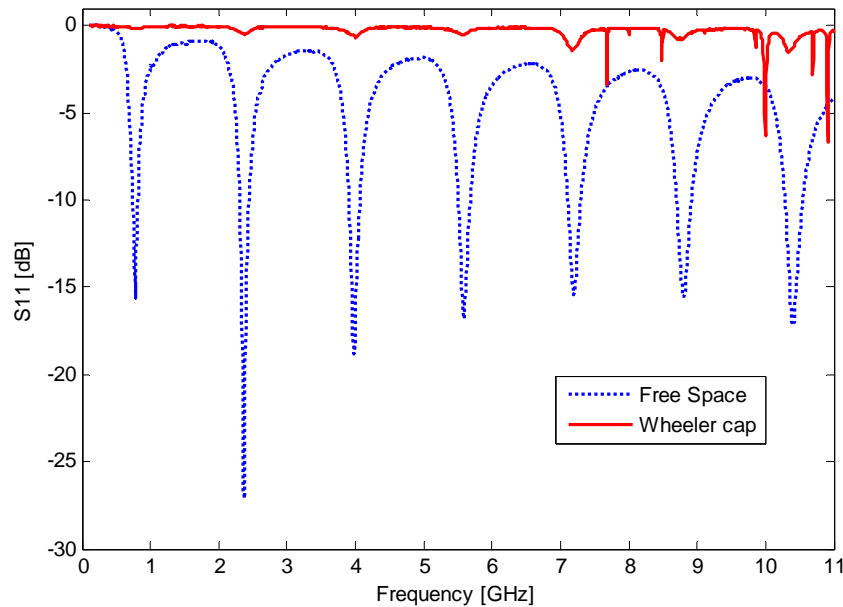


Figure A3.1: Measured reflection coefficients of 800MHz wire monopole in free space and within Wheeler cap.

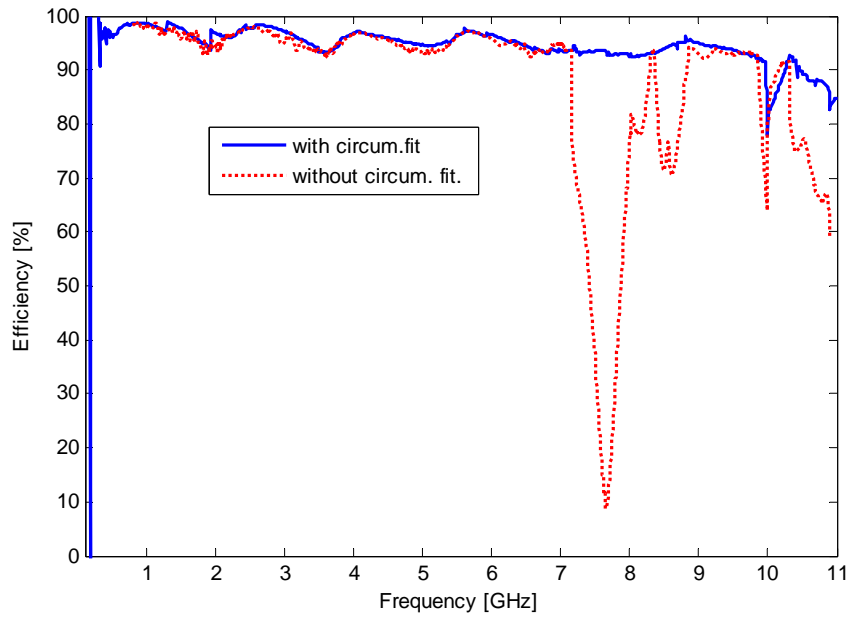


Figure A3.2: Radiation efficiency of the 800MHz wire monopole measured using J-G method, with (blue continuous line) and without (red dashed line) the fitted circumference.

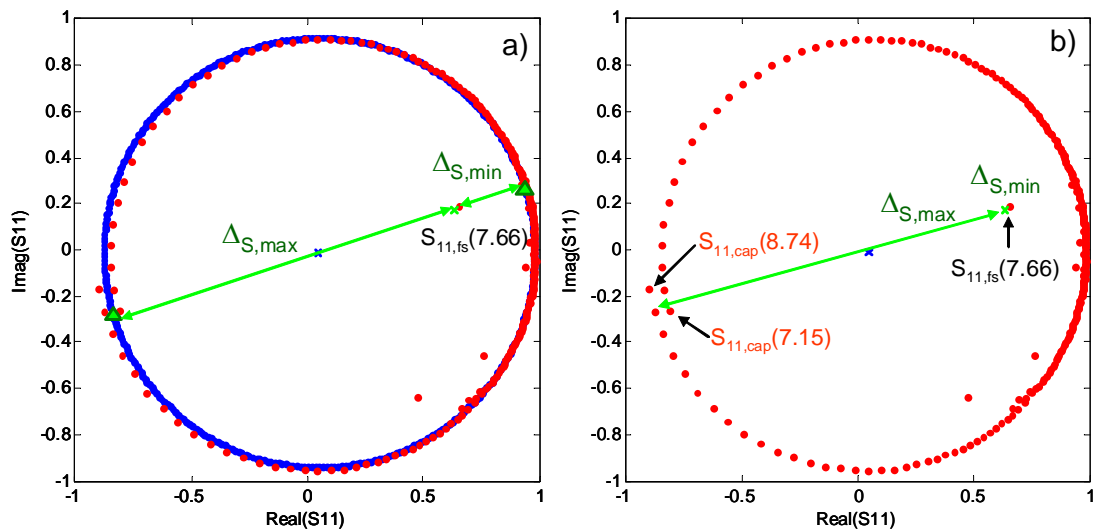


Figure A3.3: Computing of $\Delta_{S,\min}$ and $\Delta_{S,\max}$ using a complete $S_{11,\text{cap}}$ measured circumference at 7.66GHz, a) with fitted circumference, b) without fitted circumference.

A5: Dimensioning the resistors widths

		(1/10), $3.8e^6$ S/m $w[mm]$			(1/2), $1.9e^7$ S/m $w[mm]$			(1/20), $1.9e^5$ S/m $w[mm]$		
N	R [Ω]	h=60nm	h=40nm	h=20nm	h=60nm	h=40nm	h=20nm	h=60nm	h=40nm	h=20nm
1	0.68	11.352	17.028	34.056	2.2704	3.4056	6.8111	227.04	340.56	681.11
2	0.33	23.392	35.088	70.175	4.6784	7.0175	14.035	467.84	701.75	1403.5
3	0.1	77.193	115.79	231.58	15.439	23.158	46.316	1543.9	2315.8	4631.6
4	0
5	0
6	0.15	51.462	77.193	154.39	10.292	15.439	30.877	1029.2	1543.9	3087.7
7	0.39	19.793	29.69	59.379	3.9586	5.9379	11.876	395.86	593.79	1187.6
8	0.82	9.4138	14.121	28.241	1.8828	2.8241	5.6483	188.28	282.41	564.83
9	1.2	6.4327	9.6491	19.298	1.2865	1.9298	3.8596	128.65	192.98	385.96
10	1.8	4.2885	6.4327	12.865	0.8577	1.2865	2.5731	85.77	128.65	257.31
11	2.7	2.859	4.2885	8.577	0.5718	0.8577	1.7154	57.18	85.77	171.54
12	3.3	2.3392	3.5088	7.0175	0.46784	0.70175	1.4035	46.784	70.175	140.35
13	4.7	1.6424	2.4636	4.9272	0.32848	0.49272	0.98544	32.848	49.272	98.544
14	5.6	1.3784	2.0677	4.1353	0.27569	0.41353	0.82707	27.569	41.353	82.707
15	6.8	1.1352	1.7028	3.4056	0.22704	0.34056	0.68111	22.704	34.056	68.111
16	8.2	0.94138	1.4121	2.8241	0.18828	0.28241	0.56483	18.828	28.241	56.483
17	10	0.77193	1.1579	2.3158	0.15439	0.23158	0.46316	15.439	23.158	46.316

REFERENCES

- [Altshuler61] E. E. Altshuler, "The travelling-wave linear antenna", *IRE Trans. Antennas. Propag.*, vol AP-9, July 1961
- [Ashkenazy85] J. Ashkenazy, E. Levine, D. Treves, "Radiometric measurement of antenna efficiency," *Electron. Lett.*, vol.21, no.3, pp.111-112, Jan. 1985.
- [Balanis97] C. A. Balanis, *Antenna Theory Analysis and Design*, Second edition, Wiley, 1997
- [Barnes00] M. A. Barnes, *Ultra-Wideband Magnetic Antenna*, US Patent 6,091,374, July 18, 2000
- [Bates72] R. Bates, G. Burrell, "Towards faithful radio transmission of very wide bandwidth signals," *IEEE Trans. Ant. & Prop.*, vol.20, no.6, pp. 684-690, Nov. 1972
- [Burke81] G. J. Burke, A. J. Poggio, *Numerical Electromagnetics Code (NEC) - Method of Moments*, Rep. UCID18834, Lawrence Livermore Lab. Livermore, CA, 1981.
- [Cardama98] A. Cardama et al., *Antennas*, Primera edición, Edicions UPC, 1998
- [Carlisle01] A. Carlisle, G. Dozier, "An off-the-shelf PSO," in Proc. Workshop ParticleSwarm Optimization, Indianapolis, IN, 2001
- [Carter39] P. S. Carter, *Short Wave Antenna*, US Patent 2,175,252, October 10, 1939
- [Chen02] X. Chen; S. Kiaei, "Monocycle shapes for ultra wideband system," *IEEE International Symposium on Circuits and Systems, 2002. ISCAS 2002.*, vol.1, pp. 597-600, 2002

- [Com07] Commission of the European Communities, "Commission Decision of 21/II/2007 on allowing the use of the radio spectrum for equipment using ultra-wideband technology in a harmonized manner in the Community," Brussels, 21 February, 2007 (<http://eur-lex.europa.eu/LexUriServ/LexUriServ.do?uri=OJ:L:2007:055:0033:0036:EN:PDF>)
- [Conroy99] J. T. Conroy, J. L. LoCicero, D. R. Ucci, "Communication techniques using monopulse waveforms," *Proc. IEEE MILCOM*, vol.2, pp.1181-1185 vol.2, 1999
- [Dissanayake06] T. Dissanayake, K. P. Esselle, "Correlation-Based Pattern Stability Analysis and a Figure of Merit for UWB Antennas," *IEEE Trans. Antennas Propag.*, vol.54, no.11, pp.3184-3191, Nov. 2006
- [DuHamel57] R. DuHamel, D. Isbell, "Broadband logarithmically periodic antenna structures," *IRE International Convention Record*, vol.5, pp. 119-128, Mar. 1957
- [Eberhart01] R. C. Eberhart, Y. Shi, „Particle swarm optimization: developments, applications and resources,“ in *Proc. 2001 Congr. Evolutionary Computation*, vol. 1, 2001
- [Esselle90] K. P. Esselle, S. Stuchly, "Pulse-receiving characteristics of resistively loaded dipole antennas," *IEEE Trans. Antennas Propag.*, vol. 38, no. 10, pp. 1677-1683, Oct. 1990.
- [Evans99] J. A. Evans, M. J. Amunann, "Planar trapezoidal and pentagonal monopoles with impedance bandwidths in excess of 10:1," *Proc. IEEE Antennas Propag. Soc. Int. Symp.*, vol.3, pp.1558-1561, Aug. 1999
- [ETS03] ETS Lindgren "Model 3160 Pyramidal Horn Antennas manual", REV C-PN 399 185 July 2003, published at <http://www.ets-lindgren.com/manuals/3160.pdf>

- [FCC02] Federal Communications Commission (FCC), *Revision of Part 15 of the Commission's Rules Regarding Ultra-Wideband Transmission Systems*, April, 2002; <http://www.wireless.fcc.gov/rules.html>
- [Fontana00] R. J. Fontana, "A Brief History of UWB Communications", published on <http://www.ferret.com.au/n/A-brief-history-of-UWB-communications-n681131>
- [Fontana02] R. Fontana, A. Ameti, E. Richley, L. Beard, D. Guy, "Recent advances in ultra wideband communications systems," *IEEE Conference on Ultra Wideband Systems and Technologies*, pp. 129-133, 2002
- [Geissler03] M. Geissler, O. Litschke, D. Heberling, P. Waldow, I. Wolff, "An improved method for measuring the radiation efficiency of mobile devices," *Proc. IEEE Antennas Propag. Soc. Int. Symp.*, vol.4, pp. 743-746, June 2003
- [Gemio09] J. Gemio, G. Junkin, J. Parron, R. Villarino, "Resonator-Loaded Dual-Band Monopole for Universal WLAN," *IEEE Ant. & Wireless Prop. Letters*, vol.8, pp.736-739, 2009
- [Herrero08] J. L. Herrero Devroye, "Optimización mediante PSO del perfil resistivo de un monopolo cargado para aplicaciones UWB", *trabajo de fin de carrera*, EPSC-UPC, Julio 2008, advised by P. Miškovský, J.M. González-Arbesú
- [Murata09] Murata Product Catalog, "Chip Monolithic Ceramic Capacitors", CO2E-15, 29. Sept., 2009
<http://www.murata.com/products/catalog/pdf/c02e.pdf>
- [Han02] J. Han; C. Nguyen, "A new ultra-wideband, ultra-short monocycle pulse generator with reduced ringing," *IEEE Microw. Wireless Compon. Lett.*, vol.12, no.6, pp.206-208, Jun 2002

- [Johnston98] R. H. Johnston, J. G. McRory, "An improved small antenna radiation-efficiency measurement method," *IEEE Antennas Propag. Mag.*, vol.40, no.5, pp.40-48, Oct 1998.
- [Johnston03] R. H. Johnston, J. Chu, "Small antenna efficiency measurements using overmoded cavities," *Proc. IEEE Antennas Propag. Soc. Int. Symp.*, vol.4, pp. 723-726, June 2003
- [Kanda78] M. Kanda, "A relatively short cylindrical broadband antenna with tapered resistive loading for picosecond pulse measurements", *IEEE Trans. Antennas Propag.*, vol. AP-26, no. 3, pp. 439-446, May 1978.
- [Kanda83] M. Kanda, "Time domain sensors for radiated impulsive measurements," *IEEE Trans. Antennas Propag.*, vol.31, no.3, pp. 438-444, May 1983
- [Kandoian46] A. G. Kandoian, "Three new Antenna Types and Their Applications," *Proceedings of the IRE* 34, p70W, Feb 1946
- [Kennedy95] Kennedy, J.; Eberhart, R., "Particle swarm optimization," *Proc. IEEE Neural Networks Int. Conf.*, vol.4, pp.1942-1948 vol.4, Nov/Dec 1995
- [Kim05] Ki-Hak Kim; Jin-U Kim; Seong-Ook Park, "An ultrawide-band double discone antenna with the tapered cylindrical wires," *IEEE Trans. Ant. & Prop.*, vol.53, no.10, pp. 3403-3406, Oct. 2005
- [Lamensdorf94] D. Lamensdorf, L. Susman, "Baseband - Pulse antenna techniques", *IEEE Antennas Propag. Mag.*, vol. 36, no. 1, pp. 20-30, Feb.1994.
- [Lee01] J. S. Lee; C. Nguyen, "Novel low-cost ultra-wideband, ultra-short-pulse transmitter with MESFET impulse-shaping circuitry for reduced distortion and improved pulse repetition rate," *IEEE Microw. Wireless Compon. Lett.*, vol.11, no.5, pp.208-210, May 2001

- [Leybold] Leybold Univex 350 coating system, details can be found at <http://www.ibm-microtech.co.uk/equipment/leybold.php>
- [Lindeblad41] N. E. Lindeblad, April 29, 1941, *Wideband Antenna*, US Patent 2,239,724
- [Lodge98] O. Lodge, August 16, 1898, *Electric Telegraphy*, US Patent 609,154
- [Marie62] G. R-P. Marié, *Wideband Slot Antenna*, US Patent 3,031,665, April 24, 1962
- [MathWorks] <http://www.mathworks.com/>
- [Miao06] Meng Miao, C. Nguyen, "On the Development of an Integrated CMOS-Based UWB Tunable-Pulse Transmit Module", *IEEE Trans. Microw. Theory Tech.*, vol.54, no.10, pp.3681-3687, Oct. 2006
- [Miskovsky06] P. Miškovský, J. M. González Arbesú, J. Romeu, "Application of UWB Antenna Descriptors to Lossy Dipole Performance Assessment", IEEE AP-S, pp. 175 - 178, Albuquerque NM, July 2006
- [Miskovsky07a] P. Miškovský, J. M. González Arbesú, J. Romeu, "Application of UWB Antenna Descriptors to Antenna Performance Assessment", Springer, ISBN 978-0-387-73045-5, *Ultra-Wideband Short-Pulse Electromagnetics 8*, Baum, C. E.; Stone A. P.; Tyo, J. S.; (Eds.), 262 p., 2007
- [Miskovsky07b] P. Miškovský, J. M. González Arbesú, J. Romeu, "What can we expect from a continuously tapered, resistively loaded monopole, for UWB applications", IEEE AP-S, pp.1421-1424, Honolulu HI, June 2007
- [Miskovsky09] P. Miškovský, J. M. González Arbesú, J. Romeu, "Antenna Radiation Efficiency Measurement in an Ultrawide Frequency Range," *IEEE Ant. & Wireless Prop. Letters*, vol.8, pp.72-75, 2009

- [Mollfulleda05] A. Mollfulleda, M. Nájjar, P. Miškovský, C. Ibars, J. Mateu, M. Navarro, "Ultra-wideband Testbed For Reduced Data-rates and Location", IEEE ICU, Zurich, Sept. 2005
- [Mollfulleda06] A. Mollfulleda, M. Najjar, P. Miskovsky, J. A. Leyva, L. Berenguer, C. Ibars, M. Navarro, "QUETZAL: qualified ultra-wideband testbed for reduced data-rates and location," Proc. *TRIDENTCOM 2006*, pp.7-191.
- [Montoya96] T. P. Montoya, G. S. Smith, "A study of pulse radiation from several broad-band loaded monopoles," *IEEE Trans. Antennas Propag*, vol.44, no.8, pp.1172-1182, Aug 1996
- [McLean05] J.S. McLean, H. Foltz, R. Sutton, Pattern descriptors for UWB antennas, *IEEE Trans. Antennas Propag.*, vol. 53, no. 1, pp. 553-559, Jan. 2005.
- [McKinzie97] W. E. McKinzie III, "A modified Wheeler cap method for measuring antenna efficiency," Proc. *IEEE Antennas Propag. Soc. Int. Symp.*, vol.1, pp.542-545, July 1997
- [Mushiake92] Y. Mushiake, "Self-Complementary Antennas", *IEEE Ant. & Propag. Mag.*, vol. 34, no.6, pp.23-29, Dec. 1992
- [NASA] "How Old is the Universe?", a document from NESA web page: <http://map.gsfc.nasa.gov/universe/uni-age.html>
- [Paulsen03] L. Paulsen, J. B. West, W. F. Perger and J. Kraus, "Recent investigations on the volcano smoke antenna," Proc. *IEEE Antennas Propag. Soc. Int. Symp.*, vol.3, pp. 845-848, June 2003
- [Perruisseau09] J. Perruisseau, P. Pardo, P. Miskovsky, "Modelling, Design and Characterization of a very Wideband Slot Antenna with Reconfigurable Band Rejection", *IEEE Trans. Antennas Propag.*, Nov. 2009, accepted for publication
- [Pozar88] D. M. Pozar, B. Kaufman, "Comparison of three methods for the measurement of printed antenna efficiency," *IEEE Trans. Antennas Propag.*, vol.36, no.1, pp.136-139, Jan. 1988.

- [Pozar98] D. Pozar, *Microwave Engineering*, second edition, Wiley & Sons Inc. 1998.
- [Rao69] B. Rao, J. Ferris, W. Zimmerman, "Broadband characteristics of cylindrical antennas with exponentially tapered capacitive loading," *IEEE Trans. Antennas Propag.*, vol.17, no.2, pp. 145-151, Mar. 1969
- [Reyes06] M. Reyes-Sierra, C. A. Coello Coello, "Multi-Objective Particle Swarm Optimizers A Survey of the State-of-the-Art," *Intl. Journal of Computational Intelligence Research*, vol.2, no.3, pp. 287-308, 2006
- [Reinhardt07] Reinhardt Microtech Technical Specification, can be found in <http://www.reinhardt-microtech.ch/company/firstpage.htm>
- [Robinson04] J. Robinson, Y. Rahmat-Samii, "Particle swarm optimization in electromagnetics," *IEEE Trans. Antennas Propag.*, vol.52, no.2, pp. 397-407, Feb. 2004
- [Robinson02] J. Robinson, S. Sinton, Y. Rahmat-Samii, "Particle swarm, genetic algorithm, and their hybrids: optimization of a profiled corrugated horn antenna," *Proc. IEEE Antennas Propag. Soc. Int. Symp.*, vol.1, pp. 314-317, 2002
- [Ross73] G. F. Ross, *Baseband Pulse Object Sensor system*, November 13, 1973, US Patent 3,772,697
- [Rumsey57] V. H. Rumsey, "Frequency Independent Antennas", *IRE International Convention Record*, vol.1, part5, pp.114-118, March 1957
- [STD79] "IEEE standard test procedures for antennas," *ANSI/IEEE Std 149-1979*, 19 Dec 1979
- [Schantz01] H. G. Schantz, "Measurement of UWB antenna efficiency," *IEEE Vehicular Tech. Conf.*, vol.2, pp.1189-1191, 2001.

- [Schantz04] H. G. Schantz, *The Art & Science of Ultra-Wideband Antenna Design*, short course, *IEEE Antennas Propag. Soc. Int. Symp.*, 2004
- [Schantz02] H. G. Schantz, "Radiation efficiency of UWB antennas," *IEEE Conference on Ultra Wideband Systems and Technologies*, pp. 351-355, 2002
- [Schelkunoff41] S. A. Schelkunoff, March 18, 1941, *Ultra Short Wave Radio System*, US Patent 2,235,506
- [Schelkunoff66] S. A. Schelkunoff, "Antennas: Theory and practice", 3rd. Ed. Wiley & Sons, 1966
- [Schroeder06] W. L. Schroeder, D. Gapski, "Direct Measurement of Small Antenna Radiation Efficiency by Calorimetric Method," *IEEE Trans. Antennas Propag*, vol.54, no.9, pp. 2646-2656, Sept. 2006.
- [Shannon49] C. E. Shannon, "Communication in the Presence of Noise," *Proceedings of the IRE* , vol.37, no.1, pp. 10-21, Jan. 1949
- [Smith77] G. Smith, "An analysis of the Wheeler method for measuring the radiating efficiency of antennas," *IEEE Trans. Antennas Propag*, vol.25, no.4, pp. 552-556, July 1977.
- [Vishay01] "High Frequency Flat Chip Resistors", Vishay MCT 0603 HF datasheet, Document number 28712, published in
<http://www.vishay.com/docs/28712/mct0603h.pdf>
- [Vishay02] "High Frequency (up to 20 GHz) Chip Resistors", FC Vishay Thin Film datasheet, Document number 60093, published in
<http://www.vishay.com/docs/60093/fcseries.pdf>
- [Vishay03] "Resistors in microwave applications", Vishay App. note AP0010, published in
http://www.ieee.li/pdf/essay/resistors_in_microwave_applications.pdf

- [Wheeler59] H. A. Wheeler, "The radian sphere around a small antenna," *Proc. IRE*, vol. 47, pp. 1325-1331, Aug. 1959.
- [Wu65] T. T. Wu and R. W. P. King, "The cylindrical antenna with non-reflecting resistive loading," *IEEE Trans. Antennas Propag.*, vol. AP-13, no. 3, pp. 369-373, May 1965
- [Zhuang03] W. Zhuang, X. Shen, Q. Bi, "Ultra-wideband wireless communications," *Wirel. Commun. Mob. Comput.* 2003; pp.663-685, Wiley & Sons, Ltd 2003